Reconciliation of Almost-Invariant Tori in Chaotic Systems

Ashley Martin Gibson

A thesis submitted for the degree
of Master of Philosophy of
The Australian National University

13 January 2012

Declaration

This thesis is an account of research undertaken between June 2009 and January 2012 in the Plasma Theory and Modelling Group, Plasma Research Laboratory, Research School of Physics and Engineering, The Australian National University, Canberra, Australia. Except where acknowledged in the customary manner, the material presented in this thesis is, to the best of my knowledge, original, and has not been submitted either in whole or in part for a degree at any university.

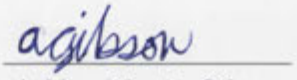

Ashley Martin Gibson
13 January 2012

Acknowledgements

There are many people who have contributed directly to the development of my thesis. First and foremost, I would like to thank my supervisors Prof. Robert L. Dewar and Dr. Matthew J. Hole for the extensive help and support they have given me throughout the duration of my research. Without your support, patience and encouragement, I could not have succeeded, and I am very much indebted to both of you. I would also like to thank my advisors Dr. Gregory T. von Nessi and Dr. Boyd D. Blackwell for being involved in my project, even though I didn't use your knowledge and expertise as much as I should have. Some other people I would like to thank are Dr. Stuart R. Hudson for collaborating with Prof. R. L. Dewar to formulate a reconciliation condition for QFMin and ghost tori, and Dr. Alexei B. Khorev for giving us his *Mathematica* notebook so I could visualise QFMin and ghost curves for myself. Your code has been entirely rewritten and now has the capacity to plot reconciled QFMin-ghost curves as well. I would also like to thank Mr. Mathew McGann for allowing me to use his code to draw Figure 1.6.

Besides these people, there are also many people who have not contributed directly to my thesis, but who have given me so much help and guidance in the finer points of life that my thesis would not have been what it is today without them. In particular, I would like to thank Prof. Neil B. Manson for overseeing my research candidature, and for encouraging me to persevere with my research no matter how much I wanted to give up. I would also like to thank Mr. Jason Bertram, who shared an office with me and reiterated Prof. N. B. Manson's words of encouragement, and the various support people I have conversed with over the years, both on- and off-campus. There are far too many of you to name here, and to do so would be a breach of privacy, but I'm sure you know who you are. You had a greater impact on my studies than you realised. I would also like to thank the members of the Shobu-Kai karate club in Canberra, Australia, headed by Sensei Ivan Mehkek, for giving me a place where I could relax and forget about my studies, but where I could still learn about the benefits of hard work, focus and discipline, and gain a healthy dose of self-confidence. I still believe that doing Shobu-Kai karate three times a week is one of the best ways to relieve stress and avoid depression, and I am greatly indebted to all of you for giving me a reason to persevere with my studies.

Finally, I would like to thank my parents and siblings for being supportive of me throughout the duration of my candidature, even though I have never been able to explain to them what my research is about, or why I had to do it in Canberra. I especially want to thank my father David for all the money he has loaned me so I could remain in Canberra long enough to bring my thesis up to such a high standard. I don't know how I will ever be able to pay it back to you. I also want to apologise to my parents, siblings and relatives for not flying up to Brisbane to spend Christmas with them last year. It's almost unheard of for us to be visited by so many relatives for Christmas, and I'm sure that my absence put a dampener on the festive spirit. However, it was important for me to avoid all sources of distraction and remain focussed on my goal throughout the remainder of my candidature, because as any good karateka knows, if you look away from your opponent for just a fraction of a second, you get hit. Fortunately, I have been able to remain focussed

on my thesis until the very end, and submit it on a day that holds great intrigue for both mathematicians and non-mathematicians alike.

In Western cultures, it has become customary to consider Friday the 13th to be unlucky, but as anyone who has spent any decent amount of time dealing with golden numbers and their continued-fraction convergents will recognise, the number 13 is revered by mathematicians much more than it is despised and rejected by them. As such, I couldn't resist submitting my thesis on Friday, the 13th of January, as a tribute to the number 13 and its relationship to the golden mean. I insincerely apologise to anyone who happens to read my thesis while suffering from triskaidekaphobia or paraskevidekatriaphobia, and I sincerely believe that they should seek psychological treatment, because 13 is one of the most beautiful numbers in the study of chaos.

Abstract

Magnetic field lines within toroidal magnetic confinement systems can be described as orbits of $1\frac{1}{2}$-degree-of-freedom Lagrangian and Hamiltonian systems. In axisymmetric devices such as ideal tokamaks in equilibrium, all field lines lie within a smoothly nested set of invariant tori (magnetic surfaces) foliating the plasma volume, but this integrability is lost within non-axisymmetric devices such as stellarators. That is, not all field lines lie within magnetic surfaces and thus they cannot be described by conventional action-angle coordinates. However, according to the Kolmogorov-Arnold-Moser (KAM) theorem, some invariant tori, covered ergodically by quasiperiodic orbits, survive perturbation away from integrability. Furthermore, by the Poincaré-Birkhoff theorem, two kinds of periodic orbits (closed field lines), called the action-minimax and action-minimising orbits, survive perturbation, and they can be incorporated into families of pseudo-orbits that provide best approximations to invariant tori within nonintegrable systems.

The three candidates for such almost-invariant tori discussed in this thesis are quadratic-flux-minimising (QFMin) tori, which minimise the integral of the square of the action gradient over the poloidal and toroidal angles, action-gradient-minimising (AGMin) tori, which minimise the square of the action gradient over each periodic pseudo-orbit, and ghost tori, which join the action-minimax and action-minimising orbits via an action-gradient flow. Although none of these almost-invariant tori has any direct physical interpretation, it has been shown by Hudson and Breslau (Phys. Rev. Lett., **100**, 095001 (2008)) that ghost tori are in very close correspondence with temperature isotherms. There is also a very close relationship between QFMin, AGMin and ghost tori, which suggests that they could be made equivalent to each other or "reconciled" by making an appropriate coordinate transformation.

By using the standard map as a discrete-time model for magnetic field lines via the kicked rotor, it is demonstrated using *Mathematica* that QFMin and ghost tori can be reconciled with each other up to at least $k = 1.0$ for all rational rotational transforms with denominator less than or equal to 13, where k denotes the nonlinearity parameter of the standard map. This is accomplished by expanding the coordinate transformation as a Fourier series and formulating a variational principle, which is used to numerically construct a set of almost-invariant curves that have rotational transforms equal to continued-fraction convergents of two minus the golden mean (i.e., $0.381966\ldots$). By calculating the flux between the curves, it is shown via a preliminary investigation that the reconciled QFMin-ghost tori are consistent with Greene's residue criterion and the existence of KAM tori within the standard map for $k < 0.971635\ldots$, which is the value at which the last KAM curves are destroyed. It is also shown via the construction of a rigidity principle that the reconciled QFMin-ghost tori have also been reconciled with AGMin tori, by appealing to the fact that discrete-time dynamical systems are merely just Poincaré sections of continuous-time dynamical systems, for which the rigidity principle was formulated. This provides an important first step towards constructing an almost-straight-field-line coordinate system for magnetic islands.

List of Original Research

Throughout the preparation of this thesis, I have drawn heavily on the work of others in order to present my results as clearly as possible. I have also relied heavily on the advice and feedback from my supervisors Prof. Robert L. Dewar and Dr. Matthew J. Hole. As such, I would like to draw your attention to those sections of my thesis which contain either partially (in collaboration with Prof. R. L. Dewar) or substantially my own original research. These sections are as follows:

- Section 3.5.1: The Lagrangian derivation of the Euler-Lagrange equation for continuous-time QFMin tori, which was published in Dewar, Hudson, and Gibson (Commun. Nonlinear Sci. Numer. Simulat., **17**, 2062 (2012)).
- Sections 3.6.1–3.6.3: The Lagrangian and Hamiltonian derivations of the Euler-Lagrange equations for continuous-time AGMin tori. This is a modification of the Euler-Lagrange equations for AGMin pseudo-orbits that were published in Dewar, Hudson, and Gibson (Commun. Nonlinear Sci. Numer. Simulat., **17**, 2062 (2012)).
- Section 3.7: The demonstration that continuous-time QFMin and AGMin pseudo-orbits belong to the same class of pseudo-orbits, and by extension, that continuous-time QFMin and AGMin tori belong to the same class of almost-invariant tori.
- Section 3.9 (first paragraph): The observation that the trajectories of AGMin and ghost curves are much closer to each other than they are to the trajectories of QFMin curves, and the observation that the trajectories of AGMin and ghost curves cross each other at points where the action is not extremised.
- Section 4.1: The discovery of the rigidity principle for almost-invariant tori, which was based on the observation that the right hand side of Equation (3.66) is equal to the right hand side of Equation (3.88), and the Lagrangian and Hamiltonian derivations of the rigidity principle.
- Section 5.9: An alternative Lagrangian formulation of the Euler-Lagrange equation for discrete-time QFMin tori, which is based on substituting the Lagrangian for the kicked rotor into the Euler-Lagrange equation for continuous-time QFMin tori and finding a parabolic trial function.
- Section 5.10: The demonstration that discrete-time QFMin and AGMin pseudo-orbits belong to the same class of pseudo-orbits, and by extension, that discrete-time QFMin and AGMin tori belong to the same class of almost-invariant tori.
- Section 6.2: The determination of the periodicity of the momentum under a canonical transformation that's consistent with the coordinate transformation that's being used to reconcile QFMin and ghost tori.
- Section 6.7: The construction of a variational principle for reconciled QFMin-ghost tori in discrete-time systems.

- Sections 6.8 and 6.9: The construction of a perturbative expansion for reconciled QFMin-ghost tori in discrete-time systems and the determination of its first-order solutions, including the case where the generating function takes the form of the one used to generate the standard map.

- Sections 7.1–7.4: The construction of a variational principle for reconciled QFMin-ghost tori in discrete-time systems, including the imposition of the reality condition, the restriction to odd basis functions, the discovery that an additional constraint was required to ensure the uniqueness of the pseudo-orbits, and the imposition of this additional constraint.

- Sections 7.5–7.8: The numerical implementation of the variational principle for reconciled QFMin-ghost tori in discrete-time systems using *Mathematica*, including the selection of the minimisation and integration methods, and the techniques that were used to maximise the algorithm's speed.

- Section 8.2: The investigation of the convergence of the Fourier series obtained from the numerical implementation of the variational construction, including the plots of its power spectra.

- Section 8.3: The investigation of the monotonicity of the transformation used to complete the reconciliation, including the plots of the coordinate transformation and its derivative.

- Section 8.4: The investigation of the reconciled QFMin-ghost curves in phase space, including the plots of the reconciled QFMin-ghost curves.

- Section 8.7: The investigation of the differences between the reconciled QFMin-ghost curves, including the plots of these differences and the observation that they are consistent with Greene's residue criterion and the existence of KAM tori for $k < 0.971635\ldots$.

- Section 8.8: The determination of the flux leakage exponents from the difference plots, and the preliminary analysis which shows they are consistent with Greene's residue criterion and the existence of KAM tori for $k < 0.971635\ldots$.

- Section 8.9: The assertion that because QFMin and ghost tori can be reconciled with each other, then by the rigidity principle defined in Section 4.1, the reconciled QFMin-ghost tori must necessarily be reconciled with AGMin tori.

The remaining sections of my thesis do not contain significant amounts of original research, but are important for the overall development of the argument and the provision of an adequate survey of the literature.

Contents

Chapter 1

Introduction to Plasma Fusion Physics

This chapter serves as an introduction to plasma fusion physics, and provides the physical motivation for the highly mathematical calculations that occur throughout the rest of this thesis. In particular, it discusses why plasmas are used in nuclear fusion devices, how plasmas can be described using the MHD model, the types of fusion devices that are used to magnetically confine plasmas, and the meaning of equilibrium in the context of plasmas. It also introduces the toroidal magnetic coordinate system as a means to describe plasmas, and discusses the importance of magnetic surfaces. The rotational transform is also introduced as a means of quantifying the trajectories of magnetically confined plasmas, and the breakdown of magnetic surfaces is used as motivation for the determination of an almost-straight-field-line coordinate system for magnetic islands.

1.1 What is Plasma?

Plasma is the fourth state of matter in which gas has become sufficiently ionised for it to be an effective electrical conductor [1]. There are many different examples of plasmas, including, but not limited to, fire and lightning (see Figure 1.1), astrophysical objects such as solar wind, the magnetosphere, the auroras, the Sun, stars, nebulae, the interior of gas giants such as Jupiter, Saturn, Uranus and Neptune, and common, everyday appliances such as plasma televisions, fluorescent lights, plasma lamps and even plasma globes. Plasmas are also heavily used in industrial processing and the semiconductor industry. The two key properties of plasmas are that they contain a significant degree of ionisation and that they're electrostatically neutral [2]. **Ionisation** occurs when the kinetic energy of the electrons inside an atom is greater than its ionisation energy, which allows the electrons to escape the atomic bonds and become free charges. **Electrostatic neutrality** means that macroscopic volumes of plasma do not contain large net electric charges [2].

1.2 Nuclear Fusion

One application of plasma physics is to enable **nuclear fusion** for power. The easiest reaction to initiate is the reaction between deuterium and tritium, because it has the largest collisional cross-section. Although deuterium is found abundantly on Earth, tritium is extremely scarce because it has a half-life of only 12.5 years. Fortunately, lithium is reasonably abundant on Earth, and can be used to manufacture tritium. This is made possible by neutron activation of lithium, in which a 100 MeV neutron impacting lithium

Figure 1.1: Lightning is a common, everyday example of plasma [3].

can produce up to fourteen tritium nuclei [2]. There is enough deuterium and lithium on this planet for this type of fusion power to supply all our energy needs for millions of years.

There are two prominent lines towards realising fusion power, namely **magnetic fusion** and **inertial confinement** [2]. In magnetic confinement fusion, a magnetic field is used to contain the plasma, whereas in inertial confinement, deuterium and tritium are compressed by lasers. This thesis will focus on magnetic field line representations for toroidal magnetic confinement.

1.3 The Ideal MHD Model of Plasmas

A simple, but surprisingly accurate description of plasmas is afforded by the **magneto-hydrodynamic (MHD) model**. The MHD model of plasmas is a combination of fluid mechanics and electromagnetism with the neglect of Maxwell's correction to Ampère's Law. The MHD model can be applied to any electrically conducting fluid that's in the presence of a magnetic field [2]. Electric charges do not appear explicitly in the ideal MHD equations.

The MHD model holds when the plasma is dominated by collisions [2], and the charged particles have equal temperatures. However, because plasmas are quasineutral, it follows that the particles must also have equal pressures, and that the energy equilibrium times must be considerably shorter than the characteristic time. This implies that the MHD equations hold when [2]

$$r_i \ll a, \tag{1.1}$$

$$\sqrt{\frac{m_i}{m_e}} v_i \tau \ll a, \tag{1.2}$$

where r_i is the Larmor radius of the ions, $a \in \mathbb{R}^+$ (the set of positive real numbers) is the MHD scale length, m_i is the ion mass, m_e is the electron mass, v_i is the thermal speed of the ions, and τ is the collision time between ions. However, in cases where the electrical resistivity is negligible, or the resistive diffusion time is much less than the MHD time scale, these two conditions are conflated to give the **scale length ordering** [2]

$$\sqrt{\frac{m_e}{m_i}} \frac{r_i^2}{v_i \tau} \ll a. \tag{1.3}$$

When this condition is satisfied, the MHD equations are said to be **ideal** because they utilise the ideal version of Ohm's law. They are given by [2]

$$\frac{\partial \rho}{\partial t} + \nabla \cdot (\rho \mathbf{v}) = 0, \quad \text{the mass continuity equation,} \tag{1.4}$$

$$\frac{\mathrm{d}}{\mathrm{d}t}\left(\frac{P}{\rho^{\gamma}}\right) = 0, \quad \text{the adiabatic equation of state,} \tag{1.5}$$

$$\rho \frac{\mathrm{d}\mathbf{v}}{\mathrm{d}t} = \mathbf{J} \times \mathbf{B} - \nabla P, \quad \text{the momentum equation,} \tag{1.6}$$

$$\nabla \times \mathbf{B} = \mu_0 \mathbf{J}, \quad \text{Ampère's law,} \tag{1.7}$$

$$\nabla \times \mathbf{E} = -\frac{\partial \mathbf{B}}{\partial t}, \quad \text{Faraday's law,} \tag{1.8}$$

$$\nabla \cdot \mathbf{B} = 0, \quad \text{Gauss's law for magnetism, and} \tag{1.9}$$

$$\mathbf{E} + \mathbf{v} \times \mathbf{B} = 0, \quad \text{the ideal version of Ohm's law,} \tag{1.10}$$

where γ is the ratio of specific heats, $\mathrm{d}/\mathrm{d}t = \partial/\partial t + \mathbf{v} \cdot \nabla$ is the convective derivative, and all other symbols have their regular meaning. The MHD equations inherit the four basic conservation properties of fluid mechanics and electromagnetism – energy, mass, momentum, and magnetic flux.

1.4 Toroidal Magnetic Confinement

Plasma confinement is the process of trapping plasma inside an arbitrary region of space. **Toroidal magnetic confinement** is a type of plasma confinement that uses a magnetic field to trap plasmas inside a toroidal region of space, and can be divided into two broad classes that use either tokamaks or stellarators for the confinement process [1].

Tokamaks are approximately toroidally symmetric (or **axisymmetric**), which makes it possible to reduce descriptions of them to two-dimensional systems without losing magnetic field line information. However, they also require a toroidal current to create magnetic surfaces [4]. **Stellarators**, which are toroidally asymmetric (or **non-axisymmetric**), use external coils to generate the magnetic surfaces. As the stellarator is non-axisymmetric, it has no ignorable spatial coordinate, so magnetic descriptions of it

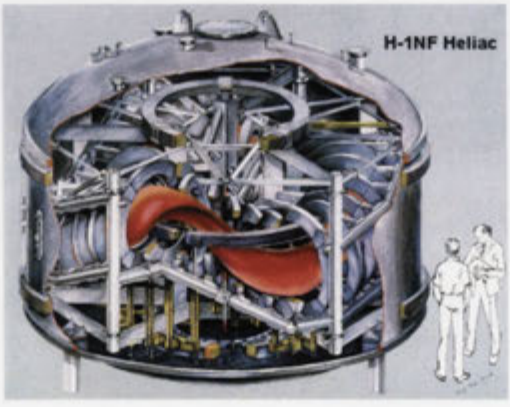

Figure 1.2: H-1 heliac toroidal stellarator at the Australian National University in Canberra, Australia.

cannot be reduced to two dimensions as in the case of tokamaks [4]. A schematic of the H-1 heliac stellarator at the Australian National University is shown in Figure 1.2.

1.5 Ideal MHD Equilibrium

If a plasma satisfies the assumptions of the MHD model, then its equation of motion is given by $\rho \, \mathrm{d}\mathbf{v}/\mathrm{d}t = \mathbf{J} \times \mathbf{B} - \boldsymbol{\nabla} P$, where ρ is the mass density, $\mathrm{d}\mathbf{v}/\mathrm{d}t$ is the acceleration of the particles, $\mathbf{J}$ is the current density, $\mathbf{B}$ is the magnetic field, and P is the pressure [5]. However, if the acceleration of the particles is zero, then the plasma is said to be in **equilibrium**, and the equation of motion reduces to $\mathbf{J} \times \mathbf{B} = \boldsymbol{\nabla} P$ [5].

For a plasma in ideal MHD equilibrium, both $\mathbf{J} \cdot \boldsymbol{\nabla} P = 0$ and $\mathbf{B} \cdot \boldsymbol{\nabla} P = 0$. This implies that both the current and the magnetic field travel along lines of constant pressure, so there is no pressure gradient in the direction of either the current or the magnetic field [5]. Equilibrium places severe constraints on the topology of closed field line surfaces that can be used to confine a plasma, because the condition that $\mathbf{B} \cdot \boldsymbol{\nabla} P = 0$ can only be satisfied when the magnetic field lines lie on a **torus** [1, 4]. Hence, the study of tori is a crucial component of magnetic confinement theory.

1.6 Coordinates and Fluxes

In order to describe plasmas confined by toroidal magnetic fields, it is helpful to introduce a new coordinate system in which one of the coordinates stays constant on a magnetic surface. This new coordinate system, called **toroidal magnetic coordinates**, contains a surface label s, a poloidal angle θ, and a toroidal angle ζ, of which both θ and ζ are 2π-periodic [5]. The direction of each of these coordinates is shown in Figure 1.3.

In toroidal magnetic confinement, the magnetic field lines form a torus by travelling around a circle called the **poloidal axis** in helical trajectories [5]. The poloidal axis remains equidistant from the **toroidal axis**, which, by convention, runs through its centre in the direction of the right-hand rule (see Figure 1.3). In plasma confinement theory, the poloidal axis is often called the **magnetic axis**, because the magnetic field lines wrap around it. The angle that a point on a magnetic field line makes with the poloidal axis as it gyrates around it is denoted by θ, whereas the angle that the point makes with the toroidal axis as it revolves around it is denoted by ζ [5].

The most basic example of an axisymmetric system is a tokamak with circular cross-section and zero pressure, which resembles the geometry of Figure 1.3. In axisymmetric systems, the magnetic field lines lie in nested surfaces around the tori, and are differentiated by the surface label coordinate s [5] (see Figure 1.4). Nested surfaces are usually called **toroidal magnetic surfaces**, although one or more of the adjectives is sometimes dropped.

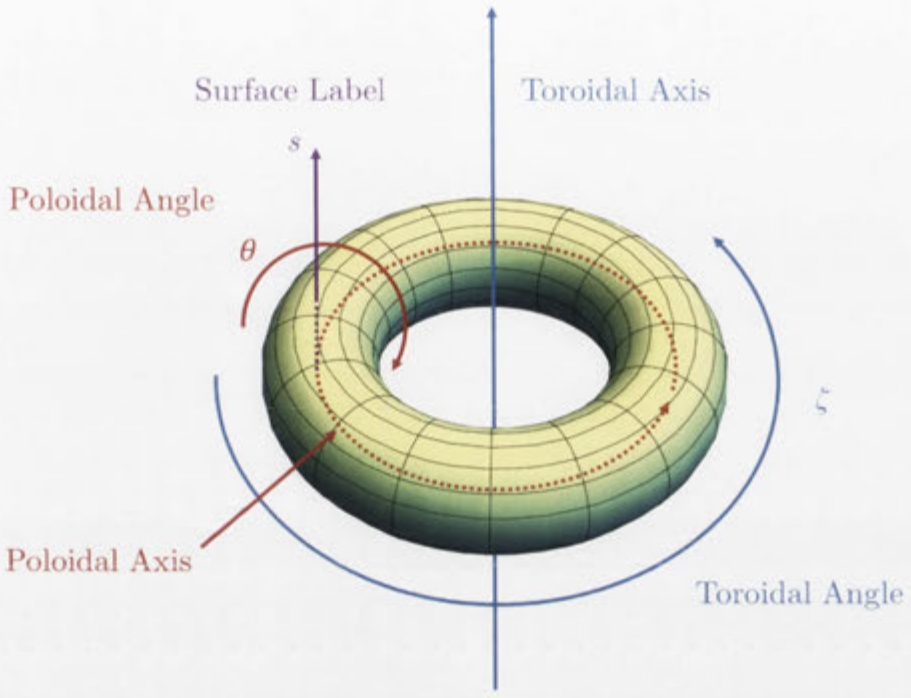

Figure 1.3: Toroidal magnetic coordinates and their axes.

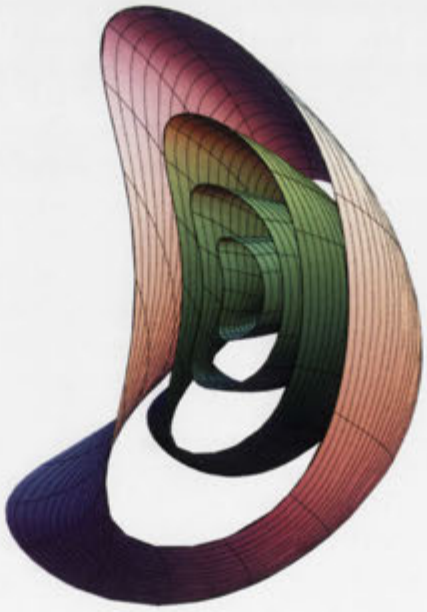

Figure 1.4: Nested toroidal magnetic surfaces.

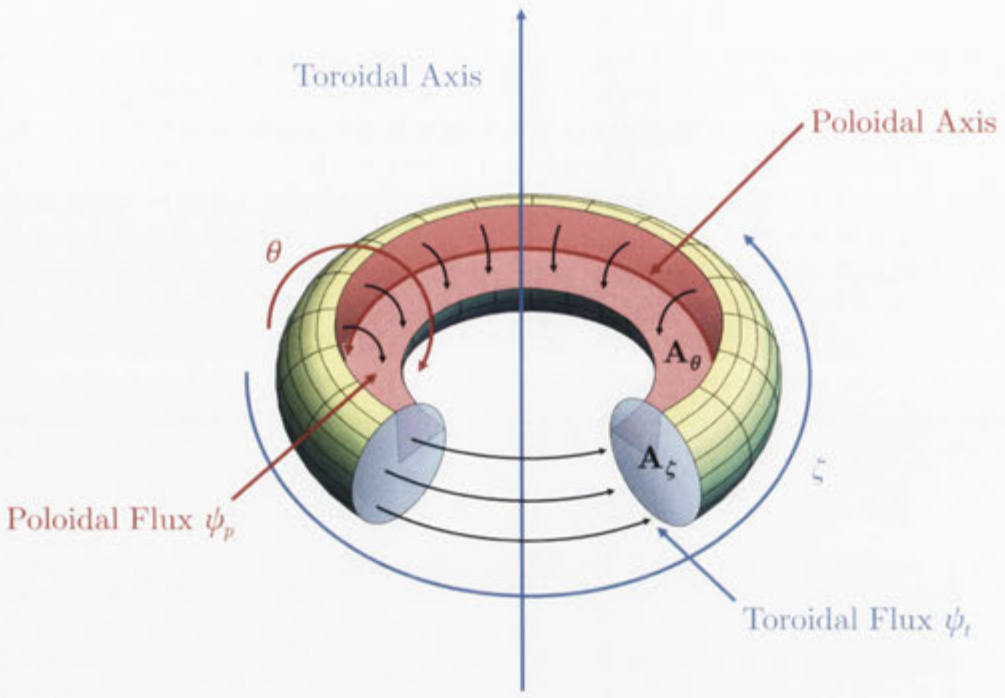

Figure 1.5: Poloidal and toroidal magnetic fluxes.

Magnetically confined plasmas can be described by two separate flux functions [1]. The **toroidal magnetic flux**, given by $\psi_t = \int \mathbf{B} \cdot \mathrm{d}\mathbf{A}_\zeta$, is the flux parallel to the poloidal axis that intersects the cross-section of a magnetic surface at constant ζ [1]. Similarly, the **poloidal magnetic flux**, given by $\psi_p = -\int \mathbf{B} \cdot \mathrm{d}\mathbf{A}_{\boldsymbol{\theta}}$, is the flux relationship in the poloidal direction between the poloidal axis and the locus of a magnetic surface at constant θ. Both types of flux are shown in Figure 1.5.

1.7 The Rotational Transform

The helicity of the magnetic field inside a plasma is not constant, and changes from one surface to another. These changes can be quantified by the **rotational transform**, or **winding number**, which measures the average twist, or pitch, of the magnetic field lines [1,5]. The rotational transform is the rate of change of the poloidal magnetic flux with respect to the toroidal magnetic flux, and is given by [1,6]

$$\iota = \frac{\mathrm{d}\psi_p}{\mathrm{d}\psi_t} = \lim_{\Delta\zeta \to \infty} \frac{\Delta\theta}{\Delta\zeta}. \tag{1.11}$$

It can take both positive and negative values, depending on the direction of the field. If a magnetic field line transits more poloidal rotations than toroidal rotations, then $|\iota| > 1$, and if it transits more toroidal rotations than poloidal rotations, then $|\iota| < 1$. When $|\iota| = 1$, the magnetic field line transits one poloidal transit per toroidal transit, and returns to its starting position after each rotation [5]. All magnetic field lines lying on the same magnetic surface must have the same rotational transform. The rotational transform ι is constant on a flux surface and, in general, changes between flux surfaces.

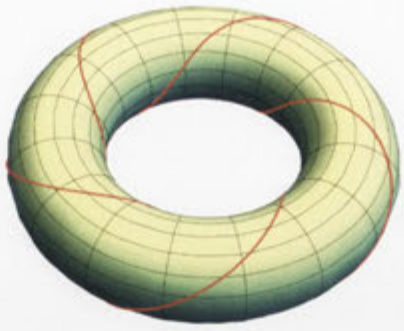

Figure 1.6: Magnetic field lines with rational rotational transform $\iota = 5/2$ travelling around a torus. These field lines close on themselves after five poloidal transits and two toroidal transits.

It is an important consequence of the definition of the rotational transform that a magnetic field line is periodic if and only if it has **rational rotational transform** [5]. If the rotational transform is rational, then it has the form $\iota = p/q$, where p and q are integers representing the respective number of poloidal and toroidal transits after which the magnetic field lines close on themselves [5]. This closure can only occur under the periodicity condition $\theta_q = \theta_0 + 2\pi p$, where θ_0 is the value of θ at $\zeta = 0$, and θ_q is the value of θ at $\zeta = 2\pi q$. A magnetic field line that satisfies this closure condition is said to be **(p, q)-periodic**. However, because we wish to limit our attention to periodic orbits that are connected with unperturbed systems, we shall require p and q to be mutually prime throughout the rest of this thesis, so that they represent the respective *minimum* number of poloidal and toroidal transits after which the magnetic field lines close on themselves. An important consequence of the definition of the rotational transform is that whenever a system is integrable (that is, it has an explicit, analytical, closed-form solution), ι depends solely on ψ_p [5]. An example of a magnetic field line with rational rotational transform $\iota = 5/2$ is shown in Figure 1.6.

1.8 Trajectories of Magnetic Field Lines

Magnetic field lines inside axisymmetric magnetic confinement devices have one of only three fundamentally different kinds of trajectories [4]. In the first case, the rotational transform is rational, and the magnetic field lines create a surface by closing on themselves after a certain number of poloidal and toroidal transits, although they do not come arbitrarily close to every point on that surface [4] (see Figure 1.6). In the second case, the rotational transform is irrational, and the magnetic field lines create a surface on which they come arbitrarily close to every point as $\zeta \to \infty$ [4]. In the third case, the rotational transform can be either rational or irrational, and although the magnetic field lines fail to make a surface, they come arbitrarily close to every point within a nonzero volume of space [4].

The first kind of trajectory is sometimes referred to as a **periodic orbit**, whereas the second and third kinds of trajectories are sometimes referred to as **quasiperiodic orbits** [7]. A family of trajectories of the third kind describes a **chaotic system**, which is obtained by perturbing a family of trajectories of one of the first two kinds. In the first case, where the rotational transform is rational, the magnetic field lines are not structurally stable, so even an infinitesimally small perturbation is enough to make them chaotic over a

nonzero volume. However, in the second case, the **Kolmogorov-Arnold-Moser (KAM) theorem** [8–10] implies that the magnetic field lines, which have irrational rotational transform, are stable under small perturbations for most of the volume within which they reside [4], and create a surface called a **KAM torus**. The cross-sections of KAM tori are known as **KAM curves**. Unfortunately, the stability of KAM curves and KAM tori decreases as the size of the perturbation increases, and under large perturbations, magnetic field lines of the second kind all become chaotic.

1.9 Breakdown of Magnetic Surfaces

As an extension of the KAM theorem, the **Aubry-Mather theorem** [7,11,12] states that quasiperiodic orbits exist not only for systems that have been slightly perturbed from the integrable case, but for all systems and for all rotational transforms that have no corresponding family of contiguous periodic orbits, no matter how big the perturbation is. It also implies that the cross-sections of the trajectories of magnetic field lines form invariant sets called **Aubry-Mather sets**. In the case of the first and second kinds of trajectories, the Aubry-Mather sets are cross-sections of magnetic surfaces called **invariant curves**, whereas in the case of the third kind of trajectory, they contain invariant Cantor sets called **cantori** [12,13]. These cantori are important because they have an infinite set of holes that allow flux to escape, thus leading to the concept of **flux leakage** [7]. Since plasmas cannot be confined by magnetic fields that allow leakage, it is necessary to find ways to minimise leakage during plasma confinement.

Unfortunately, because stellarators are non-axisymmetric, they experience a large amount of **symmetry breaking**, and this symmetry breaking leads to flux leakage. This is because the magnetic surfaces inside stellarators have a tendency to split into **magnetic islands** of rational rotational transform [14], and when the magnetic islands corresponding to different rotational transforms are sufficiently wide to overlap each other, the magnetic field lines within these regions become chaotic [1]. Because chaotic systems experience a large amount of flux leakage, they cannot be used for plasma confinement, and one must find ways to maximise the number of magnetic surfaces inside stellarators, even though they are the exception, rather than the norm [14].

1.10 Research Goals and Outline

The **primary goal** of this thesis is to provide the first step towards finding an almost-straight-field-line coordinate system for magnetic islands, which will allow the dynamics of chaotic regions to be described much more simply than they are now. In pursuit of this goal, we will study the Hamiltonian and Lagrangian formulations of magnetic field lines in Chapter 2, along with Hamilton's Principle, action-angle coordinates, and iterated maps. We will also discuss the relationship between the kicked rotor and the standard map, and use it to demonstrate how the standard map can be used as a toy model for the dynamics inside magnetic confinement systems.

In Chapter 3, we will explain how the Poincaré-Birkhoff Theorem implies the existence of action-minimax and action-minimising orbits in continuous-time chaotic systems, and use them to construct a set of best approximations to the original magnetic surfaces that were destroyed by a perturbation. These new surfaces will be called "almost-invariant tori", and will be shown to consist of quadratic-flux-minimising (QFMin) tori, action-

gradient-minimising (AGMin) tori and ghost tori, as well as generalisations of these. Cross-sections of the almost-invariant tori will also be taken, and plotted in phase space, in order to demonstrate why QFMin, AGMin and ghost tori need to be made equivalent or "reconciled" with each other.

In Chapter 4, we will develop a framework for reconciled almost-invariant tori, by deriving a set of conditions under which QFMin, AGMin and ghost tori must be equal under the most general coordinate transformation of the poloidal angle. In particular, this involves the development of a reconciliation condition and variational principle under which QFMin and ghost tori are equal, and showing that the reconciled QFMin-ghost tori can be reconciled with AGMin tori via a rigidity principle.

In Chapter 5, we will begin to prepare the results for numerical implementation by showing that many of the results from Chapters 2 and 3 can also be applied to discrete-time systems without making any major modifications to them, and in Chapter 6, we will do the same with the results from Chapter 4. Towards the end of Chapter 6, we will formulate a perturbative construction for the reconciled QFMin-ghost tori, and use it to analytically calculate a first-order approximation to them.

In Chapter 7, we will replace the perturbative construction for the reconciled QFMin-ghost tori with a variational construction that's better suited to numerical implementation, and impose some conditions and constraints on it in order to ensure that it has a unique solution. We will then implement the variational construction in *Mathematica*, and discuss the results of the numerical implementation in Chapter 8. Finally, we will plot cross-sections of the reconciled QFMin-ghost tori in phase space, and show that the reconciled QFMin-ghost tori are consistent with Greene's residue criterion and the existence of KAM tori within the standard map for $k < 0.971635\ldots$, where k is the nonlinearity parameter and $k_c = 0.971635\ldots$ is the value at which the last KAM curves are destroyed.

Chapter 2

Dynamics of Magnetically Confined Plasmas

This chapter introduces the Lagrangian and Hamiltonian dynamics that will be used to describe magnetic field lines, by showing that magnetic field lines are the trajectories of $1\frac{1}{2}$-degree-of-freedom Hamiltonian systems, and demonstrating that Lagrangian and Hamiltonian systems are connected to each other via a Legendre transformation. It also introduces Hamilton's principle of stationary action, and uses it to define pseudo-orbits that are approximations to magnetic field lines in chaotic systems. Towards the end of this chapter, iterated maps are presented as a means of reducing the dimensionality of dynamical systems to make them easier to analyse, and the kicked rotor is introduced as a toy model for the Poincaré sections of magnetic field lines. The kicked rotor is shown to generate the standard map, which is used extensively throughout the rest of this thesis to model the magnetic field lines inside a hypothetical system.

2.1 Magnetic Field Lines and Hamiltonian Systems

Before proceeding any further, it is necessary to describe the relationship between magnetic field lines and Hamiltonian systems so we can employ more powerful mathematical techniques in our study of magnetic field lines and plasmas. To do this, we define the **configuration space** as being the vector space spanned by all the generalised position and time coordinates, and the **phase space** as being the vector space spanned by all the generalised position, momentum and time coordinates. The former is typically used to define a **Lagrangian system**, whereas the latter is typically used to define a **Hamiltonian system**. We also define the **dimension** of a vector space as being the total number of independent variables, and the **degree of freedom** of a dynamical system as being the number of generalised position coordinates plus half the number of generalised time coordinates. Although this could lead to confusion in systems that have multiple time coordinates, it is more than adequate for this thesis, which does not feature systems that have more than one time coordinate. It follows that the degree of freedom of a dynamical system is always equal to half the dimension of its phase space.

When a magnetic field is written in terms of the toroidal magnetic coordinates defined in Section 1.6, it takes the form [15]

$$\mathbf{B} = \boldsymbol{\nabla}\psi_t \times \boldsymbol{\nabla}\theta + \boldsymbol{\nabla}\zeta \times \boldsymbol{\nabla}\psi_p. \tag{2.1}$$

Assuming that $\mathbf{B} \cdot \boldsymbol{\nabla}\zeta \neq 0$, it can be shown that the magnetic field lines satisfy the

differential equations [1]

$$\frac{\mathrm{d}\psi_t}{\mathrm{d}\zeta} = -\frac{\partial\psi_p(\psi_t,\theta,\zeta)}{\partial\theta}, \tag{2.2}$$

$$\frac{\mathrm{d}\theta}{\mathrm{d}\zeta} = \frac{\partial\psi_p(\psi_t,\theta,\zeta)}{\partial\psi_t}. \tag{2.3}$$

Making the substitutions $\zeta \to t$, $\psi_t \to p$, and $\psi_p \to H$, it can be seen that these are identical to **Hamilton's equations**, defined by

$$\frac{\mathrm{d}p}{\mathrm{d}t} = -\frac{\partial H(p,\theta,t)}{\partial\theta}, \tag{2.4}$$

$$\frac{\mathrm{d}\theta}{\mathrm{d}t} = \frac{\partial H(p,\theta,t)}{\partial p}. \tag{2.5}$$

Hence, the magnetic field lines must be the trajectories of a **$1\frac{1}{2}$-degree-of-freedom Hamiltonian system**, with position θ, momentum ψ_t, time ζ, and Hamiltonian ψ_p [1]. These trajectories are usually called **periodic orbits**. Note that there is nothing contradictory about the time coordinate ζ being 2π-periodic. Since ψ_p is equivalent to the Hamiltonian, it is therefore a function of the other variables $\psi_p = \psi_p(\psi_t,\theta,\zeta)$, which is equivalent to $H = H(p,\theta,t)$. From now on, ψ_p, ψ_t, and ζ will only be used in the context of magnetic fields, whereas H, p, and t will be used in other, more general contexts (although p will usually be denoted by I, due to a convention explained in Section 2.3).

2.2 The Magnetic Action and Hamilton's Principle

The **action** is one of the most fundamental properties of a dynamical system. For a closed (p,q)-periodic magnetic field line C under the vector potential representation $\mathbf{B} = \boldsymbol{\nabla}\times\mathbf{A}$, the action is called the **magnetic field line action** and is given by the functional

$$S[C] = \oint_C \mathbf{A}\cdot\mathbf{dl} = \int_0^{2\pi q} \mathbf{A}\cdot\dot{\mathbf{r}}\,\mathrm{d}\zeta, \tag{2.6}$$

where $\dot{\mathbf{r}} = \mathrm{d}\mathbf{r}/\mathrm{d}\zeta$ is the velocity, $\mathbf{dl} = \dot{\mathbf{r}}\,\mathrm{d}\zeta$ is an infinitesimal line element tangential to C, and $\dot{\mathbf{r}}\cdot\boldsymbol{\nabla}\zeta \equiv 1$ is a vector identity that's always satisfied [16, 17].

This thesis will follow the convention that a dot over a variable denotes total differentiation with respect to either t or ζ (depending on the context), that a prime after a single-variable function denotes total differentiation with respect to its argument, and that unless the context dictates otherwise, a subscript variable denotes partial differentiation with respect to that variable (ψ_p and ψ_t are obvious exceptions to this). Hence, $\dot{x}$ denotes $\mathrm{d}x/\mathrm{d}t$, $\theta'(t)$ denotes $\mathrm{d}\theta/\mathrm{d}t$, and H_θ denotes $\partial H/\partial\theta$.

According to **Hamilton's principle of stationary action**, objects such as ions inside a magnetically confined plasma or some other dynamical system will always travel such that their action is stationary. In terms of the above formulation, this means that S will always be stationary with respect to variations $\delta\mathbf{r}$ of C [16]. To determine when the action is stationary, it is necessary to find the **Euler-Lagrange equations**, which characterise the motion of the object. This is done by calculating the variation in S and setting it equal to zero, which yields a system of equations that the object or ion must obey. In the

magnetic representation of the action, the Euler-Lagrange equations are given by

$$\frac{\delta S}{\delta \mathbf{r}} = \dot{\mathbf{r}} \times \mathbf{B} = 0, \tag{2.7}$$

where $\delta S/\delta \mathbf{r}$ is called the **action gradient**. Clearly, Equation (2.7) is consistent with the fact that $\dot{\mathbf{r}}$ is parallel to $\mathbf{B}$ within magnetic fields [16, 17]. The action can also be generalised to other systems besides magnetic fields, and we will turn our attention to these in Sections 2.4 and 2.6.

2.3 Integrable Systems and Action-Angle Coordinates

A Hamiltonian system is said to be **integrable** if and only if it has an explicit, analytical, closed-form solution. The solution to such systems is obtained by transforming them into a special type of coordinate system called **action-angle coordinates** [18], which greatly simplifies their dynamics and makes it possible to obtain an explicit, analytical, closed-form solution to them. This solution is usually obtained via integration, which is why such systems are said to be integrable. By definition, a Hamiltonian system is integrable if and only if it can be written in terms of action-angle coordinates.

The goal of action-angle coordinates is to find an explicit, closed-form solution to a time-independent Hamiltonian $H = H(p, \theta)$ by making it independent of θ, so that the momentum p and the Hamiltonian H become constant. This gives the Hamiltonian the form $H = H(p)$ [18], so that Equation (2.4) is identically zero and p can be written explicitly in terms of H via analytical integration. Since both H and p are constant, $\mathrm{d}\theta/\mathrm{d}t$ is also constant via Equation (2.5), which means that θ depends linearly on t [18]. Regardless of the initial coordinate system, action-angle coordinates invariably have the same phase space as an **invariant torus**, with p being the action variable and θ being the angle variable. However, due to a long-standing convention, the action variable is usually denoted by I, rather than p, and we will use this convention throughout the rest of this thesis to avoid confusion with the numerator of rational rotational transforms.

Some good examples of physical systems that don't look anything like tori, but can still be written in terms of action-angle coordinates, include simple harmonic oscillators and simple pendula. These systems are therefore integrable because their phase spaces can be reduced to those of simple tori. Because they are used to describe invariant tori, toroidal magnetic coordinates are usually defined such that they form an action-angle coordinate system [1]. In such cases, both ψ_p and ψ_t are constant on each magnetic surface and can be used to define a surface label [5]. However, this isn't always the case, and in integrable systems that are not written in terms of action-angle coordinates, only ψ_p can be used to define a surface label [5]. It follows from these definitions that invariant tori are integrable, whereas noninvariant tori are nonintegrable. In magnetic confinement systems, action-angle coordinates are usually referred to as **straight-field-line coordinates** [6].

2.4 Hamiltonian Dynamics

A **path** within the Hamiltonian phase space is a curve defined parametrically by $\theta = \vartheta(t)$, $I = \mathcal{I}(t)$ that lies within the covering space $[0, I_{\max}] \times \mathbb{R} \times \mathbb{R}$, where $I_{\max}$ is the maximum value of the surface label [19]. The rotational transform corresponding to a path in phase space can be either rational or irrational, but when it is rational, it has the form $\iota = p/q$,

where p and q are integers that we have restricted to being mutually prime, and the path is said to be **(p, q)-periodic** because it satisfies the closure conditions [19]

$$\vartheta(t + 2\pi q) = \vartheta(t) + 2\pi p, \tag{2.8}$$
$$\mathcal{I}(t + 2\pi q) = \mathcal{I}(t), \tag{2.9}$$

for all $t \in \mathbb{R}$. For a (p, q)-periodic path parametrised by $\theta = \vartheta(t)$, $I = \mathcal{I}(t)$ inside a Hamiltonian system, the **action** S is given by [19]

$$S[\vartheta, \mathcal{I}] = \int_0^{2\pi q} \left[\mathcal{I}\dot{\vartheta} - H(\mathcal{I}, \vartheta, t)\right] \mathrm{d}t, \tag{2.10}$$

and the variation in S is given by

$$\begin{aligned} \delta S[\vartheta, \mathcal{I}] &= \int_0^{2\pi q} \left(\dot{\vartheta}\,\delta\mathcal{I} + \mathcal{I}\,\delta\dot{\vartheta} - H_I\,\delta\mathcal{I} - H_\theta\,\delta\vartheta\right) \mathrm{d}t \\ &= \int_0^{2\pi q} \left[\left(-\dot{\mathcal{I}} - H_\theta\right)\delta\vartheta + \left(\dot{\vartheta} - H_I\right)\delta\mathcal{I}\right] \mathrm{d}t, \end{aligned} \tag{2.11}$$

where the last line was obtained by using integration by parts (the endpoints cancel due to the periodicity conditions given by Equations (2.8) and (2.9)). However, because S is a functional, the variation in S must also be of the form [19]

$$\delta S[\vartheta, \mathcal{I}] = \int_0^{2\pi q} \left(\frac{\delta S}{\delta\theta}\,\delta\vartheta + \frac{\delta S}{\delta I}\,\delta\mathcal{I}\right) \mathrm{d}t, \tag{2.12}$$

so when combined with the previous equation, it can be seen that the gradients of the action are given by the functional derivatives [19]

$$\frac{\delta S}{\delta\theta} = -\dot{I} - H_\theta \tag{2.13}$$
$$\frac{\delta S}{\delta I} = \dot{\theta} - H_I. \tag{2.14}$$

When a (p, q)-periodic path satisfies both $\delta S/\delta\theta = 0$ and $\delta S/\delta I = 0$ for all t, it is called a **(p, q)-periodic orbit**, and it satisfies **Hamilton's equations**

$$\dot{\theta} = H_I, \tag{2.15}$$
$$\dot{I} = -H_\theta. \tag{2.16}$$

However, if a (p, q)-periodic path satisfies only $\delta S/\delta I = 0$ for all t, but $\delta S/\delta\theta \approx 0$ is of order ε, then it is called a **(p, q)-periodic pseudo-orbit** [19]. It can be seen from the definition that (p, q)-periodic pseudo-orbits are generalisations of (p, q)-periodic orbits, in that they satisfy Equation (2.15) but not Equation (2.16).

Note that because $\delta S/\delta I = 0$ on both (p, q)-periodic orbits and (p, q)-periodic pseudo-orbits, it is less interesting than $\delta S/\delta\theta$, so any reference to a singular action gradient within a Hamiltonian system will always be a reference to $\delta S/\delta\theta$ rather than $\delta S/\delta I$. Also, any reference to a singular Euler-Lagrange equation within a Hamiltonian system will always be to that which contains $\delta S/\delta\theta$, rather than to that which contains $\delta S/\delta I$, because it will be implicitly assumed that the Euler-Lagrange equation containing $\delta S/\delta I$ automatically holds in Hamiltonian systems, and is of little interest. Hamiltonian systems will always

contain two action gradients and at least two Euler-Lagrange equations, even if only one is alluded to in the text. The same goes for the action gradient flow equations, defined in Chapter 3. Furthermore, because magnetic field lines are (p, q)-periodic orbits, they will be referred to as such throughout the rest of this thesis in order to keep the discussion as general as possible.

2.5 Relationship Between Lagrangian and Hamiltonian Systems

Sometimes it's more convenient to express magnetic fields as a Lagrangian system instead of a Hamiltonian one. A **Lagrangian system** can be obtained from a Hamiltonian one by setting

$$L(\theta, \dot{\theta}, t) = I(\theta, \dot{\theta}, t)\dot{\theta} - H(I(\theta, \dot{\theta}, t), \theta, t), \tag{2.17}$$

where $I(\theta, \dot{\theta}, t)$ is defined implicitly by $\dot{\theta} = H_I(I, \theta, t)$ [19]. Going backwards, we also have

$$H(I, \theta, t) = I\dot{\theta}(I, \theta, t) - L(\theta, \dot{\theta}(I, \theta, t), t), \tag{2.18}$$

where $\dot{\theta}(I, \theta, t)$ is defined implicitly by $I = L_{\dot{\theta}}(\theta, \dot{\theta}, t)$ [19]. This type of transformation is called a **Legendre transformation**.

It is important to note that this transition bewtween Lagrangian and Hamiltonian systems can only occur when the original system satisfies the **twist condition**, given by

$$H_{II} \neq 0 \tag{2.19}$$

for Hamiltonian systems and

$$L_{\dot{\theta}\dot{\theta}} \neq 0 \tag{2.20}$$

for Lagrangian systems [19]. If the twist condition is not satisfied, then either $\dot{\theta}(I, \theta, t)$ or $I(\theta, \dot{\theta}, t)$ will become multivalued during the transformation, which makes the transformation impossible [19]. Throughout the rest of this thesis, it will be assumed that the twist condition always holds to facilitate comparison between the two approaches and take advantage of the insights gained by transitioning between them.

The main difference between a Lagrangian and a Hamiltonian system is that, for time-independent systems, the Lagrangian formulation describes a system in terms of n variables and n second-order differential equations, where n is the number of degrees of freedom of the system, whereas the Hamiltonian formulation describes a system in terms of $2n$ variables and $2n$ first-order differential equations. Usually, the Hamiltonian formulation is preferred, because it is easier to manipulate using matrices.

2.6 Lagrangian Dynamics

A **path** within the Lagrangian configuration space is a curve defined parametrically by $\theta = \vartheta(t)$ that lies within the covering space $\mathbb{R} \times \mathbb{R}$, and a **$(p, q)$-periodic path** within the configuration space is a path that satisfies

$$\vartheta(t + 2\pi q) = \vartheta(t) + 2\pi p, \tag{2.21}$$

$$\vartheta'(t + 2\pi q) = \vartheta'(t), \tag{2.22}$$

for all $t \in \mathbb{R}$ and some $p, q \in \mathbb{Z}$. The **action** of a Lagrangian system along a (p, q)-periodic path $\theta = \vartheta(t)$ is given by [19]

$$S[\vartheta] = \int_0^{2\pi q} L(\vartheta, \dot{\vartheta}, t)\, \mathrm{d}t, \tag{2.23}$$

and its variation is given by

$$\begin{aligned} \delta S[\vartheta] &= \int_0^{2\pi q} \left(L_\theta\, \delta\vartheta + L_{\dot{\theta}}\, \delta\dot{\vartheta} \right) \mathrm{d}t \\ &= \int_0^{2\pi q} \left(L_\theta - \frac{\mathrm{d}L_{\dot{\theta}}}{\mathrm{d}t} \right) \delta\vartheta\, \mathrm{d}t, \end{aligned} \tag{2.24}$$

where the last line was obtained by using integration by parts (the endpoints cancel due to the periodicity conditions given by Equations (2.21) and (2.22)). However, because S is a functional, the variation in S must be of the form [19]

$$\delta S[\vartheta] = \int_0^{2\pi q} \frac{\delta S}{\delta \theta}\, \delta\vartheta\, \mathrm{d}t, \tag{2.25}$$

so when combined with the previous expression, it can be seen that the action gradient is given by the functional derivative [19]

$$\frac{\delta S}{\delta \theta} = L_\theta - \frac{\mathrm{d}L_{\dot{\theta}}}{\mathrm{d}t}. \tag{2.26}$$

When a (p, q)-periodic path satisfies $\delta S / \delta\theta = 0$ for all t, it is called a **(p, q)-periodic orbit**, and it satisfies **Lagrange's equation**

$$L_\theta - \frac{\mathrm{d}L_{\dot{\theta}}}{\mathrm{d}t} = 0. \tag{2.27}$$

However, if a (p, q)-periodic path fails to satisfy $\delta S / \delta\theta = 0$ for all t, but $\delta S / \delta\theta \approx 0$ still holds up to order ε, then it is called a **(p, q)-periodic pseudo-orbit**. Once again, it can be seen from the definition that (p, q)-periodic pseudo-orbits are generalisations of (p, q)-periodic orbits.

2.7 Poincaré Sections and Iterated Maps

Sometimes it's easier to understand the dynamics of a continuous-time Lagrangian or Hamiltonian system when it's formulated in terms of a discrete-time map. Recall that when a magnetic field is described using Hamiltonian coordinates, the toroidal angle ζ is equivalent to the time t, and because ζ is 2π-periodic, so is t. Suppose that a cross-section of a torus is taken with $\zeta \in [0, 2\pi)$ being held constant, and that every time a magnetic field line passes through the cross-section, its surface label (or Hamiltonian momentum) and poloidal angle are plotted in phase space. This cross-section is called a **Poincaré section**, and the plot itself is called a **Poincaré plot** or **puncture plot** [20]. A schematic diagram of a Poincaré section is shown in Figure 2.1.

The points associated with a Poincaré section or plot define what is known as an iterated map. An **iterated map** is a transformation T of each point of a discrete-time dynamical system such that $\mathbf{x}_{n+1} = T(\mathbf{x}_n)$, where $\mathbf{x}$ is a point in phase space, $n \in \mathbb{Z}$ de-

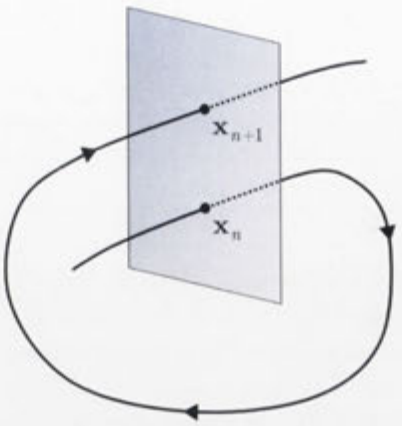

Figure 2.1: Schematic diagram of a Poincaré section.

notes the iteration number and $\mathbf{x}_n$ denotes the value of $\mathbf{x}$ after n iterations of the map [20]. When an iterated map satisfactorily describes the dynamics of a system at discrete, periodic points in time by following the orbits of a continuous-time system from one transversal surface of section until its first return to that particular surface (as shown in Figure 2.1), it is called a **return map**, and is the discrete-time analogue of a continuous-time dynamical system. Return maps retain all the features of continuous-time dynamical systems, except that one degree of freedom has been removed from the description of the system so that an n-dimensional system can easily be plotted in $(n-1)$-dimensional space [20]. This is important because it is much easier to visualise a two-dimensional system than a three-dimensional one, and return maps make it possible to reduce a three-dimensional system to a two-dimensional one without losing significant amounts of important information about the system. It is important to note that there is a subtle difference between the definition of an iterated map and that of a return map. An iterated map is a purely mathematical construction that exists in its own right, whereas a return map is an iterated map that is being used specifically to reduce the dimensionality of a dynamical system.

2.8 Area-Preserving Twist Maps

The return maps of all $1\frac{1}{2}$-d.o.f Hamiltonian systems are area-preserving [21], which means that the absolute value of their Jacobian is unity. Such maps are called **area-preserving maps**, because they preserve the phase space area of their coordinates under transformation. An **area-preserving twist map** is an area-preserving map $T : (x, y) \mapsto (\bar{x}, \bar{y})$ that is periodic in x and satisfies either

$$\left.\frac{\mathrm{d}x}{\mathrm{d}\bar{y}}\right|_{\bar{x}} \leq \kappa < 0 \tag{2.28}$$

or

$$0 < \kappa \leq \left.\frac{\mathrm{d}\bar{x}}{\mathrm{d}y}\right|_{x} \tag{2.29}$$

for some constant κ [7]. In the first case, the untransformed x-coordinate is a monotonically increasing function of the transformed y-coordinate, whereas in the second case, the transformed x-coordinate is a monotonically increasing function of the untransformed

y-coordinate [7]. These two conditions are connected via the relationship [7]

$$\left.\frac{\mathrm{d}x}{\mathrm{d}\bar{y}}\right|_{\bar{x}} \equiv -\left.\frac{\mathrm{d}\bar{x}}{\mathrm{d}y}\right|_{x}, \tag{2.30}$$

which was obtained via the Jacobian matrix of the inverse transformation T^{-1}, from which we can see that area-preserving twist maps can also be formulated in terms of monotonically *decreasing* functions. Because the phase space is cylindrical, the relationship between x and $\bar{y}$ in Equation (2.28) and between $\bar{x}$ and y in Equation (2.29) takes the form of a helix. By convention, twist maps that satisfy Equation (2.28) are said to **twist to the left**, whereas twist maps that satisfy Equation (2.29) are said to **twist to the right** [7]. Area-preserving twist maps have Jacobian unity (not minus unity), and are commonly used to describe Hamiltonian systems in which the velocity depends monotonically on the momentum [7]. It is important to note that despite the label, the second iterate of a twist map is not necessarily a twist map [7]. Throughout the rest of this thesis, it will be assumed that all two-dimensional iterated maps are area-preserving twist maps.

2.9 The Kicked Rotor and the Standard Map

The **kicked rotor** is a pendulum in which the gravity is discretised and periodic [22]. This can be accomplished in numerous ways, one of which is to cause the pendulum support to oscillate vertically and then change to the accelerating reference frame in which the support is motionless [22]. The Hamiltonian of the kicked rotor is given by

$$H(I,\theta,t) = \frac{I^2}{2ml^2} + mg(t)l(1-\cos\theta), \tag{2.31}$$

where

$$g(t) = g_0 \Delta t \sum_{n=-\infty}^{\infty} \delta(t-t_n) \tag{2.32}$$

is the gravity, t is the time, θ is the angle coordinate, I is the momentum, m is the mass, l is the length of the pendulum, g_0 is the average value of $g(t)$, and $\delta(t-t_n)$ is the Dirac delta function [22].

The kicked rotor is inextricably linked to an area-preserving twist map known as the standard map, which twists to the right with unity. The **standard map** is defined by

$$x_{n+1} = x_n + y_{n+1}, \tag{2.33}$$

$$y_{n+1} = y_n - \frac{k}{2\pi}\sin 2\pi x_n, \tag{2.34}$$

where $n \in \mathbb{Z}$, x_n is periodic and k is called the **nonlinearity parameter**. When $k = 0$, the system is integrable and totally free of chaos. As k increases, the amount of chaos also increases. When k exceeds $k_c = 0.971635\ldots$, the value at which the last KAM curves are destroyed, the system is said to be **totally chaotic**, and is filled with cantori (compare Section 1.9) [23, 24]. The breakup of KAM curves under the standard map is shown in Figure 2.2.

Although the working is too complex to be included here, and has been left until Chapter 5, the standard map defines the set of points at which the kicked rotor has stationary action [22]. This is significant, because according to Hamilton's principle of

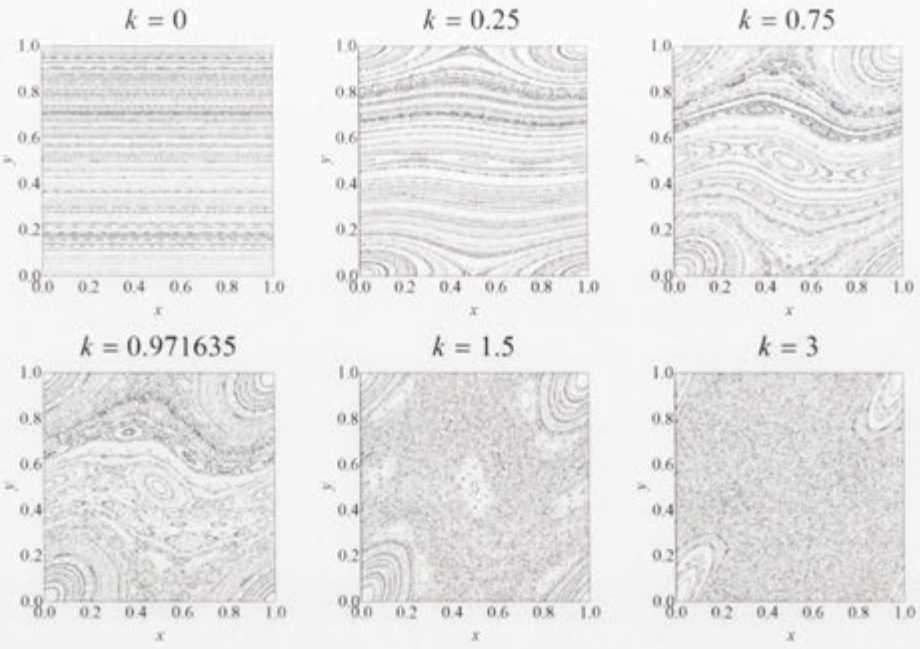

Figure 2.2: Breakup of KAM curves under the standard map.

stationary action, any continuous-time system for which the action is stationary at only discrete, periodic points in time must technically be a discrete-time system, and behave accordingly. This is because an object in motion will never follow a trajectory along which the action isn't stationary, and because the action of the kicked rotor isn't stationary outside the kick, there is no motion there, so the time coordinate of its trajectories must be discrete. Hence, the kicked rotor is merely just the standard map, defined such that the time coordinate takes values in $\mathbb{R}$ instead of $\mathbb{Z}$. If that be the case, then because the standard map is well-known and well-studied, it serves as a **toy model** for better understanding the dynamics of other, more realistic Hamiltonian systems for which the Poincaré sections are described by other, more sophisticated maps that are much more difficult to study. In other words, the kicked rotor is not meant to be a real physical system, but a way of defining a continuous-time system that behaves similarly to a real physical system at certain discrete points in time, without having to perform numerical integrations in order to derive the map associated with it. This makes it easier for us to demonstrate the relationship between continuous-time and discrete-time systems, because in a real physical system, a single Poincaré section will not include *all* the points of stationary action, so this relationship isn't so obvious. Throughout the rest of this thesis, the standard map will be used primarily as a toy model for better understanding the dynamics of toroidally confined plasmas.

Chapter 3

Construction of Almost-Invariant Tori for Continuous-Time Systems

This chapter discusses the transition between integrable and nonintegrable, chaotic systems, and draws on the Poincaré-Birkhoff theorem to conclude that the only two periodic orbits that survive the perturbation of an integrable Hamiltonian system are the action-minimax and action-minimising orbits. It also defines almost-invariant tori for continuous-time Lagrangian and Hamiltonian systems, as well as the pseudo-orbits and almost-invariant curves associated with them. Three different methods are used to construct the almost-invariant tori, including the minimisation of the quadratic flux functional, the minimisation of the action gradient functional, and the determination of the path of steepest descent of the action gradient flow between the action-minimax and action-minimising orbits. These lead to quadratic-flux-minimising (QFMin) tori, action-gradient-minimising (AGMin) tori and ghost tori, respectively. QFMin and AGMin tori are shown to belong to the same class of almost-invariant tori, called generalised AGMin tori, and contrasted with ghost tori in order to demonstrate why QFMin, AGMin and ghost tori need to be made equivalent to or "reconciled" with each other. It is also argued that because of the similarities between QFMin, AGMin and ghost tori, such a reconciliation should be possible by making an appropriate coordinate transformation.

3.1 Invariant Tori and Periodic Orbits

Most objects within a $1\frac{1}{2}$-degree-of-freedom Hamiltonian system change over time. Those that don't are said to be **invariant**, and they have the property that they are mapped onto themselves by the Hamiltonian dynamics [19]. The two main classes of invariant geometrical objects used in dynamical systems theory are **invariant surfaces** and **periodic orbits** [19]. Both concepts are closely related to each other, because invariant surfaces are just the two-dimensional equivalent of a periodic orbit, which is one-dimensional. As such, invariant surfaces are composed entirely of a continuous family of periodic orbits. The magnetic field lines used to confine plasmas are constrained to lie on tori. As such, we will refer to surfaces as **tori** unless we expect the result to hold in more general circumstances.

One of the most important characteristics of invariant tori is that they're integrable. That is, they can be written in terms of action-angle coordinates that give the Hamiltonian the form $H = H_0(I)$, so that it yields an explicit, analytical, closed-form solution. Unfortunately, invariant tori that have rational rotational transform are not structurally stable, and this integrability will always be lost after an arbitrarily small perturbation

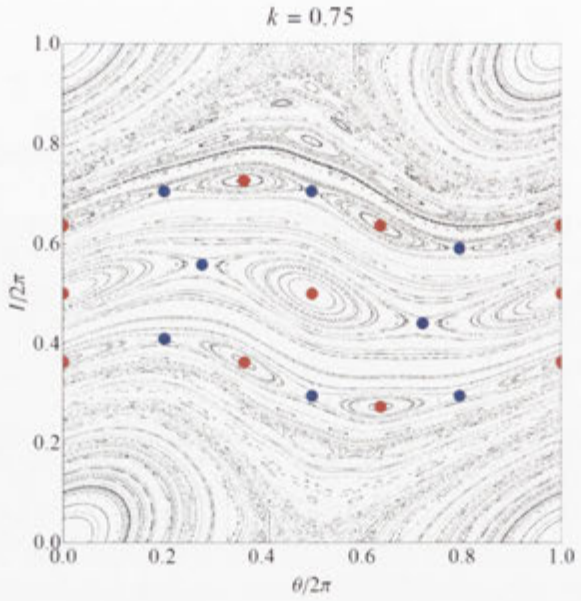

Figure 3.1: Poincaré plot of the action-minimax orbits (red) and the action-minimising orbits (blue) within the standard map for $k = 0.75$, corresponding to $\epsilon = 1/3$, $1/2$ and $2/3$ (in order from bottom to top).

$H = H_0(I) + \varepsilon H_1(I, \theta, t)$ [16]. However, a remarkable fact is that although most periodic orbits are destroyed, an isolated handful still remain, and if the twist condition $H_{II} \neq 0$ holds, then the **Poincaré-Birkhoff theorem** implies that there will be exactly two of them for each island chain with rational rotational transform [16]. This means that we stand a good chance of being able to recreate the periodic orbits to a good approximation after they have been destroyed by a perturbation.

Because the action is a saddle point along one of the remaining periodic orbits, and a minimum along the other, the periodic orbits that survive the perturbation of an invariant torus are called the action-minimax and action-minimising orbits, respectively [16]. The **action-minimax orbit** threads the centres of the islands together [16] like a string threads the centres of the beads inside a necklace, with the number of beads being equal to both the number of islands in the island chain and the denominator of the rational rotational transform. Similarly, the **action-minimising orbit** threads the centres of the points in the chaotic separatrix region at which the separatrices would cross if it weren't for chaos [16]. By analogy, this is the gap between the beads in a necklace. The action-minimax orbit is always stable unless there's a period-doubling bifurcation, in which case it's unstable, whereas the action-minimising orbit is always unstable [16, 17]. A Poincaré plot of the action-minimax and action-minimising orbits associated with the standard map for $k = 0.75$ is shown in Figure 3.1, along with a visualisation of the standard map itself. From this figure, it can be seen that the action-minimax and action-minimising orbits are the O-points and X-points of the island chains, respectively, and that the number of islands in an island chain is equal to the denominator of the rational rotational transform. This is not inconsistent with the definition of the action-minimax and action-minimising orbits, which are defined to be the X-points and O-points of the *action*, respectively, because the islands represent the *energy* of the system, not the action (see Figure 1 of Dewar, Hudson, and Gibson [19]).

3.2 Almost-Invariant Tori and Almost-Invariant Curves

Once an invariant torus has been destroyed by perturbation, it can still be recovered to a best approximation by attempting to "fill in the gaps" between the action-minimax and action-minimising orbits such that they form a torus [16]. Although the new torus will not be invariant, it should be as close to invariance as possible, and is therefore called an **almost-invariant torus**.

In analogy with invariant tori, which are composed of a continuous family of (p, q)-periodic orbits, almost-invariant tori are composed of a continuous family of (p, q)-periodic pseudo-orbits [19]. In Hamiltonian systems, this pseudo-orbit family is given by

$$\theta = \vartheta(t|\theta_0), \tag{3.1}$$

$$I = L_{\dot{\theta}}(\vartheta(t|\theta_0), \dot{\vartheta}(t|\theta_0), t), \quad \forall t \in [0, 2\pi q), \tag{3.2}$$

and in Lagrangian systems, it is given by

$$\theta = \vartheta(t|\theta_0), \tag{3.3}$$

$$\dot{\theta} = H_I(\mathcal{I}(t|\theta_0), \vartheta(t|\theta_0), t), \quad \forall t \in [0, 2\pi q), \tag{3.4}$$

where $\theta_0 = \vartheta(0|\theta_0)$ is a 2π-periodic parameter that varies over the range $\theta_0 \in [0, 2\pi)$ [19].

The Poincaré section of an almost-invariant torus is called an **almost-invariant curve**. As the natural discretisation of an almost-invariant torus with respect to time, almost-invariant curves play a fundamental role in understanding the behaviour of almost-invariant tori. For a continuous-time system, the shape of the almost-invariant curves depends continually on the value of t or ζ at which the cross-section is made. This means that in the case of the simple pendulum, there's only one distinct kind of almost-invariant curve for each definition of an almost-invariant curve. However, in the case of the kicked rotor, defined by Equation (2.31), the discontinuity in the potential means that there are two distinct kinds of almost-invariant curves for each definition, denoted by C^+ and C^-. Both these curves will be defined explicitly in Section 5.6, but for the moment, it is sufficient to know that the C^+ curves are the forward images of the C^- curves under an area-preserving twist map (and vice versa for the backward image) [25].

3.3 The Linear Magnetic Flux

Before attempting to construct some (p, q)-periodic pseudo-orbits and almost-invariant tori, it is necessary to define some flux quantities. The first of these, the linear magnetic flux, often referred to simply as the **magnetic flux**, is defined most generally for an arbitrary closed surface Γ as

$$\varphi_1[\Gamma] = \oiint_\Gamma \mathbf{n} \cdot \mathbf{B} \, \mathrm{d}A, \tag{3.5}$$

where $\mathbf{B}$ is the magnetic field, $\mathbf{n}$ is the unit normal to an arbitrary point on Γ, and $\mathrm{d}A$ is the directed infinitesimal area element of Γ [16, 17]. For a magnetic surface defined in toroidal magnetic coordinates, $\Gamma : I = I_\Gamma(\theta, \zeta)$, so the directed infinitesimal area element is given by

$$\mathrm{d}A = \frac{\mathrm{d}\theta \, \mathrm{d}\zeta}{\mathbf{n} \cdot \boldsymbol{\nabla}\theta \times \boldsymbol{\nabla}\zeta}, \tag{3.6}$$

where θ and ζ are both 2π-periodic. The magnetic flux then becomes [16]

$$\varphi_1[\Gamma] = \int_0^{2\pi} \int_0^{2\pi} \frac{\mathbf{n} \cdot \mathbf{B}}{\mathbf{n} \cdot \boldsymbol{\nabla}\theta \times \boldsymbol{\nabla}\zeta} \, \mathrm{d}\theta \, \mathrm{d}\zeta. \tag{3.7}$$

Because of the continuing lack of evidence to prove the existence of magnetic monopoles, we can safely assume that $\varphi_1 \equiv 0$ provided that the surface is closed, so that φ_1 is independent of both Γ and the coordinates [16]. It is shown in Hudson and Dewar [26] that

$$\frac{\delta S}{\delta \theta} = \frac{\mathbf{n} \cdot \mathbf{B}}{\mathbf{n} \cdot \boldsymbol{\nabla}\theta \times \boldsymbol{\nabla}\zeta}, \tag{3.8}$$

so the magnetic flux can also be written in terms of the action gradient as

$$\varphi_1[\Gamma] = \int_0^{2\pi} \int_0^{2\pi} \frac{\delta S}{\delta \theta} \, \mathrm{d}\theta \, \mathrm{d}\zeta. \tag{3.9}$$

3.4 The Quadratic Magnetic Flux

Because $\varphi_1 \equiv 0$, the linear magnetic flux cannot be used to determine the degree to which Γ deviates from being a magnetic surface, so it is unfit for defining almost-invariant surfaces [27]. It is therefore necessary to define a new flux, the quadratic magnetic flux, which is the second moment of the linear magnetic flux [26]. From now on, the quadratic magnetic flux will be referred to simply as the **quadratic flux**. For an arbitrary closed surface Γ, the most general definition of the quadratic flux is given by

$$\varphi_2[\Gamma] = \frac{1}{2} \oiint_\Gamma \frac{(\mathbf{n} \cdot \mathbf{B})^2}{\mathbf{n} \cdot \mathbf{C}} \, \mathrm{d}A, \tag{3.10}$$

where $\mathbf{C}$ is the cross product of the gradients of each of the coordinates that varies on Γ [26]. For a magnetic surface written in terms of toroidal magnetic coordinates, $\mathbf{C} = \boldsymbol{\nabla}\theta \times \boldsymbol{\nabla}\zeta$, and the quadratic flux becomes [26]

$$\varphi_2[\Gamma] = \frac{1}{2} \int_0^{2\pi} \int_0^{2\pi} \left(\frac{\mathbf{n} \cdot \mathbf{B}}{\mathbf{n} \cdot \boldsymbol{\nabla}\theta \times \boldsymbol{\nabla}\zeta} \right)^2 \mathrm{d}\theta \, \mathrm{d}\zeta. \tag{3.11}$$

Unlike the linear flux, the quadratic flux is not coordinate-independent [26]. However, coordinate independence does still hold in certain situations – specifically, when $\boldsymbol{\nabla} \cdot \mathbf{C} = 0$ and $\mathbf{n} \cdot \mathbf{C} \neq 0$ [26]. The latter should always be satisfied if the coordinates used to describe Γ are suitable for tori [26]. Because the integrand is squared, it can be seen that the quadratic flux is positive definite. As with the linear flux, the quadratic flux can be written in terms of the action gradient [26], which leads to

$$\varphi_2[\Gamma] = \frac{1}{2} \int_0^{2\pi} \int_0^{2\pi} \left(\frac{\delta S}{\delta \theta} \right)^2 \mathrm{d}\theta \, \mathrm{d}\zeta, \tag{3.12}$$

where $\delta S / \delta \theta$ is defined in Equation (3.8). This shows that the quadratic flux is merely the minimisation of the action gradient in least squares over Γ, which explains the need to introduce a peculiar weighting factor $1/(\mathbf{n} \cdot \mathbf{C})$ into the definition of φ_2 [26].

3.5 QFMin Tori and Pseudo-Orbits

The first method of defining an almost-invariant torus is as the minimum of the **quadratic flux functional**

$$\varphi_2[\Gamma] = \frac{1}{2}\int_0^{2\pi}\int_0^{2\pi}\left(\frac{\delta S}{\delta\theta}\right)^2 \mathrm{d}\theta\,\mathrm{d}t \tag{3.13}$$

under arbitrary deformations of an almost-invariant torus Γ. Such tori are called **quadratic-flux-minimising (QFMin) tori**, because they are the tori of least quadratic flux [19]. The Euler-Lagrange equation corresponding to this variational principle can be calculated using both Lagrangian and Hamiltonian dynamics, and both methods have been presented to facilitate comparison. Towards the end of each formulation, it will be seen that QFMin tori are foliated by a family of (p, q)-periodic pseudo-orbits, parametrised by θ_0. The properties of these pseudo-orbits will be discussed in Section 3.5.3.

3.5.1 Lagrangian Formulation of QFMin Tori

In the Lagrangian formulation, we assume that $\theta = \vartheta(t|\theta_0)$, so that the quadratic flux functional becomes [19]

$$\varphi_2[\Gamma] = \frac{1}{2}\int_0^{2\pi}\int_0^{2\pi}\left(\frac{\delta S}{\delta\theta}\right)^2 \frac{\partial\vartheta}{\partial\theta_0}\,\mathrm{d}\theta_0\,\mathrm{d}t. \tag{3.14}$$

The first variation of $\varphi_2[\Gamma]$ is given by

$$\delta\varphi_2[\Gamma] = \int_0^{2\pi}\int_0^{2\pi}\left[\frac{\delta S}{\delta\theta}\,\delta\left(\frac{\delta S}{\delta\theta}\right)\frac{\partial\vartheta}{\partial\theta_0} + \frac{1}{2}\left(\frac{\delta S}{\delta\theta}\right)^2\frac{\partial(\delta\vartheta)}{\partial\theta_0}\right]\mathrm{d}\theta_0\,\mathrm{d}t, \tag{3.15}$$

where we have used the identity

$$\delta\left(\frac{\partial\vartheta}{\partial\theta_0}\right) = \frac{\partial(\delta\vartheta)}{\partial\theta_0}. \tag{3.16}$$

Using integration by parts to eliminate the $\partial(\delta\vartheta)/\partial\theta_0$ term, it can be seen that [19]

$$\delta\varphi_2[\Gamma] = \int_0^{2\pi}\int_0^{2\pi}\frac{\delta S}{\delta\theta}\left[\delta\left(\frac{\delta S}{\delta\theta}\right)\frac{\partial\vartheta}{\partial\theta_0} - \frac{\partial}{\partial\theta_0}\left(\frac{\delta S}{\delta\theta}\right)\delta\vartheta\right]\mathrm{d}\theta_0\,\mathrm{d}t, \tag{3.17}$$

because the endpoints cancel due to the periodicity conditions (Equations (2.21) and (2.22)). Substituting in

$$\frac{\delta S}{\delta\theta} = \frac{\partial L}{\partial\theta} - \frac{\mathrm{d}}{\mathrm{d}t}\frac{\partial L}{\partial\dot{\theta}}, \tag{3.18}$$

$$\delta\left(\frac{\delta S}{\delta\theta}\right) = \frac{\partial(\delta L)}{\partial\theta} - \frac{\mathrm{d}}{\mathrm{d}t}\frac{\partial(\delta L)}{\partial\dot{\theta}}, \tag{3.19}$$

and

$$\delta L = \frac{\partial L}{\partial\theta}\,\delta\vartheta + \frac{\partial L}{\partial\dot{\theta}}\,\delta\dot{\vartheta}, \tag{3.20}$$

where $L = L(\vartheta, \dot{\vartheta}, t)$ and $\dot{\vartheta} = \mathrm{d}\vartheta/\mathrm{d}t$, it follows that the quadratic flux functional can be written in the form

$$\delta\varphi_2[\Gamma] = \int_0^{2\pi}\int_0^{2\pi} \frac{\delta S}{\delta\theta}\left[L_{\dot\theta\dot\theta}\frac{\partial\ddot\vartheta}{\partial\theta_0}\,\delta\vartheta + \frac{\mathrm{d}L_{\dot\theta\dot\theta}}{\mathrm{d}t}\frac{\partial\dot\vartheta}{\partial\theta_0}\,\delta\vartheta - L_{\dot\theta\dot\theta}\frac{\partial\vartheta}{\partial\theta_0}\,\delta\ddot\vartheta - \frac{\mathrm{d}L_{\dot\theta\dot\theta}}{\mathrm{d}t}\frac{\partial\vartheta}{\partial\theta_0}\,\delta\dot\vartheta\right]\mathrm{d}\theta_0\,\mathrm{d}t. \tag{3.21}$$

Using integration by parts to eliminate $\delta\dot\vartheta$ and $\delta\ddot\vartheta$, this can be reduced to

$$\delta\varphi_2[\Gamma] = -\int_0^{2\pi}\int_0^{2\pi}\left\{\frac{\mathrm{d}}{\mathrm{d}t}\left[L_{\dot\theta\dot\theta}\frac{\partial\vartheta}{\partial\theta_0}\frac{\mathrm{d}}{\mathrm{d}t}\left(\frac{\delta S}{\delta\theta}\right)\right] + L_{\dot\theta\dot\theta}\frac{\partial\dot\vartheta}{\partial\theta_0}\frac{\mathrm{d}}{\mathrm{d}t}\left(\frac{\delta S}{\delta\theta}\right)\right\}\delta\vartheta\,\mathrm{d}\theta_0\,\mathrm{d}t, \tag{3.22}$$

because the endpoints cancel due to the periodicity conditions. Assuming that $\theta = \vartheta(t|\theta_0)$ is monotonic – that is,

$$\frac{\partial\vartheta}{\partial\theta_0} > 0 \quad \forall t, \tag{3.23}$$

another integration by parts can be performed over t to yield [19]

$$\delta\varphi_2[\Gamma] = -\int_0^{2\pi}\int_0^{2\pi}\left(\frac{\partial\vartheta}{\partial\theta_0}\right)^{-1}\frac{\mathrm{d}}{\mathrm{d}t}\left[L_{\dot\theta\dot\theta}\left(\frac{\partial\vartheta}{\partial\theta_0}\right)^2\frac{\mathrm{d}}{\mathrm{d}t}\left(\frac{\delta S}{\delta\theta}\right)\right]\delta\vartheta\,\mathrm{d}\theta_0\,\mathrm{d}t, \tag{3.24}$$

where the endpoints cancel due to the periodicity conditions. Since this must be true for all $\delta\vartheta$, it follows that the Euler-Lagrange equation is given by [19]

$$\frac{\mathrm{d}}{\mathrm{d}t}\left[L_{\dot\theta\dot\theta}\left(\frac{\partial\vartheta}{\partial\theta_0}\right)^2\frac{\mathrm{d}}{\mathrm{d}t}\left(\frac{\delta S}{\delta\theta}\right)\right] = 0. \tag{3.25}$$

Surprisingly, this equation can be integrated with respect to t to yield [19]

$$\frac{\delta S}{\delta\theta} = \nu(\theta_0) + \sigma(\theta_0)\int_0^t\left[L_{\dot\theta\dot\theta}\left(\frac{\partial\vartheta}{\partial\theta_0}\right)^2\right]^{-1}\Bigg|_{t\mapsto u}\mathrm{d}u, \tag{3.26}$$

where u is a dummy variable. Assuming that the twist condition $L_{\dot\theta\dot\theta} \neq 0$ holds, the second term is monotonically secular in t whenever $\sigma(\theta_0) \neq 0$. Hence, we must set $\sigma(\theta_0) = 0$ in order to ensure the periodicity of $\delta S/\delta\theta$, which is required to be periodic because of its evaluation on a (p, q)-periodic pseudo-orbit [19]. Hence, the Euler-Lagrange equation is given by

$$\frac{\delta S}{\delta\theta} = \nu(\theta_0), \tag{3.27}$$

where θ_0 parametrises a family of (p, q)-periodic orbits and $\nu(\theta_0)$ is constant with respect to t. This equation is called the **QFMin equation**, and this result is called the **QFMin theorem**.

3.5.2 Hamiltonian Formulation of QFMin Tori

In the Hamiltonian formulation, θ is paramterised by $\theta = \vartheta(t)$, and the first variation in $\varphi_2[\Gamma]$ is given by

$$\delta\varphi_2[\Gamma] = \int_0^{2\pi}\int_0^{2\pi}\frac{\delta S}{\delta\theta}\,\delta\left(\frac{\delta S}{\delta\theta}\right)\mathrm{d}\theta\,\mathrm{d}t. \tag{3.28}$$

Because we are dealing with pseudo-orbits within a Hamiltonian system, $H = H(I, \theta, t)$ and $\delta S/\delta I = 0$. This implies that $\dot{\theta} = H_I$, and by constraining I to lie on an arbitrary torus $I = \rho(\theta, t)$, it can be shown that [19,28]

$$\dot{I} = \rho_t + H_I \rho_\theta. \tag{3.29}$$

Substituting this into Equation (2.13), it can be seen that [19]

$$\begin{aligned} \frac{\delta S}{\delta \theta} &= -\rho_t - H_I \rho_\theta - H_\theta \\ &= -\rho_t - \eth_\theta H, \end{aligned} \tag{3.30}$$

where $\eth_\theta \equiv \partial_\theta + \rho_\theta \partial_I$ denotes the total θ derivative (which would only be partial if the pseudo-orbits weren't constrained to lie on a torus). The first variation of $\delta S/\delta\theta$ is given by [19]

$$\begin{aligned} \delta\left(\frac{\delta S}{\delta \theta}\right) &= -\delta\rho_t - \rho_\theta\, \delta H_I - H_I\, \delta\rho_\theta - \delta H_\theta \\ &= -\delta\rho_t - \rho_\theta H_{II}\, \delta\rho - H_I\, \delta\rho_\theta - H_{I\theta}\, \delta\rho \\ &= -\delta\rho_t - \eth_\theta(H_I)\, \delta\rho - H_I\, \delta\rho_\theta \\ &= -\delta\rho_t - \eth_\theta(H_I\, \delta\rho), \end{aligned} \tag{3.31}$$

which can also be obtained by writing

$$\delta\left(\frac{\delta S}{\delta \theta}\right) = -\delta\rho_t - \eth_\theta(\delta H) \tag{3.32}$$

and substituting $\delta H = H_I\, \delta\rho$ into Equation (3.32) (remember that the pseudo-orbits are constrained to lie on a torus). Substituting Equation (3.31) into Equation (3.28), we obtain

$$\delta\varphi_2[\Gamma] = \int_0^{2\pi}\int_0^{2\pi} \frac{\delta S}{\delta\theta}\left[-\delta\rho_t - \eth_\theta\left(H_I\, \delta\rho\right)\right] \mathrm{d}\theta\, \mathrm{d}t, \tag{3.33}$$

which after integration by parts, becomes [19,28]

$$\begin{aligned} \delta\varphi_2[\Gamma] &= \int_0^{2\pi}\int_0^{2\pi} \left[\left(\frac{\partial}{\partial t} + H_I \frac{\eth}{\eth\theta}\right)\frac{\delta S}{\delta\theta}\right] \delta\rho\, \mathrm{d}\theta\, \mathrm{d}t \\ &= \int_0^{2\pi}\int_0^{2\pi} \frac{\mathrm{d}}{\mathrm{d}t}\left(\frac{\delta S}{\delta\theta}\right) \delta\rho\, \mathrm{d}\theta\, \mathrm{d}t, \end{aligned} \tag{3.34}$$

because the endpoints cancel due to the periodicity conditions (Equations (2.8) and (2.9)). Hence, the Euler-Lagrange equations are given by [19]

$$\frac{\mathrm{d}}{\mathrm{d}t}\left(\frac{\delta S}{\delta\theta}\right) = 0, \tag{3.35}$$

$$\frac{\delta S}{\delta I} = 0, \tag{3.36}$$

although the first equation can be rewritten as [19,28]

$$\frac{\delta S}{\delta\theta} = \nu(\theta_0), \tag{3.37}$$

where θ_0 parametrises a family of (p, q)-periodic orbits and $\nu(\theta_0)$ is constant with respect to t. As expected, this is the same Euler-Lagrange equation that was obtained using the Lagrangian formulation. From now on, we will restrict our attention to Equation (3.37) when discussing the Euler-Lagrange equations of QFMin tori within Hamiltonian systems, and ignore Equation (3.36) almost entirely.

3.5.3 QFMin Pseudo-Orbits

As shown in Sections 3.5.1 and 3.5.2, and verified by Equations (3.37) and (3.36), the surface Γ is foliated by a continuous family of (p, q)-periodic pseudo-orbits. These pseudo-orbits are called **QFMin pseudo-orbits**, and they foliate a **QFMin torus** [19]. When written in terms of the magnetic field, the QFMin equation defined by Equations (3.27) and (3.37) takes the form [26]

$$\mathbf{B}_\nu \cdot \boldsymbol{\nabla}\nu = 0, \tag{3.38}$$

where $\mathbf{B}_\nu \equiv \mathbf{B} - \nu\boldsymbol{\nabla}\theta \times \boldsymbol{\nabla}\zeta$ is called the **pseudo-magnetic field** and $\nu = \mathbf{n}\cdot\mathbf{B}/\mathbf{n}\cdot\boldsymbol{\nabla}\theta\times\boldsymbol{\nabla}\zeta$ is called the **integrability parameter** [26]. This implies both that the QFMin pseudo-orbits are characteristics of the QFMin equation and that they are tangential to the pseudo-magnetic-field [26]. Although the QFMin equation implies that $\nu(\theta_0)$ is constant on each particular pseudo-orbit, it can still vary from one pseudo-orbit to another, because the pseudo-orbits are not required to have the same initial values. In particular, $\nu = 0$ on the action-minimax and action-minimising orbits, and $\nu \neq 0$ elsewhere [26], which is why $\nu(\theta_0)$ is sometimes referred to as the integrability parameter.

3.5.4 QFMin Curves

The Poincaré section of a QFMin torus is called a **QFMin curve**. The two different kinds of QFMin curves have been plotted in Figure 3.2, along with a visualisation of the standard map in order to show how they relate to islands and chaos. A poloidal plot has also been provided in Figure 3.3 in order to show what the QFMin curves would look like inside the topological base space.

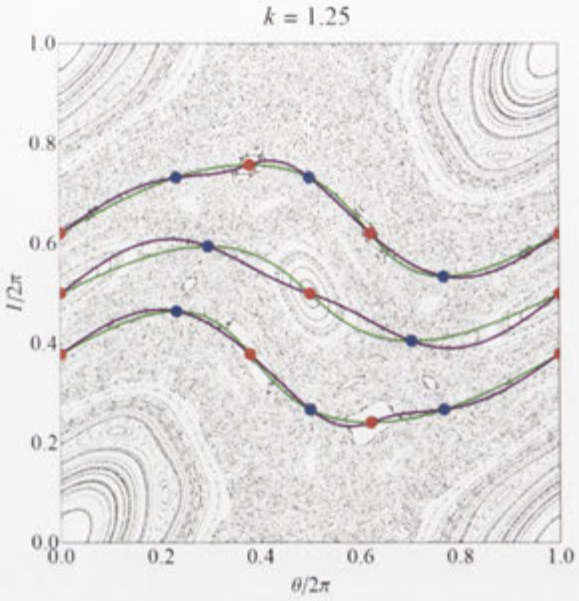

Figure 3.2: QFMin curves plotted in Cartesian coordinates when $k = 1.25$. The green C^+ QFMin curves are the forward images of the purple C^- QFMin curves.

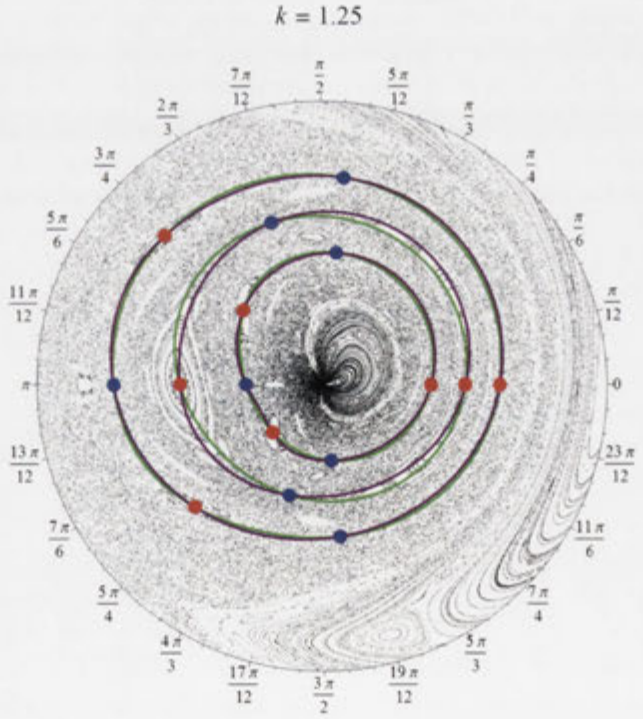

Figure 3.3: QFMin curves plotted in polar coordinates when $k = 1.25$. The green C^+ QFMin curves are the forward images of the purple C^- QFMin curves.

3.6 AGMin Pseudo-Orbits and Tori

The second type of almost-invariant torus can be defined as the foliation of a torus by a series of (p, q)-periodic pseudo-orbits obtained by integrating the square of the action gradient over t but not θ. This new functional is called the **action gradient functional**, and is defined by [19]

$$f[C] = \frac{1}{2}\int_0^{2\pi q}\left(\frac{\delta S}{\delta\theta}\right)^2 \mathrm{d}t, \tag{3.39}$$

where C is an arbitrary (p, q)-periodic path. The action gradient functional is the square of the **action gradient norm** [19]

$$\left\|\frac{\delta S}{\delta\theta}\right\| = \left\langle\frac{\delta S}{\delta\theta}, \frac{\delta S}{\delta\theta}\right\rangle^{1/2} \geq 0, \tag{3.40}$$

where

$$\langle f, g\rangle = \frac{1}{2}\int_0^{2\pi q} fg\,\mathrm{d}t. \tag{3.41}$$

When the action gradient functional is minimised under arbitrary deformations of C, the resulting pseudo-orbit is called an **action-gradient-minimising (AGMin) pseudo-orbit** [19], and when a family of AGMin pseudo-orbits foliate a torus, the resulting torus is called an **AGMin torus**.

3.6.1 Restriction of the AGMin Pseudo-Orbits to Lie on Tori

The original derivation of AGMin pseudo-orbits is shown in Dewar, Hudson, and Gibson [19], but because it's difficult to extend this formulation to encompass AGMin tori as well as AGMin pseudo-orbits, we have decided to introduce a new formulation in this thesis that works just as well for AGMin tori as it does for AGMin pseudo-orbits. This new formulation requires us to modify the action gradient functional in order to make it two-dimensional, by adding a Lagrange multiplier that allows us to drop some of the boundary conditions (that $\vartheta'(0) = \dot{\theta}_0$ and $\vartheta'(2\pi q) = \dot{\theta}_0$) and replace them with the constraint that the area between the AGMin pseudo-orbits $\theta = \vartheta(t)$ and the poloidal axis be constant with respect to t. This is in analogy with the pseudo-action defined in Section 6 of Hudson and Dewar [16], and it goes well beyond answering the third question in the list of open issues at the end of Dewar, Hudson, and Gibson [19].

Because each pseudo-orbit has a different initial value, the area between each pseudo-orbit and the poloidal axis must depend on θ_0 (see Figure 3 of Dewar, Hudson, and Gibson [19]), which means that we can make the Euler-Lagrange equation for AGMin pseudo-orbits (Equations (22) and (31) of Dewar, Hudson, and Gibson [19]) dependent on θ_0 simply by constraining the area between each pseudo-orbit and the poloidal axis to be constant. This turns the Euler-Lagrange equation for AGMin pseudo-orbits into an Euler-Lagrange equation for AGMin tori, by making it depend continuously on θ_0. This is similar to the Euler-Lagrange equation for QFMin tori, which also depends continuously on θ_0. The Lagrange multiplier is necessary to show that AGMin pseudo-orbits foliate a torus, and because it was omitted from the original formulation described by Dewar, Hudson, and Gibson [19], it is worthwhile comparing the original formulation with the one outlined below. The Lagrangian formulation has been presented first, followed by the Hamiltonian formulation.

3.6.2 Lagrangian Formulation of AGMin Tori

In the Lagrangian formulation, C is parametrised by $\theta = \vartheta(t)$, and we introduce the Lagrange multiplier μ in order to constrain

$$\mathcal{A} = \int_0^{2\pi q} \vartheta \, \mathrm{d}t \tag{3.42}$$

to be constant, where $\mathcal{A}$ is the area between an AGMin pseudo-orbit $\theta = \vartheta(t)$ and the poloidal axis. This leads to the modified action gradient functional

$$f[\vartheta, \mu] = \int_0^{2\pi q} \left[\frac{1}{2} \left(\frac{\delta S}{\delta \theta} \right)^2 - \mu \vartheta \right] \mathrm{d}t, \tag{3.43}$$

which has variation

$$\delta f[\vartheta, \mu] = \int_0^{2\pi q} \left[\frac{\delta S}{\delta \theta} \, \delta \left(\frac{\delta S}{\delta \theta} \right) - \mu \, \delta \vartheta \right] \mathrm{d}t, \tag{3.44}$$

where

$$\delta \left(\frac{\delta S}{\delta \theta} \right) = L_{\theta\theta} \, \delta \vartheta - \frac{\mathrm{d} L_{\theta\dot{\theta}}}{\mathrm{d}t} \, \delta \vartheta - \frac{\mathrm{d} L_{\dot{\theta}\dot{\theta}}}{\mathrm{d}t} \, \delta \dot{\vartheta} - L_{\dot{\theta}\dot{\theta}} \, \delta \ddot{\vartheta}. \tag{3.45}$$

Substituting Equation (3.45) into Equation (3.44) and integrating by parts to remove the time derivative from $\delta\dot{\vartheta}$ and $\delta\ddot{\vartheta}$ yields

$$\delta f[\vartheta, \mu] = \int_0^{2\pi q} \left[\frac{\delta S}{\delta \theta} \left(L_{\theta\theta} - \frac{\mathrm{d} L_{\theta\dot{\theta}}}{\mathrm{d}t} \right) + \frac{\mathrm{d}}{\mathrm{d}t} \left(\frac{\delta S}{\delta \theta} \frac{\mathrm{d} L_{\dot{\theta}\dot{\theta}}}{\mathrm{d}t} \right) - \frac{\mathrm{d}^2}{\mathrm{d}t^2} \left(\frac{\delta S}{\delta \theta} L_{\dot{\theta}\dot{\theta}} \right) - \mu \right] \delta \vartheta \, \mathrm{d}t, \tag{3.46}$$

where the endpoints cancel due to the periodicity conditions (Equations (2.21) and (2.22)). By rearranging some of the derivatives, this equation can be simplified to

$$\delta f[\vartheta, \mu] = \int_0^{2\pi q} \left\{ \left(L_{\theta\theta} - \frac{\mathrm{d} L_{\theta\dot{\theta}}}{\mathrm{d}t} \right) \frac{\delta S}{\delta \theta} - \frac{\mathrm{d}}{\mathrm{d}t} \left[L_{\dot{\theta}\dot{\theta}} \frac{\mathrm{d}}{\mathrm{d}t} \left(\frac{\delta S}{\delta \theta} \right) \right] - \mu \right\} \delta \vartheta \, \mathrm{d}t. \tag{3.47}$$

Because Equation (3.47) must be minimised over all variations $\delta\vartheta$, we obtain three Euler-Lagrange equations, given by

$$\left(L_{\theta\theta} - \frac{\mathrm{d} L_{\theta\dot{\theta}}}{\mathrm{d}t} \right) \frac{\delta S}{\delta \theta} - \frac{\mathrm{d}}{\mathrm{d}t} \left[L_{\dot{\theta}\dot{\theta}} \frac{\mathrm{d}}{\mathrm{d}t} \left(\frac{\delta S}{\delta \theta} \right) \right] = \mu, \tag{3.48}$$

$$\mu = \mu(\mathcal{A}), \tag{3.49}$$

$$\mathcal{A} = \int_0^{2\pi q} \vartheta \, \mathrm{d}t. \tag{3.50}$$

In order to determine how $\mathcal{A}$ depends on θ_0, we split off the linear part of $\vartheta(t)$, which gives

$$\vartheta(t) = \theta_0 + \iota t + \tilde{\vartheta}(t), \tag{3.51}$$

where the nonlinear component

$$\tilde{\vartheta}(t) \equiv \theta(\theta_0 + \iota t) - \iota t - \langle \theta(\theta_0 + \iota t) - \iota t \rangle \tag{3.52}$$

is defined such that it averages to zero over one full (p, q)-periodic pseudo-orbit. Then, because $\tilde{\vartheta}(t)$ averages to zero, we get

$$\int_0^{2\pi q} \vartheta \, \mathrm{d}t = \int_0^{2\pi q} (\theta_0 + \iota t) \, \mathrm{d}t = 2\pi q(\theta_0 + \pi p), \tag{3.53}$$

from which we can see that

$$\mathcal{A} = 2\pi q(\theta_0 + \pi p). \tag{3.54}$$

Substituting Equation (3.54) into Equation (3.49), and Equation (3.49) into Equation (3.48), it can be seen that because p is constant on each AGMin torus, the Euler-Lagrange equations for AGMin tori can be reduced to the single Euler-Lagrange equation

$$\left(L_{\theta\theta} - \frac{\mathrm{d}L_{\theta\dot{\theta}}}{\mathrm{d}t}\right)\frac{\delta S}{\delta \theta} - \frac{\mathrm{d}}{\mathrm{d}t}\left[L_{\dot{\theta}\dot{\theta}}\frac{\mathrm{d}}{\mathrm{d}t}\left(\frac{\delta S}{\delta \theta}\right)\right] = \mu(\theta_0). \tag{3.55}$$

Note that although $\delta S/\delta\theta$ cannot be reduced to a constant as in the case of QFMin tori, it still satisfies the pseudo-dynamics defined in Chapter 2.

3.6.3 Hamiltonian Formulation of AGMin Tori

In the Hamiltonian formulation, the constraint $\mathcal{A} = \int_0^{2\pi q} \vartheta \, \mathrm{d}t$ and the Lagrange multiplier μ are preserved, but a second Lagrange multiplier is introduced in order to implement the constraint $\delta S/\delta I = 0$. Because C can be parametrised by both $\theta = \vartheta(t)$ and $I = \mathcal{I}(t)$, the action gradient functional is given by

$$f[\mathcal{I}, \vartheta, \lambda, \mu] = \int_0^{2\pi q} \left[\frac{1}{2}\left(\frac{\delta S}{\delta \theta}\right)^2 - \lambda\frac{\delta S}{\delta I} - \mu\vartheta\right] \mathrm{d}t, \tag{3.56}$$

and has variation

$$\delta f[\mathcal{I}, \vartheta, \lambda, \mu] = \int_0^{2\pi q} \left[\frac{\delta S}{\delta \theta}\,\delta\left(\frac{\delta S}{\delta \theta}\right) - \lambda\,\delta\left(\frac{\delta S}{\delta I}\right) - \mu\,\delta\vartheta\right] \mathrm{d}t. \tag{3.57}$$

Taking the variations of $\delta S/\delta\theta$ and $\delta S/\delta I$, it can be seen that

$$\delta\left(\frac{\delta S}{\delta \theta}\right) = -\delta\dot{\mathcal{I}} - H_{I\theta}\,\delta\mathcal{I} - H_{\theta\theta}\,\delta\vartheta, \tag{3.58}$$

$$\delta\left(\frac{\delta S}{\delta I}\right) = \delta\dot{\vartheta} - H_{II}\,\delta\mathcal{I} - H_{I\theta}\,\delta\vartheta. \tag{3.59}$$

Substituting these into Equation (3.57) and using integration by parts to eliminate $\delta\dot{\vartheta}$ and $\delta\dot{\mathcal{I}}$ yields

$$\begin{aligned}\delta f[\mathcal{I}, \vartheta, \lambda, \mu] = \int_0^{2\pi q} \Bigg\{ &\left[\frac{\mathrm{d}}{\mathrm{d}t}\left(\frac{\delta S}{\delta \theta}\right) - H_{I\theta}\frac{\delta S}{\delta \theta} + \lambda H_{II}\right]\delta\mathcal{I} \\ &+ \left[\frac{\mathrm{d}\lambda}{\mathrm{d}t} + H_{I\theta}\lambda - H_{\theta\theta}\frac{\delta S}{\delta \theta} - \mu\right]\delta\vartheta\Bigg\}\,\mathrm{d}t,\end{aligned} \tag{3.60}$$

where the endpoints cancel due to the periodicity conditions (Equations (2.8) and (2.9)). Because this has to be zero for all variations $\delta\mathcal{I}$ and $\delta\vartheta$, we obtain five Euler-Lagrange

equations, given by

$$\frac{\mathrm{d}}{\mathrm{d}t}\left(\frac{\delta S}{\delta \theta}\right) - H_{I\theta}\frac{\delta S}{\delta \theta} + \lambda H_{II} = 0, \tag{3.61}$$

$$\frac{\mathrm{d}\lambda}{\mathrm{d}t} + H_{I\theta}\lambda - H_{\theta\theta}\frac{\delta S}{\delta \theta} - \mu = 0, \tag{3.62}$$

$$\frac{\delta S}{\delta I} = 0, \tag{3.63}$$

$$\mu = \mu(\mathcal{A}), \tag{3.64}$$

$$\mathcal{A} = \int_0^{2\pi q} \vartheta \, \mathrm{d}t. \tag{3.65}$$

Assuming that the twist condition $H_{II} \neq 0$ also holds, Equation (3.61) can be written as

$$\lambda = \frac{1}{H_{II}}\left(H_{I\theta} - \frac{\mathrm{d}}{\mathrm{d}t}\right)\frac{\delta S}{\delta \theta}, \tag{3.66}$$

where $\mathrm{d}/\mathrm{d}t$ is an operator acting on everything to its right. Substituting Equation (3.54) into Equation (3.64), and Equations (3.66) and (3.64) into Equation (3.62), it can be seen that the Euler-Lagrange equations for AGMin tori can be reduced to the two Euler-Lagrange equations

$$\left[\left(\frac{\mathrm{d}}{\mathrm{d}t} + H_{I\theta}\right)\frac{1}{H_{II}}\left(\frac{\mathrm{d}}{\mathrm{d}t} - H_{I\theta}\right) + H_{\theta\theta}\right]\frac{\delta S}{\delta \theta} = -\mu(\theta_0), \tag{3.67}$$

$$\frac{\delta S}{\delta I} = 0, \tag{3.68}$$

where the sign reversal was necessary to facilitate comparison with Dewar, Hudson, and Gibson [19]. From now on, we will restrict our attention to Equation (3.67) when discussing the Euler-Lagrange equations of AGMin tori within Hamiltonian systems, and ignore Equation (3.68) almost entirely.

3.6.4 AGMin Curves

The Poincaré section of an AGMin torus is called an **AGMin curve**. The two different kinds of AGMin curves have been plotted in Figure 3.4, along with a visualisation of the standard map in order to show how they relate to islands and chaos.

3.7 Generalised AGMin Pseudo-Orbits and Tori

QFMin and AGMin pseudo-orbits belong to a larger class of (p, q)-periodic pseudo-orbits called **generalised AGMin pseudo-orbits**, and by extension, QFMin and AGMin tori belong to a larger class of almost-invariant tori called **generalised AGMin tori**. In order to demonstrate this relationship, it is necessary to formulate a variational principle by solving the Euler-Lagrange equation for QFMin pseudo-orbits. We begin by taking the average of both sides of Equation (3.27) over one full (p, q)-periodic QFMin pseudo-orbit with respect to t. This gives

$$\nu(\theta_0) = \frac{1}{2\pi q}\int_0^{2\pi q} \frac{\delta S}{\delta \theta} \, \mathrm{d}t. \tag{3.69}$$

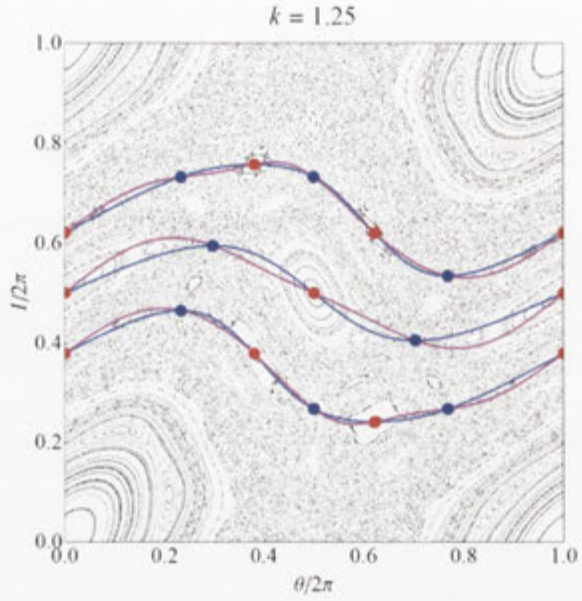

Figure 3.4: AGMin curves plotted in Cartesian coordinates when $k = 1.25$. The blue C^+ AGMin curves are the forward images of the magenta C^- AGMin curves.

We then define the **orbit-average projection operator**

$$\bar{\mathbb{P}}\left(\frac{\delta S}{\delta\theta}\right) = \frac{1}{2\pi q}\int_0^{2\pi q}\frac{\delta S}{\delta\theta}\,\mathrm{d}t, \tag{3.70}$$

so we can write Equation (3.69) as

$$\bar{\mathbb{P}}\left(\frac{\delta S}{\delta\theta}\right) = \nu(\theta_0). \tag{3.71}$$

In order to project out the fluctuating part of $\delta S/\delta\theta$, we also define

$$\tilde{\mathbb{P}}\left(\frac{\delta S}{\delta\theta}\right) = (\mathbb{1} - \bar{\mathbb{P}})\,\frac{\delta S}{\delta\theta}, \tag{3.72}$$

so that the combination of Equations (3.27), (3.69) and (3.71) can be written as

$$\tilde{\mathbb{P}}\left(\frac{\delta S}{\delta\theta}\right) = 0. \tag{3.73}$$

We now define a **variational principle** for QFMin pseudo-orbits by integrating the square of Equation (3.73) over one full (p, q)-periodic QFMin pseudo-orbit with respect to t. This defines

$$\mathcal{V}[\vartheta] = \frac{1}{2}\int_0^{2\pi q}\left[\tilde{\mathbb{P}}\left(\frac{\delta S}{\delta\theta}\right)\right]^2\mathrm{d}t, \tag{3.74}$$

where $\theta = \vartheta(t)$ is a (p, q)-periodic QFMin pseudo-orbit. Clearly, $\mathcal{V}[\vartheta] \geq 0$ with equality if and only if Equation (3.73) is satisfied. That is, $\mathcal{V}[\vartheta]$ is minimised (to zero) by QFMin

pseduo-orbits. Invoking the computational formula for the variance, we also have

$$\int_0^{2\pi q} \left[\tilde{\mathbb{P}}\left(\frac{\delta S}{\delta\theta}\right)\right]^2 \mathrm{d}t = \int_0^{2\pi q} \left(\frac{\delta S}{\delta\theta}\right)^2 \mathrm{d}t - \frac{1}{2\pi q}\left(\int_0^{2\pi q} \frac{\delta S}{\delta\theta}\,\mathrm{d}t\right)^2, \tag{3.75}$$

so the objective functional for QFMin pseudo-orbits is given by

$$\mathcal{V}[\vartheta] = \frac{1}{2}\int_0^{2\pi q} \left(\frac{\delta S}{\delta\theta}\right)^2 \mathrm{d}t - \frac{1}{4\pi q}\left(\int_0^{2\pi q} \frac{\delta S}{\delta\theta}\,\mathrm{d}t\right)^2. \tag{3.76}$$

Comparing this to the modified action gradient functional

$$f[\vartheta,\mu] = \int_0^{2\pi q} \left[\frac{1}{2}\left(\frac{\delta S}{\delta\theta}\right)^2 - \mu\vartheta\right] \mathrm{d}t, \tag{3.77}$$

it's easy to see that QFMin and AGMin pseudo-orbits belong to the same class of pseudo-orbits, defined as the minimum of

$$f[\vartheta] = \frac{1}{2}\int_0^{2\pi q} \left(\frac{\delta S}{\delta\theta}\right)^2 \mathrm{d}t - \eta[\vartheta] \tag{3.78}$$

along an arbitrary (p,q)-periodic path $\theta = \vartheta(t)$. These pseudo-orbits are called **generalised AGMin pseudo-orbits**, and they correspond to QFMin pseudo-orbits when

$$\eta[\vartheta] = \frac{1}{4\pi q}\left(\int_0^{2\pi q} \frac{\delta S}{\delta\theta}\,\mathrm{d}t\right)^2 \tag{3.79}$$

and to AGMin pseudo-orbits when

$$\eta[\vartheta] = \mu\int_0^{2\pi q} \vartheta\,\mathrm{d}t. \tag{3.80}$$

It is worth comparing this with the AGMin pseudo-orbits defined in Dewar, Hudson, and Gibson [19], where $\eta[\vartheta] = 0$. When generalised AGMin pseudo-orbits foliate a torus, the torus is called a **generalised AGMin torus**. Hence, QFMin and AGMin tori are both special cases of generalised AGMin tori.

3.8 Ghost Pseudo-Orbits and Tori

A third way to define an almost-invariant torus is by creating a family of pseudo-orbits by flowing down the path of steepest descent of the action gradient [26]. Beginning at an action-minimax orbit, which is a saddle point of the action, an almost-invariant torus called a **ghost torus** is formed by flowing down the action gradient along the path of steepest descent on both sides of the saddle until an action-minimising orbit is reached [26]. The path of steepest descent is given by the **action gradient flow equation**, which can be formulated in terms of both Lagrangian and Hamiltonian dynamics.

3.8.1 Lagrangian Formulation of Ghost Tori

In the Lagrangian case, the (p,q)-periodic pseudo-orbits are parametrised by $\theta = \vartheta(t)$, and the action gradient flow is given by [19,26]

$$\frac{\mathrm{D}\vartheta}{\mathrm{D}\tau} = -\frac{\delta S}{\delta \theta}, \tag{3.81}$$

where τ is a continuous, timelike parameter and $\mathrm{D}/\mathrm{D}\tau$ represents the total τ-derivative at fixed t. Because $\delta S/\delta\theta = 0$ on the action-minimax and action-minimising orbits, the action gradient flow $\mathrm{D}\vartheta/\mathrm{D}\tau$ also equals zero along these orbits. This makes it difficult to calculate ghost tori numerically, because as $\mathrm{D}\vartheta/\mathrm{D}\tau \to 0$, the amount of time it takes to calculate a point on a ghost torus approaches infinity.

3.8.2 Hamiltonian Formulation of Ghost Tori

In the Hamiltonian case, the Lagrangian equation for the action gradient flow still holds. However, a second equation must also be specified in order to implement the constraint $\delta S/\delta I = 0$ [19]. In order to determine this equation, we note that in phase space, (p,q)-periodic pseudo-orbits are parametrised by $\theta = \vartheta(t)$ and $I = \mathcal{I}(t)$, and they satisfy the relationship

$$\frac{\delta S}{\delta I} = \vartheta'(t) - H_I = 0. \tag{3.82}$$

Taking the total derivative of this equation with respect to τ, it follows that [19]

$$\frac{\mathrm{D}}{\mathrm{D}\tau}\left(\frac{\delta S}{\delta I}\right) = \frac{\mathrm{D}}{\mathrm{D}\tau}\left(\frac{\mathrm{d}\vartheta}{\mathrm{d}t} - H_I\right) = 0. \tag{3.83}$$

Because t and τ are independent variables, their derivatives can be interchanged without affecting the original equation [19]. Making this interchange, and noting that

$$\frac{\mathrm{D}H_I}{\mathrm{D}\tau} = H_{I\theta}\frac{\mathrm{D}\vartheta}{\mathrm{D}\tau} + H_{II}\frac{\mathrm{D}\mathcal{I}}{\mathrm{D}\tau}, \tag{3.84}$$

we arrive at

$$\frac{\mathrm{d}}{\mathrm{d}t}\left(\frac{\mathrm{D}\vartheta}{\mathrm{D}\tau}\right) - H_{I\theta}\frac{\mathrm{D}\vartheta}{\mathrm{D}\tau} - H_{II}\frac{\mathrm{D}\mathcal{I}}{\mathrm{D}\tau} = 0. \tag{3.85}$$

Substituting Equation (3.81) into Equation (3.85), and assuming that the twist condition $H_{II} \neq 0$ holds, Equation (3.85) can be rearranged to yield [19]

$$\frac{\mathrm{D}\mathcal{I}}{\mathrm{D}\tau} = \frac{1}{H_{II}}\left(H_{I\theta} - \frac{\mathrm{d}}{\mathrm{d}t}\right)\frac{\delta S}{\delta\theta}, \tag{3.86}$$

where $\mathrm{d}/\mathrm{d}t$ is considered to be an operator acting on everything to its right. Hence, the action gradient flow of a ghost torus can be completely described in Hamiltonian phase space by using the two Hamiltonian equations

$$\frac{\mathrm{D}\vartheta}{\mathrm{D}\tau} = -\frac{\delta S}{\delta\theta}, \tag{3.87}$$

$$\frac{\mathrm{D}\mathcal{I}}{\mathrm{D}\tau} = \frac{1}{H_{II}}\left(H_{I\theta} - \frac{\mathrm{d}}{\mathrm{d}t}\right)\frac{\delta S}{\delta\theta}. \tag{3.88}$$

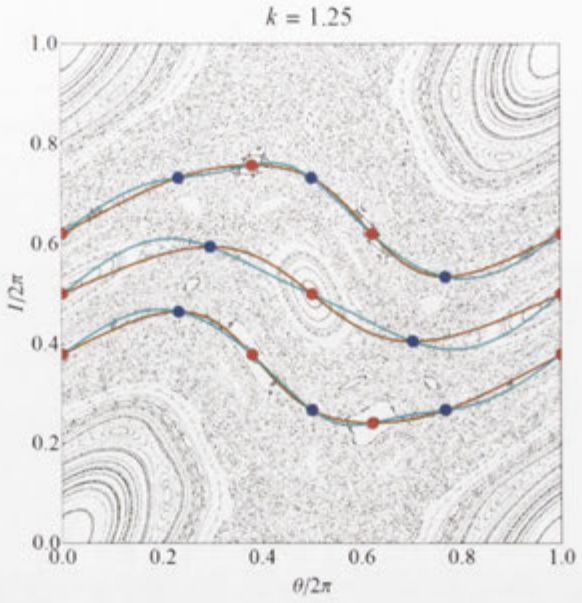

Figure 3.5: Ghost curves plotted in Cartesian coordinates when $k = 1.25$. The orange C^+ ghost curves are the forward images of the cyan C^- ghost curves.

From now on, we will restrict our attention to Equation (3.87) when discussing the action gradient flow equations of ghost tori within Hamiltonian systems, and ignore Equation (3.88) almost entirely.

3.8.3 Ghost Pseudo-Orbits

According to Hudson and Dewar [16], ghost tori are named after the fact that they are the "ghostly remnants" of invariant tori. Like QFMin and AGMin tori, ghost tori are foliated by a continuous family of (p, q)-periodic pseudo-orbits, called **ghost pseudo-orbits** [26]. However, ghost pseudo-orbits are typically parametrised by τ, rather than θ_0, in order to emphasise their dependence on the time dependence of the action gradient flow equation.

3.8.4 Ghost Curves

The Poincaré section of a ghost torus is called a **ghost curve**. The two different kinds of ghost curves have been plotted in Figure 3.5, along with a visualisation of the standard map in order to show how they relate to islands and chaos.

3.9 Comparison of Almost-Invariant Tori

Based on Figures 3.2–3.5, it's easy to question whether there's any difference between QFMin, AGMin and ghost tori. Indeed, Figure 3.6 shows that QFMin, AGMin and ghost curves are virtually indistinguishable inside weakly chaotic systems. However, as k is increased, the differences between QFMin, AGMin and ghost curves become more and more noticeable, and by the time the system is strongly chaotic, there's little doubt that QFMin, AGMin and ghost tori are distinct. It's interesting to note that, according to Figure 3.7, the trajectories of AGMin and ghost curves are much closer to each other than those of QFMin and AGMin curves, and those of QFMin and ghost curves. The

reason for this is unclear, but it could have something to do with the relationship between Equations (3.66) and (3.88). One might be tempted to think that because of the low accuracy of the computational algorithm used to plot AGMin curves, AGMin and ghost curves might be equivalent to each other. However, the inconsistency of Equation (3.66) with Equation (3.88) precludes this from happening [19]. It's also interesting to note that the AGMin and ghost curves cross each other at points where the action is not extremised, but the reasons for this and the significance of it remain unclear.

QFMin and AGMin curves are superior to ghost curves in the sense that they can both be calculated one pseudo-orbit at a time rather than requiring the construction of an infinite set of pseudo-orbits via a flow. They are also superior to ghost curves in the sense that QFMin curves are defined in terms of flux leakage [17], which gives them a clear physical interpretation, and this physical interpretation can be extended to AGMin curves via Equation (3.78). However, QFMin and AGMin curves also have inferior mathematical properties because they violate the **graph property** for high k, meaning that they cross lines of constant θ multiple times in (θ, I)-space, so $I(\theta)$ is not unique [16]. This can be seen in Figure 3.8, which shows what the QFMin curves look like when $k = 3.33$. Unfortunately, the lowest k value at which the graph property is violated decreases as the order of the approximation of the rational rotational transform to an irrational rotational transform increases. Practically, this would restrict the use of QFMin and AGMin tori to rational rotational transforms that are very low-order approximations to irrational ones, because convergence would be difficult to characterise in these circumstances, and would result in a very distorted mesh for the coordinates.

Fortunately, it has been proven by Golé [12] that in the case of area-preserving twist maps, ghost tori satisfy the graph property, so they can represent physical field lines, as can be seen by comparing the plot of the ghost curves for $k = 3.33$ shown in Figure 3.9 with the analogous plot of the QFMin curves shown in Figure 3.8. However, ghost tori are difficult to construct numerically because the amount of time it takes to find a point on a ghost curve tends to infinity as $\delta S/\delta\theta \to 0$ [16]. There are ways to circumvent this problem if $\delta S/\delta\theta$ is much greater than zero on most parts of the ghost curve, but the current solutions are less than ideal. Fortunately, because of the similarities between QFMin, AGMin and ghost curves shown in Figure 3.6, there's a strong chance that either QFMin or AGMin tori can be made equivalent to ghost tori by making an appropriate coordinate transformation. The process of making two different types of almost-invariant tori equivalent to each other is called **reconciliation**, and when the reconciliation process has been completed, the resulting almost-invariant tori are said to be **reconciled**.

The advantage of reconciling QFMin, AGMin and ghost tori is that it causes the QFMin and AGMin curves to take on the properties of ghost curves, such as satisfaction of the graph property, while allowing the ghost curves to take on the properties of QFMin and AGMin curves, such as ease of numerical computability. The latter is facilitated by the fact that if ghost curves can be reconciled with either QFMin or AGMin curves, then they could also be calculated by using the same methods as for QFMin and AGMin curves, which are typically a lot easier to implement numerically than those that are used for ghost curves. The **primary goal** of this thesis is to find a coordinate transformation that reconciles either QFMin or AGMin tori with ghost tori, and to demonstrate its existence. Although it's well beyond the scope of this thesis, Hudson and Breslau [29] have shown that ghost curves have similar trajectories to temperature isotherms, which suggests that there may be a coordinate transformation that reconciles them as well. This would be very significant, because it would imply that ghost tori are more than just mathematical

a construct, but a physical entity, and it could be extended to both QFMin and AGMin tori on the basis of a proven reconciliation with ghost tori.

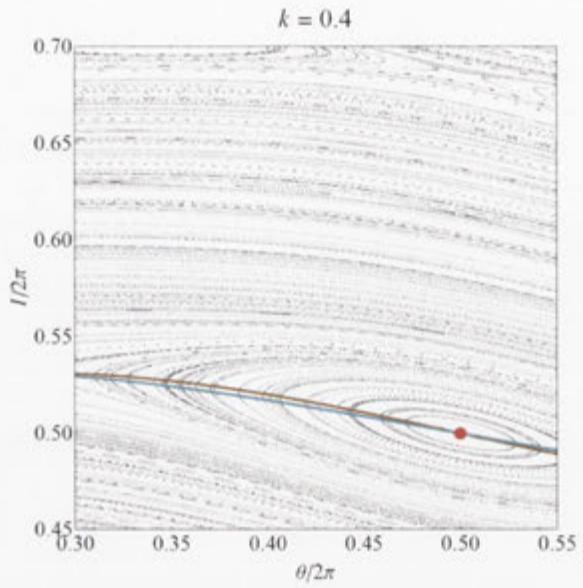

Figure 3.6: QFMin, AGMin and ghost curves plotted for $\epsilon = 1/2$ when $k = 0.4$. Although all curves have been plotted, only the orange C^+ ghost curve and the cyan C^- ghost curve can be seen because of the similarities between each type of curve (either C^+ or C^-) and the thickness of the lines. In other words, the C^+ curves are virtually indistinguishable from each other, as are the C^- curves in this weakly chaotic system.

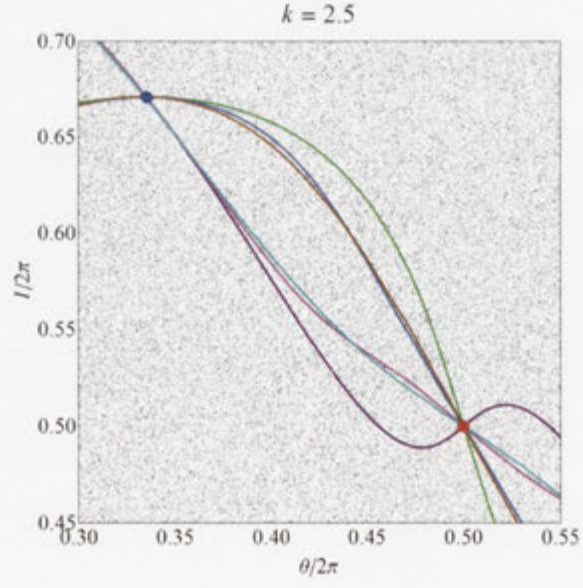

Figure 3.7: QFMin, AGMin and ghost curves plotted for $\epsilon = 1/2$ when $k = 2.5$. The green curve is the C^+ QFMin curve, the blue curve is the C^+ AGMin curve, the orange curve is the C^+ ghost curve, the cyan curve is the C^- ghost curve, the magenta curve is the C^- AGMin curve and the purple curve is the C^- QFMin curve. Notice that all six curves are clearly distinct from each other in this strongly chaotic system.

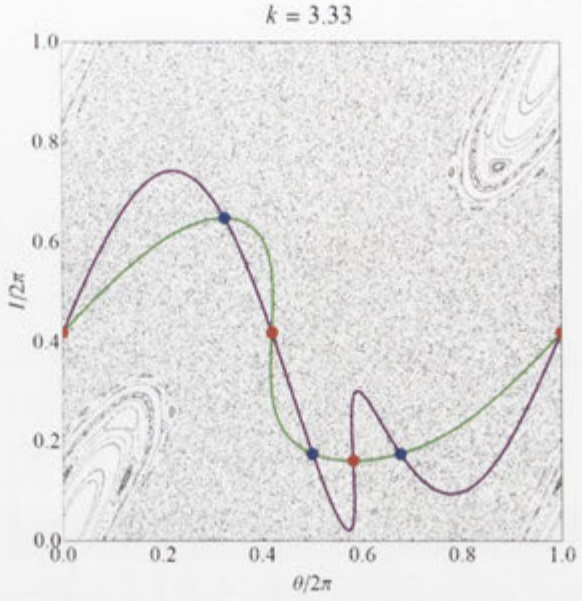

Figure 3.8: QFMin curves plotted for $\epsilon = 1/3$ when $k = 3.33$. These curves violate the graph property because $I(\theta)$ is not unique for the green C^+ QFMin curve when $\theta/2\pi \approx 0.42$ and for the purple C^- QFMin curve when $\theta/2\pi \approx 0.58$.

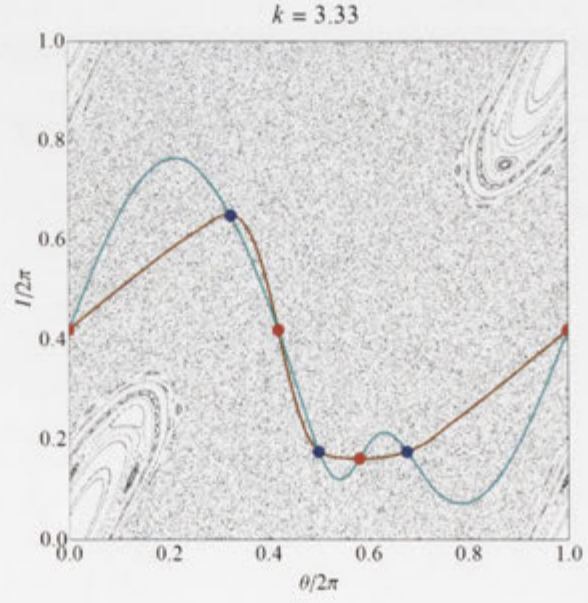

Figure 3.9: Ghost curves plotted for $\epsilon = 1/3$ when $k = 3.33$. The orange C^+ ghost curves and the cyan C^- ghost curves do not violate the graph property like their corresponding QFMin curves do.

Chapter 4

Reconciliation of Almost-Invariant Tori for Continuous-Time Systems

This chapter begins by proving an important theorem that reduces the number of almost-invariant tori that need to be reconciled from three to two. This is accomplished by showing that any reconciliation between QFMin and ghost tori is also a reconciliation between QFMin-ghost tori and AGMin tori. After that, a new poloidal angle Θ is introduced in order to carry out the reconciliation between QFMin and ghost tori via a coordinate transformation, and the Lagrangian and Hamiltonian pseudo-dynamics is defined in order to eliminate the functional dependence of Θ on I and $\dot{\theta}$. Next, QFMin and ghost tori are defined in terms of Θ, and the reconciliation condition is refined to the point where it is shown to be a linear function of the time t. Finally, a variational principle is constructed that will be discretised in Chapter 6 so that the reconciliation between QFMin and ghost tori can be carried out numerically in Chapters 7 and 8.

4.1 The Rigidity Principle for Almost-Invariant Tori

Considering the advantages and disadvantages of the various approaches to defining almost-invariant tori, as well as the similarities between them when plotted in phase space, it seems logical to seek a coordinate transformation that will make the various types of almost-invariant tori equivalent. This problem is greatly simplified by the **rigidity principle for almost-invariant tori**, which states

Theorem (Rigidity principle for almost-invariant tori). *If two of QFMin, AGMin and ghost pseudo-orbits are reconciled with each other, then they must also be reconciled with the third.*

This is due to the underlying structure of the QFMin, AGMin and ghost pseudo-orbits themselves, which makes it impossible to reconcile two of them without also reconciling the third. The rigidity principle also leads to an important corollary, which states

Corollary. *If two of QFMin, AGMin and ghost pseduo-orbits cannot be reconciled with each other, then neither of them can be reconciled with the third.*

Although it is possible to prove the rigidity principle in all cases, for the purposes of this thesis, we will restrict our attention to the case where QFMin and ghost pseudo-orbits are already reconciled, and the rigidity principle is needed to show that they are also reconciled with AGMin pseudo-orbits, because the other cases are analogous to this one, and superfluous to the aim of this thesis. The Hamiltonian formulation of the proof is presented first, followed by the Lagrangian formulation.

Proof. **Hamiltonian Formulation**

Recall that a family of QFMin pseudo-orbits parametrised by θ_0 satisfies

$$\frac{\delta S}{\delta \theta} = \nu(\theta_0). \tag{4.1}$$

Then substituting in Equation (2.13) and taking the total derivative with respect to τ gives

$$\frac{\mathrm{D}}{\mathrm{D}\tau}\left(\frac{\delta S}{\delta \theta}\right) = -\frac{\mathrm{D}}{\mathrm{D}\tau}\left(\frac{\mathrm{d}I}{\mathrm{d}t} + H_\theta\right) = \nu'(\theta_0)\theta_0'(\tau). \tag{4.2}$$

Because t and τ are independent of each other, their derivatives can be interchanged without affecting the equation. Making this interchange, expanding $\mathrm{D}H_\theta/\mathrm{D}\tau$ as

$$\frac{\mathrm{D}H_\theta}{\mathrm{D}\tau} = H_{\theta\theta}\frac{\mathrm{D}\theta}{\mathrm{D}\tau} + H_{I\theta}\frac{\mathrm{D}I}{\mathrm{D}\tau}, \tag{4.3}$$

and substituting it into Equation (4.2) yields

$$-\left(\frac{\mathrm{d}}{\mathrm{d}t} + H_{I\theta}\right)\frac{\mathrm{D}I}{\mathrm{D}\tau} - H_{\theta\theta}\frac{\mathrm{D}\theta}{\mathrm{D}\tau} = \nu'(\theta_0)\theta_0'(\tau). \tag{4.4}$$

Assuming that the QFMin pseudo-orbits are also ghost pseudo-orbits, they must satisfy Equations (3.87) and (3.88), given by

$$\frac{\mathrm{D}\theta}{\mathrm{D}\tau} = -\frac{\delta S}{\delta \theta}, \tag{4.5}$$

$$\frac{\mathrm{D}I}{\mathrm{D}\tau} = \frac{1}{H_{II}}\left(H_{I\theta} - \frac{\mathrm{d}}{\mathrm{d}t}\right)\frac{\delta S}{\delta \theta}. \tag{4.6}$$

Substituting these into Equation (4.4) yields

$$\left[\left(\frac{\mathrm{d}}{\mathrm{d}t} + H_{I\theta}\right)\frac{1}{H_{II}}\left(\frac{\mathrm{d}}{\mathrm{d}t} - H_{I\theta}\right) + H_{\theta\theta}\right]\frac{\delta S}{\delta \theta} = \nu'(\theta_0)\theta_0'(\tau). \tag{4.7}$$

Comparing this with Equation (3.67) and making the identification $\mu(\theta_0) = \nu'(\theta_0)\theta_0'(\tau) = \nu'(\theta_0)/\tau'(\theta_0)$, we can see that this is one of the Hamiltonian Euler-Lagrange equations for AGMin pseudo-orbits (the other, that $\delta S/\delta I = 0$, has already been assumed right from the outset of this proof). □

Proof. **Lagrangian Formulation**

Recall that a family of QFMin pseudo-orbits parametrised by θ_0 satisfies

$$\frac{\delta S}{\delta \theta} = \nu(\theta_0). \tag{4.8}$$

Then substituting in Equation (2.27) and taking the total derivative with respect to τ gives

$$\frac{\mathrm{D}}{\mathrm{D}\tau}\left(\frac{\delta S}{\delta \theta}\right) = \frac{\mathrm{D}}{\mathrm{D}\tau}\left(L_\theta - \frac{\mathrm{d}L_{\dot\theta}}{\mathrm{d}t}\right) = \nu'(\theta_0)\theta_0'(\tau). \tag{4.9}$$

Because t and τ are independent of each other, their derivatives can be interchanged without affecting the equation. Making this interchange, expanding $\mathrm{D}L_\theta/\mathrm{D}\tau$ and $\mathrm{D}L_{\dot\theta}/\mathrm{D}\tau$

as

$$\frac{\mathrm{D}L_\theta}{\mathrm{D}\tau} = L_{\theta\theta}\frac{\mathrm{D}\theta}{\mathrm{D}\tau} + L_{\theta\dot{\theta}}\frac{\mathrm{D}\dot{\theta}}{\mathrm{D}\tau}, \tag{4.10}$$

$$\frac{\mathrm{D}L_{\dot{\theta}}}{\mathrm{D}\tau} = L_{\theta\dot{\theta}}\frac{\mathrm{D}\theta}{\mathrm{D}\tau} + L_{\dot{\theta}\dot{\theta}}\frac{\mathrm{D}\dot{\theta}}{\mathrm{D}\tau}, \tag{4.11}$$

and substituting them back into Equation (4.9) gives

$$L_{\theta\theta}\frac{\mathrm{D}\theta}{\mathrm{D}\tau} + L_{\theta\dot{\theta}}\frac{\mathrm{D}\dot{\theta}}{\mathrm{D}\tau} - \frac{\mathrm{d}}{\mathrm{d}t}\left(L_{\theta\dot{\theta}}\frac{\mathrm{D}\theta}{\mathrm{D}\tau} + L_{\dot{\theta}\dot{\theta}}\frac{\mathrm{D}\dot{\theta}}{\mathrm{D}\tau}\right) = \nu'(\theta_0)\theta_0'(\tau). \tag{4.12}$$

Assuming that the QFMin pseudo-orbits are also ghost pseudo-orbits, they must satisfy Equation (3.81), given by

$$\frac{\mathrm{D}\theta}{\mathrm{D}\tau} = -\frac{\delta S}{\delta\theta}, \tag{4.13}$$

and because the derivatives of t and τ can be interchanged, we also have

$$\frac{\mathrm{D}\dot{\theta}}{\mathrm{D}\tau} = \frac{\mathrm{d}}{\mathrm{d}t}\left(\frac{\mathrm{D}\theta}{\mathrm{D}\tau}\right) = -\frac{\mathrm{d}}{\mathrm{d}t}\left(\frac{\delta S}{\delta\theta}\right). \tag{4.14}$$

Substituting these back into Equation (4.12) gives

$$L_{\theta\theta}\frac{\delta S}{\delta\theta} + L_{\theta\dot{\theta}}\frac{\mathrm{d}}{\mathrm{d}t}\left(\frac{\delta S}{\delta\theta}\right) - \frac{\mathrm{d}}{\mathrm{d}t}\left[L_{\theta\dot{\theta}}\frac{\delta S}{\delta\theta} + L_{\dot{\theta}\dot{\theta}}\frac{\mathrm{d}}{\mathrm{d}t}\left(\frac{\delta S}{\delta\theta}\right)\right] = \nu'(\theta_0)\theta_0'(\tau), \tag{4.15}$$

and expanding out the third term yields

$$\left(L_{\theta\theta} - \frac{\mathrm{d}L_{\theta\dot{\theta}}}{\mathrm{d}t}\right)\frac{\delta S}{\delta\theta} - \frac{\mathrm{d}}{\mathrm{d}t}\left[L_{\dot{\theta}\dot{\theta}}\frac{\mathrm{d}}{\mathrm{d}t}\left(\frac{\delta S}{\delta\theta}\right)\right] = \nu'(\theta_0)\theta_0'(\tau). \tag{4.16}$$

Comparing this with Equation (3.55) and making the identification $\mu(\theta_0) = \nu'(\theta_0)\theta_0'(\tau) = \nu'(\theta_0)/\tau'(\theta_0)$, we can see that this is one of the Lagrangian Euler-Lagrange equations for AGMin pseudo-orbits. □

Hence, if QFMin and ghost pseudo-orbits are reconciled with each other in either a Lagrangian or a Hamiltonian system, then they must also be reconciled with AGMin pseudo-orbits. Because the kicked rotor can be defined as both a continuous-time and a discrete-time system, we will assume from now on that the rigidity principle not only holds for continuous-time systems, but also for discrete-time systems under the kicked rotor (i.e. those that satisfy the standard map). Therefore, we will restrict our attention to reconciling QFMin and ghost tori, and ignore AGMin tori almost entirely throughout the rest of this thesis.

4.2 The Pseudo-Action

In order to complete the reconciliation between QFMin and ghost tori, it is necessary to find a coordinate transformation that makes both QFMin and ghost tori equivalent. This is done by introducing a new, generalised poloidal angle $\Theta = \Theta(I, \theta, t)$ that modifies the action, because the action is the only quantity that appears in the definitions of both QFMin and ghost tori [16]. However, in order to derive some of the conditions that are

necessary for the reconciliation to hold, it is important to express the pseudo-dynamics of the reconciled QFMin-ghost tori in terms of the **pseudo-action**, defined by [16]

$$S_\nu = S - \nu\mathcal{A}, \tag{4.17}$$

where S is the standard physical action, ν is a constant chosen to be equal to the value of $\delta S/\delta\Theta$ on some reconciled QFMin-ghost pseudo-orbit, and $\mathcal{A}$ is a constraint given by

$$\mathcal{A} = \int_0^{2\pi q} \Theta \, \mathrm{d}t = \text{const.} \tag{4.18}$$

The constraint $\mathcal{A}$ represents the area between a path $\mathbf{r} = \mathbf{r}(t)$ on a torus and the poloidal axis of the torus [16]. We have sufficient freedom to choose $\Theta = \Theta_0 + \iota t + \tilde{\Theta}(t)$ as a trial function, where Θ_0 is the value of Θ at $t = 0$ and $\tilde{\Theta}$ is a periodic function that averages to zero [16]. For a (p, q)-periodic pseudo-orbit, this implies that [16]

$$\mathcal{A} = 2\pi q(\Theta_0 + \pi p). \tag{4.19}$$

Because p and q are constant on each particular pseudo-orbit, we can uniquely parametrise the pseudo-orbits by constraining $\mathcal{A}$ to be a different constant on each (p, q)-periodic pseudo-orbit. With this unique parametrisation, $\mathbf{r}(\Theta, t) = \mathbf{r}(t|\Theta_0)$, where $\Theta \in [0, 2\pi)$, defines a family of pseudo-orbits that's all-sufficient to specify an almost-invariant torus [16].

In a magnetic field, the constraint $\mathcal{A}$ takes the form

$$\mathcal{A} = \oint_C \Theta \boldsymbol{\nabla}\zeta \cdot \mathbf{dl} = \int_0^{2\pi q} \Theta \, \mathrm{d}\zeta = \text{const}, \tag{4.20}$$

where C is an arbitrary curve on the torus. By defining a new vector pseudo-potential $\mathbf{A}_\nu = \mathbf{A} - \nu\Theta\boldsymbol{\nabla}\zeta$, it can be seen that the constraint $\mathcal{A}$ arises naturally from the original, physical action [16]. As it will be shown in Sections 4.3 and 4.4, the pseudo-action has the effect of simplifying the pseudo-dynamics of a particular QFMin pseudo-orbit that has action gradient equal to ν. This leads to a rather startling result concerning the dependence of Θ on one of its arguments, that will be demonstrated in Section 4.5.

4.3 Hamiltonian Pseudo-Dynamics

Recall that for a $1\frac{1}{2}$-degree-of-freedom Hamiltonian system written in terms of action-angle coordinates, the action along a (p, q)-periodic path $\theta = \vartheta(t)$, $I = \mathcal{I}(t)$ is given by

$$S[\vartheta, \mathcal{I}] = \int_0^{2\pi q} \left[\mathcal{I}\dot{\vartheta} - H\left(\mathcal{I}, \vartheta, t\right)\right] \mathrm{d}t. \tag{4.21}$$

It follows from Equations (4.17) and (4.18) that the Hamiltonian pseudo-action S_ν along a (p, q)-periodic path is given by [16]

$$S_\nu[\vartheta, \mathcal{I}] = \int_0^{2\pi q} \left[\mathcal{I}\dot{\vartheta} - H\left(\mathcal{I}, \vartheta, t\right) - \nu\Theta\left(\mathcal{I}, \vartheta, t\right)\right] \mathrm{d}t. \tag{4.22}$$

We than define the **pseudo-Hamiltonian** as [16]

$$H_\nu \equiv H + \nu\Theta, \tag{4.23}$$

so that the Hamiltonian pseudo-action can be written as

$$S_\nu[\vartheta, \mathcal{I}] = \int_0^{2\pi q} \left[\mathcal{I}\dot{\vartheta} - H_\nu\left(\mathcal{I}, \vartheta, t\right)\right] \mathrm{d}t. \tag{4.24}$$

Then the pseudo-action gradients are given by [16]

$$\frac{\delta S_\nu}{\delta \theta} = -\dot{\mathcal{I}} - \partial_\theta H_\nu, \tag{4.25}$$

$$\frac{\delta S_\nu}{\delta I} = \dot{\vartheta} - \partial_I H_\nu. \tag{4.26}$$

Unlike the original Hamiltonian action gradients, which are only equal to zero for all t on (p, q)-periodic orbits, the Hamiltonian pseudo-action gradients are only equal to zero for all t on QFMin pseudo-orbits that have the same action gradient as that which was used to define the pseudo-action gradient. In such cases, the QFMin pseudo-orbits satisfy the modified Hamilton's equations [16]

$$\dot{\vartheta} = \partial_I H_\nu, \tag{4.27}$$

$$\dot{\mathcal{I}} = -\partial_\theta H_\nu, \tag{4.28}$$

which are analogous to Hamilton's equations for (p, q)-periodic orbits. Note that when $\nu = 0$, as in the case of (p, q)-periodic orbits, the Hamiltonian pseudo-dynamics reduces to ordinary Hamiltonian dynamics.

4.4 Lagrangian Pseudo-Dynamics

In order to facilitate comparison with Hamiltonian pseudo-dynamics, Lagrangian systems can also be defined in terms of the pseudo-action, in which case, the action

$$S[\vartheta] = \int_0^{2\pi q} L(\vartheta, \dot{\vartheta}, t)\, \mathrm{d}t \tag{4.29}$$

along a (p, q)-periodic path $\vartheta(t)$ is replaced by the Lagrangian pseudo-action, given by [16]

$$S_\nu[\vartheta] = \int_0^{2\pi q} \left[L(\vartheta, \dot{\vartheta}, t) - \nu\Theta(\vartheta, \dot{\vartheta}, t)\right] \mathrm{d}t. \tag{4.30}$$

We then define the **pseudo-Lagrangian** as [16]

$$L_\nu \equiv L - \nu\Theta, \tag{4.31}$$

from which it follows by comparing Equations (4.24) and (4.30) that

$$L_\nu = \mathcal{I}\dot{\vartheta} - H_\nu. \tag{4.32}$$

Then the Lagrangian pseudo-action takes the form

$$S_\nu[\vartheta] = \int_0^{2\pi q} L_\nu(\vartheta, \dot{\vartheta}, t)\, \mathrm{d}t \tag{4.33}$$

and the pseudo-action gradient is given by [16]

$$\frac{\delta S_\nu}{\delta \theta} = \frac{\partial L_\nu}{\partial \theta} - \frac{\mathrm{d}}{\mathrm{d}t}\left(\frac{\partial L_\nu}{\partial \dot{\theta}}\right). \tag{4.34}$$

Unlike the original Lagrangian action gradient, which is only equal to zero for all t on (p,q)-periodic orbits, the Lagrangian pseudo-action gradient is only equal to zero for all t on QFMin pseudo-orbits that have the same action gradient as that which was used to define the pseudo-action gradient. In such cases, the QFMin pseudo-orbits satisfy the modified Lagrange's equation [16]

$$\frac{\partial L_\nu}{\partial \theta} - \frac{\mathrm{d}}{\mathrm{d}t}\left(\frac{\partial L_\nu}{\partial \dot{\theta}}\right) = 0, \tag{4.35}$$

which is analogous to Lagrange's equation for (p,q)-periodic orbits. Note that when $\nu = 0$, as in the case of (p,q)-periodic orbits, the Lagrangian pseudo-dynamics reduces to ordinary Lagrangian dynamics.

4.5 The Initial Reconciliation Condition

The **reconciliation condition** is a constraint placed upon $\Theta(I,\theta,t)$ in order to ensure that under the transformation $\theta \mapsto \Theta(I,\theta,t)$, QFMin and ghost tori are equal. As a first step towards obtaining the best reconciliation condition we can get, we must check that the pseudo-dynamics defined in Sections 4.3 and 4.4 are consistent with the definition of a (p,q)-periodic pseudo-orbit, defined in Chapter 2. Recall that on a (p,q)-periodic pseudo-orbit, $\delta S/\delta I$ is always equal to zero, whereas $\delta S/\delta\theta$ varies from one pseudo-orbit to another and is only equal to zero when the pseudo-orbit coincides with a periodic orbit. This implies via Equation (2.14) that

$$\dot{\theta} = H_I, \tag{4.36}$$

which must be consistent with Equation (4.27) in order for the reconciliation to hold. Substituting Equation (4.36) into Equation (4.27) gives [16]

$$H_I = \partial_I H_\nu \equiv H_I + \partial_I(\nu\Theta), \tag{4.37}$$

which implies that

$$\partial_I(\nu\Theta) = 0. \tag{4.38}$$

Because ν is constant on each particular pseudo-orbit, $\nu_I = 0$, and because $\nu \neq 0$ in general, it follows that [16]

$$\Theta_I = 0. \tag{4.39}$$

Hence, Θ is independent of I, so it has the form

$$\Theta = \Theta(\theta, t). \tag{4.40}$$

This implies that when the reconciled QFMin-ghost pseudo-orbits are transformed back into the original coordinate system, they have the form [16,17]

$$\theta = \vartheta(\Theta, t) = \vartheta(t|\Theta_0), \tag{4.41}$$

where Θ_0 is the value of Θ at $t = 0$. Hence, the reconciled QFMin-ghost pseudo-orbits can be parametrised by their initial values. Equation (4.39) will be called the **initial reconciliation condition**, and it will be considerably improved upon in Section 4.8.

4.6 Modified QFMin Tori

In order to reconcile QFMin and ghost tori, it is necessary to generalise the definition of the quadratic flux such that $\theta \mapsto \Theta(\theta, t)$. For an arbitrary torus Γ, the **modified quadratic flux** is given by [16,17]

$$\varphi_2[\Gamma] = \frac{1}{2}\int_0^{2\pi}\int_0^{2\pi}\left(\frac{\delta S}{\delta\Theta}\right)^2 \mathrm{d}\Theta\,\mathrm{d}t, \tag{4.42}$$

where $\delta S/\delta\Theta$ is the modified action gradient. By definition, the reconciled QFMin-ghost tori are the minima of Equation (4.42) under all possible variations of Γ. The Euler-Lagrange equation of the modified quadratic flux can be obtained by taking the functional derivative of Equation (4.17) with respect to θ, which gives [16,17]

$$\frac{\delta S_\nu}{\delta\theta} \equiv \frac{\delta S}{\delta\theta} - \nu\Theta_\theta = 0. \tag{4.43}$$

Rearranging this equation, it can be seen that the Euler-Lagrange equation of the modified quadratic flux is given by

$$\vartheta_\Theta \frac{\delta S}{\delta\theta} = \nu(\theta_0), \tag{4.44}$$

where $\vartheta = \vartheta(\Theta, t)$ is the functional inverse of $\Theta = \Theta(\theta, t)$ with respect to θ. However, because

$$\frac{\delta S}{\delta\Theta} = \vartheta_\Theta \frac{\delta S}{\delta\theta}, \tag{4.45}$$

it follows that the Euler-Lagrange equation of the modified quadratic flux can also be written in the form [26]

$$\frac{\delta S}{\delta\Theta} = \nu(\Theta_0), \tag{4.46}$$

where Θ_0 coincides with θ_0 because Θ and θ both have the same initial conditions.

In analogy with Equation (3.8), the modified action gradient takes the form

$$\frac{\delta S}{\delta\Theta} = \frac{\mathbf{n}\cdot\mathbf{B}}{\mathbf{n}\cdot\boldsymbol{\nabla}\Theta\times\boldsymbol{\nabla}\zeta} \tag{4.47}$$

for a magnetic field, so the modified quadratic flux can be written as

$$\varphi_2[\Gamma] = \frac{1}{2}\int_0^{2\pi}\int_0^{2\pi}\left(\frac{\mathbf{n}\cdot\mathbf{B}}{\mathbf{n}\cdot\boldsymbol{\nabla}\Theta\times\boldsymbol{\nabla}\zeta}\right)^2 \mathrm{d}\Theta\,\mathrm{d}\zeta. \tag{4.48}$$

Moreover, in analogy to Equation (3.38), the Euler-Lagrange equation for modified QFMin

tori within a magnetic field can be written in the form [26]

$$\mathbf{B}_\nu \cdot \boldsymbol{\nabla}\nu = 0, \tag{4.49}$$

where $\mathbf{B}_\nu = \mathbf{B} - \nu\boldsymbol{\nabla}\Theta \times \boldsymbol{\nabla}\zeta$ and $\nu = \mathbf{n} \cdot \mathbf{B}/\mathbf{n} \cdot \boldsymbol{\nabla}\Theta \times \boldsymbol{\nabla}\zeta$.

4.7 Modified Ghost Tori

It is also necessary to generalise the definition of a ghost torus by generalising the definition of the action gradient flow. As Hudson and Dewar [16] have shown, it isn't necessary to define the ghost tori in terms of Θ in order to complete the reconciliation. However, it was also shown by Dewar, Hudson, and Gibson [17] that defining the ghost tori in terms of Θ led to a simpler and much more elegant solution. Hence, we will define the modified ghost tori in terms of Θ.

In the same manner that we defined the modified QFMin tori, we take the original definition of ghost tori and replace θ with $\Theta(\theta, t)$. Then the **modified action gradient flow equation** is given by [17]

$$\frac{\mathrm{D}\Theta}{\mathrm{D}T} = -\frac{\delta S}{\delta\Theta}, \tag{4.50}$$

where T is a continuous, timelike parameter equivalent to τ. Hence, the reconciled QFMin-ghost tori satisfy Equation (4.50). As long as we stick to dealing with Lagrangian systems, there's no need to specify an equivalent equation for $\mathrm{D}\mathcal{I}/\mathrm{D}\tau$. The modified ghost tori are defined by flowing down the modified action gradient along the path of steepest descent from an action-minimax to an action-minimising orbit.

4.8 The Enhanced Reconciliation Condition

In order for the QFMin and ghost tori to be reconciled, the pseudo-orbits defined by Equations (4.40) and (4.41) must satisfy [17] both the modified QFMin Euler-Lagrange equation

$$\frac{\delta S}{\delta\Theta} \equiv \vartheta_\Theta \frac{\delta S}{\delta\theta} = \nu(\Theta_0) \tag{4.51}$$

and the modified action gradient flow equation

$$\frac{\mathrm{D}\Theta}{\mathrm{D}T} = -\frac{\delta S}{\delta\Theta}. \tag{4.52}$$

Hence, the reconciliation condition we derived in Section 4.5 can be improved by solving Equations (4.51) and (4.52) simultaneously. This is accomplished by eliminating $\delta S/\delta\Theta$ between these equations and expanding $\mathrm{D}\Theta/\mathrm{D}T$ as

$$\frac{\mathrm{D}\Theta}{\mathrm{D}T} = \frac{\mathrm{D}\Theta}{\mathrm{D}\Theta_0}\frac{\mathrm{D}\Theta_0}{\mathrm{D}T}, \tag{4.53}$$

so that the reconciliation condition becomes [17]

$$\frac{\mathrm{D}\Theta}{\mathrm{D}\Theta_0} = -T'(\Theta_0)\nu(\Theta_0), \tag{4.54}$$

where we have assumed that $\mathrm{D}\Theta_0/\mathrm{D}T$ is a continuous function and can therefore be inverted. It follows that Θ_0 and T must be functionally dependent on each other, because

otherwise, Equations (4.53) and (4.54) would be identically zero, and that would imply that Equations (4.51) and (4.52) were also identically zero, and unless ϑ were independent of Θ (in which case, the transformation would be impossible), $\delta S/\delta\theta$ would also have to be identically zero, thus meaning that ghost curves do not exist [16,17]. Hence, Θ_0 and T must represent the same family of pseudo-orbits in all but the most trivial of systems (in which case the QFMin and ghost tori are already reconciled). We assume that we have sufficient freedom to choose [17]

$$T'(\Theta_0)\nu(\Theta_0) = -1 \tag{4.55}$$

in order to satisfy the periodicity condition described at the end of this section, in which case the reconciliation condition can be reduced to just

$$\frac{\mathrm{D}\Theta}{\mathrm{D}\Theta_0} = 1. \tag{4.56}$$

Integrating both sides with respect to Θ, it can be seen that Θ is of the form [30]

$$\Theta(t|\Theta_0) = \Theta_0 + f(t). \tag{4.57}$$

We also assume that we have sufficient freedom to choose the trial function [30]

$$f(t) = \iota t, \tag{4.58}$$

where ι is the rational rotational transform $\iota = p/q$ corresponding to mutually prime integers p and q, so that the reconciliation condition becomes [17]

$$\Theta(t|\Theta_0) = \Theta_0 + \iota t \tag{4.59}$$

and the reconciled QFMin-ghost pseudo-orbits are straight lines in (Θ, t)-space. It is a necessary condition for the reconciliation of QFMin and ghost tori that Θ satisfies the periodicity condition [17]

$$\Theta(t|\Theta_0 + 2\pi) = \Theta(t|\Theta_0) + 2\pi, \tag{4.60}$$

and by performing the integration

$$\int_0^{2\pi} \frac{\mathrm{D}\Theta}{\mathrm{D}\Theta_0}\,\mathrm{d}\Theta_0 = \int_0^{2\pi} 1\,\mathrm{d}\Theta_0 = 2\pi, \tag{4.61}$$

it is easy to see that this condition is satisfied.

4.9 The Variational Principle

Having established that the reconciliation condition is given by $\Theta = \Theta_0 + \iota t$, we now seek to determine $\theta = \vartheta(t|\Theta_0)$ by inverting $\Theta(\theta, t)$. Unfortunately, we are not likely to obtain an analytical solution to this problem, so we determine a variational principle that can be used to calculate $\theta = \vartheta(t|\Theta_0)$ numerically. Because the reconciled QFMin-ghost tori must satisfy Equation (4.51), we take both sides of this equation and calculate the average over one full (p, q)-periodic orbit with respect to t. This gives [30]

$$\bar{\mathbb{P}}\left(\vartheta_\Theta \frac{\delta S}{\delta\theta}\right) = \nu(\Theta_0), \tag{4.62}$$

where $\bar{\mathbb{P}}$ is the orbit-average projection operator

$$\bar{\mathbb{P}}\left(\vartheta_\Theta \frac{\delta S}{\delta \theta}\right) = \frac{1}{2\pi q} \int_0^{2\pi q} \vartheta_\Theta \frac{\delta S}{\delta \theta} \, \mathrm{d}t. \tag{4.63}$$

For simplicity, we also define an operator $\tilde{\mathbb{P}}$ such that

$$\tilde{\mathbb{P}}\left(\vartheta_\Theta \frac{\delta S}{\delta \theta}\right) = \left(\mathbb{1} - \bar{\mathbb{P}}\right) \vartheta_\Theta \frac{\delta S}{\delta \theta} \tag{4.64}$$

to project out the fluctuating part of $\vartheta_\Theta(\delta S/\delta\theta)$ [30], which in the light of Equations (4.51) and (4.62) gives

$$\tilde{\mathbb{P}}\left(\vartheta_\Theta \frac{\delta S}{\delta \theta}\right) = 0 \tag{4.65}$$

for each point on a modified QFMin pseudo-orbit. Replacing $\delta S/\delta\Theta$ with $\tilde{\mathbb{P}}\left(\vartheta_\Theta \, \delta S/\delta\theta\right)$ in Equation (4.42), we arrive at the **variational principle for reconciled QFMin-ghost pseudo-orbits** [30]

$$\mathcal{V}[\vartheta] = \frac{1}{2} \int_0^{2\pi} \int_0^{2\pi} \left[\tilde{\mathbb{P}}\left(\vartheta_\Theta \frac{\delta S}{\delta \theta}\right)\right]^2 \Bigg|_{\Theta=\Theta_0+\iota t} \mathrm{d}\Theta_0 \, \mathrm{d}t, \tag{4.66}$$

where ϑ is a (p,q)-periodic pseudo-orbit, ι is the rational rotational transform $\iota = p/q$ corresponding to mutually prime integers p and q, and we have assumed that the reconciliation condition $\mathrm{D}\Theta/\mathrm{D}\Theta_0 = 1$ holds. The substitution of $\Theta = \Theta_0 + \iota t$ into the equation is necessary in order to ensure that the resulting QFMin tori are also ghost tori. Note that in contrast to the variational principles defined in Section 3.7, this variational principle contains an integral over both t and θ, because it is easier to formulate the reconciliation in terms of tori than in terms of pseudo-orbits. Equation (4.66) is also known as the **objective function**, and is the continuous-time formulation of the equation that will be minimised in order to determine the reconciled QFMin-ghost tori in terms of $\theta = \vartheta(t|\Theta_0) = \vartheta(\Theta, t)|_{\Theta=\Theta_0+\iota t}$.

Chapter 5

Construction of Almost-Invariant Tori for Discrete-Time Systems

This chapter begins the discretisation of almost-invariant tori that will allow the reconciliation between almost-invariant tori to be implemented numerically, although the emphasis is on unreconciled almost-invariant tori rather than reconciled ones. It introduces the concept of a generating function that is the discrete-time equivalent of the Lagrangian and Hamiltonian, before defining the dynamics associated with discrete-time systems and listing the various symmetries of the generating function that will be needed to complete the reconciliation and prevent it from being underdetermined. Two different classes of almost-invariant curves are defined, corresponding to the momentum both before and after the kick in the kicked rotor, and a discrete-time definition of QFMin, AGMin and ghost tori is provided. Finally, the QFMin equation is derived using two different methods, and the discrete-time QFMin and AGMin tori are shown to belong to the same class of discrete-time almost-invariant tori.

5.1 Lagrangian Generating Functions

Having defined the conditions for consistency of the continuous-time QFMin and ghost tori, we now turn our attention to analysing the discrete-time system, which is much more amenable to computational programming than the continuous-time system, and will be used in Chapters 7 and 8 to demonstrate numerically that QFMin and ghost tori can be reconciled with each other. In discrete-time dynamical systems, the Lagrangian and Hamiltonian are replaced by **generating functions**, which, in the case of the standard map, can be derived from the Lagrangian and Hamiltonian of the kicked rotor. The

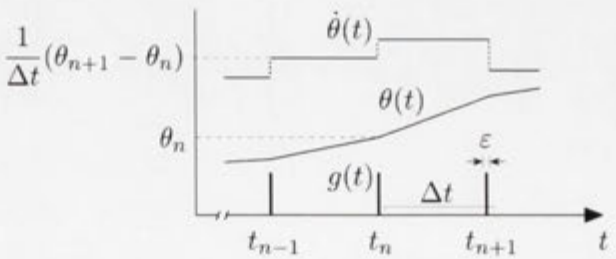

Figure 5.1: Plot of the Lagrangian trial functions $\theta(t)$ and $\dot{\theta}(t)$ along with the acceleration due to gravity $g(t)$. Source: Modified version of a diagram appearing in Dewar [21].

Lagrangian of the kicked rotor is given by [21,22]

$$L(\theta, \dot{\theta}, t) = \frac{1}{2} m l^2 \dot{\theta}^2 - mg(t) l (1 - \cos\theta), \tag{5.1}$$

where l is the length of the pendulum, m is the mass at the end of it, and $g(t)$ is the accelaration due to gravity. In the kicked rotor, an explicit formula for $g(t)$ is given by

$$g(t) = g_0 \Delta t \sum_{n=-\infty}^{\infty} \delta(t - t_n), \tag{5.2}$$

where g_0 is the average value of $g(t)$ and Δt is the periodicity (see Figure 5.1). The t_n satisfy the relationship $t_n = n\Delta t$, where $-N \leq n \leq N$, $N \in \mathbb{Z}^+$ (the set of positive integers) and $n \in \mathbb{Z}$ [21]. In order to highlight the essential features of the calculation, we set $m = l = g_0 = 1$, so the Lagrangian becomes

$$L(\theta, \dot{\theta}, t) = \frac{1}{2} \dot{\theta}^2 - \Delta t \sum_{n=-\infty}^{\infty} \delta(t - t_n)(1 - \cos\theta). \tag{5.3}$$

Because the motion is uniform between the kicks, it is possible to represent θ as a continuous, piecewise-linear trial function [21]

$$\theta(t) = \frac{1}{\Delta t}[(t_{n+1} - t)\theta_n + (t - t_n)\theta_{n+1}], \quad t_n \leq t \leq t_{n+1}, \tag{5.4}$$

along with its derivative

$$\dot{\theta}(t) = \frac{1}{\Delta t}(\theta_{n+1} - \theta_n), \quad t_n \leq t \leq t_{n+1}. \tag{5.5}$$

The Lagrangian trial functions are plotted in Figure 5.1. Assuming that $\theta(t)$ and $\theta'(t)$ can be written in this form, we calculate the action by integrating $L(\theta, \dot{\theta}, t)$ from $t_{-N} + \varepsilon$ to $t_N + \varepsilon$ with respect to t and taking the limit as $\varepsilon \to 0$ [21]. Then the kinetic energy becomes

$$\begin{aligned} \lim_{\varepsilon \to 0} \int_{t_{-N}+\varepsilon}^{t_N+\varepsilon} \frac{1}{2} \dot{\theta}^2 \, \mathrm{d}t &= \lim_{\varepsilon \to 0} \sum_{n=-N}^{N-1} \int_{t_{n-1}+\varepsilon}^{t_n+\varepsilon} \frac{1}{2} \left(\frac{\theta_{n+1} - \theta_n}{\Delta t} \right)^2 \mathrm{d}t \\ &= \sum_{n=-N}^{N-1} \frac{1}{2} \frac{(\theta_{n+1} - \theta_n)^2}{\Delta t} \end{aligned} \tag{5.6}$$

and the potential energy becomes

$$\begin{aligned} &\lim_{\varepsilon \to 0} \int_{t_{-N}+\varepsilon}^{t_N+\varepsilon} \sum_{n=-\infty}^{\infty} \delta(t - t_n)\,(1 - \cos\theta)\,\mathrm{d}t \\ &= \sum_{n=-N+1}^{N} \int_{-\infty}^{\infty} \delta(t - t_n) \left(1 - \cos\left\{ \frac{1}{\Delta t}[(t_{n+1} - t)\theta_n + (t - t_n)\theta_{n+1}] \right\} \right) \mathrm{d}t \\ &= \sum_{n=-N}^{N-1} (1 - \cos\theta_{n+1})\,, \end{aligned} \tag{5.7}$$

which imply that the action is given by

$$\begin{aligned} S &= \lim_{\varepsilon \to 0} \int_{t_{-N}+\varepsilon}^{t_N+\varepsilon} L(\theta, \dot{\theta}, t)\, \mathrm{d}t \\ &= \sum_{n=-N}^{N-1} \left[\frac{1}{2} \frac{(\theta_{n+1} - \theta_n)^2}{\Delta t} - \Delta t (1 - \cos \theta_{n+1}) \right]. \end{aligned} \tag{5.8}$$

Hence, we can define the Lagrangian generating function as [25,31]

$$F\left(\theta, \bar{\theta}\right) = \frac{1}{2} \frac{\left(\theta - \bar{\theta}\right)^2}{\Delta t} - \Delta t (1 - \cos \theta), \tag{5.9}$$

where θ and $\bar{\theta}$ are dummy variables and Δt is the periodicity of θ. In the language of Goldstein [18], this is a Type 1 generating function. Multiplying through by Δt and using an arbitrary potential, it can be seen that we can define the Lagrangian generating function much more simply as

$$F\left(\theta, \bar{\theta}\right) = \frac{1}{2} \left(\theta - \bar{\theta}\right)^2 - V(\theta), \tag{5.10}$$

which agrees with Equation (27) of Dewar and Khorev [25]. Note that in the case of the standard map,

$$V(\theta) = -k \cos \theta, \tag{5.11}$$

so the Lagrangian generating function becomes [25]

$$F\left(\theta, \bar{\theta}\right) = \frac{1}{2} \left(\theta - \bar{\theta}\right)^2 + k \cos \theta. \tag{5.12}$$

5.2 Hamiltonian Generating Functions

Similarly, the Hamiltonian of the kicked rotor is given by [21,22]

$$H(I, \theta, t) = \frac{I^2}{2ml^2} + mg(t)l(1 - \cos \theta), \tag{5.13}$$

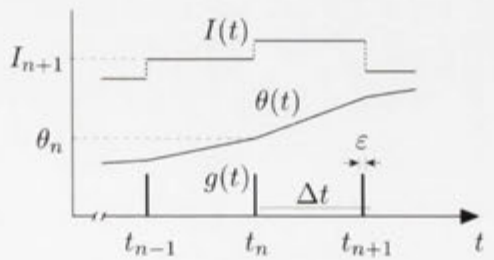

Figure 5.2: Plot of the Hamiltonian trial functions $I(t)$ and $\theta(t)$ along with the acceleration due to gravity $g(t)$. Source: Modified version of a diagram appearing in Dewar [21].

where the acceleration due to gravity is given by

$$g(t) = g_0 \Delta t \sum_{n=-\infty}^{\infty} \delta(t - t_n), \tag{5.14}$$

g_0 is the average value of $g(t)$ and Δt is the periodicity (see Figure 5.2). The t_n satisfy $t_n = n\Delta t$, where $-N \leq n \leq N$, $N \in \mathbb{Z}^+$ and $n \in \mathbb{Z}$ [22]. Setting $l = m = g_0 = 1$, this reduces to just

$$H(I, \theta, t) = \frac{1}{2} I^2 + \Delta t \sum_{n=-\infty}^{\infty} \delta(t - t_n)(1 - \cos\theta). \tag{5.15}$$

Writing θ as a continuous, piecewise linear trial function [21]

$$\theta(t) = \frac{1}{\Delta t}[(t_{n+1} - t)\theta_n + (t - t_n)\theta_{n+1}], \quad t_n \leq t \leq t_{n+1}, \tag{5.16}$$

it can be seen that I, the Hamiltonian analogue of $\dot{\theta}$, can be written as a piecewise constant step function [21]

$$I(t) = I_{n+1}, \quad t_n \leq t \leq t_{n+1}. \tag{5.17}$$

The Hamiltonian trial functions are plotted in Figure 5.2. Carrying out the same integration procedure over $H(I, \theta, t)$ as was performed over $L(\theta, \dot{\theta}, t)$ to calculate the action in the Lagrangian case, it can be seen that the kinetic energy is given by

$$\begin{aligned} \lim_{\varepsilon \to 0} \int_{t_{-N}+\varepsilon}^{t_N+\varepsilon} \frac{1}{2} I^2 \, \mathrm{d}t &= \lim_{\varepsilon \to 0} \sum_{n=-N}^{N-1} \int_{t_{n-1}+\varepsilon}^{t_n+\varepsilon} \frac{1}{2} I_{n+1}^2 \, \mathrm{d}t \\ &= \sum_{n=-N}^{N-1} \frac{1}{2} I_{n+1}^2 \Delta t \end{aligned} \tag{5.18}$$

and the transformation term between Lagrangian and Hamiltonian systems is given by

$$\begin{aligned} \lim_{\varepsilon \to 0} \int_{t_{-N}+\varepsilon}^{t_N+\varepsilon} I\dot{\theta} \, \mathrm{d}t &= \lim_{\varepsilon \to 0} \sum_{n=-N}^{N-1} \int_{t_{n-1}+\varepsilon}^{t_n+\varepsilon} I_{n+1} \left(\frac{\theta_{n+1} - \theta_n}{\Delta t} \right) \mathrm{d}t \\ &= \sum_{n=-N}^{N-1} I_{n+1} \left(\theta_{n+1} - \theta_n \right). \end{aligned} \tag{5.19}$$

Combining these with Equation (5.7), it follows that the action of the Hamiltonian system is given by [21]

$$\begin{aligned} S &= \lim_{\varepsilon \to 0} \int_{t_{-N}+\varepsilon}^{t_N+\varepsilon} \left[I\dot{\theta} - H(I, \theta, t) \right] \mathrm{d}t \\ &= \sum_{n=-N}^{N-1} \left[I_{n+1}(\theta_{n+1} - \theta_n) - \frac{1}{2} I_{n+1}^2 \Delta t - \Delta t(1 - \cos\theta_{n+1}) \right]. \end{aligned} \tag{5.20}$$

In order to write the action purely in terms of Hamiltonian coordinates, we eliminate θ_{n+1} by making the substitution $\theta_{n+1} - \theta_n = I_{n+1}\Delta t$. Then the action takes the form

$$S = \sum_{n=-N}^{N-1} \left[\frac{1}{2} I_{n+1}^2 \Delta t - \Delta t(1 - \cos\theta_{n+1}) \right], \tag{5.21}$$

which leads to the Hamiltonian generating function [25,31]

$$F(\theta, I) = \frac{1}{2} I^2 \Delta t - \Delta t(1 - \cos\theta), \tag{5.22}$$

where θ and I are dummy variables. In the language of Goldstein [18], this is a Type 2 generating function. Dividing through by Δt and replacing $(1 - \cos\theta)$ with an arbitrary potential, it follows that the most general form of the Hamiltonian generating function is given by

$$F(\theta, I) = \frac{1}{2} I^2 - V'(\theta), \tag{5.23}$$

which is analogous to the Lagrangian generating function. From now on, we will restrict our attention to Lagrangian generating functions almost entirely, but we will refer back to these results in Section 5.5, where we derive the standard map from the kicked rotor Hamiltonian.

5.3 The Discrete-Time Action and Action Gradient

The **action** of the kicked rotor is given by

$$S = \lim_{\varepsilon \to 0} \int_{t_{-N}+\varepsilon}^{t_N+\varepsilon} L(\theta, \dot{\theta}, t)\, \mathrm{d}t, \tag{5.24}$$

which, as we have already seen, can be written as the sum of generating functions [25,31]

$$S = \sum_{n=0}^{q-1} F(\theta_n, \theta_{n+1}), \tag{5.25}$$

where the θ_n satisfy the periodicity condition $\theta_{n+q} = \theta_n + 2\pi p$ for rational rotational transforms $\iota = p/q$ with $p, q \in \mathbb{Z}$ being mutually prime. Assuming that the generating function also satisfies the **twist condition** [25]

$$\frac{\partial^2 F}{\partial\theta\partial\bar{\theta}} < 0 \quad \forall\theta, \bar{\theta} \in \mathbb{R}, \tag{5.26}$$

we can define two different momenta for each θ_n, given by [25,31]

$$I_n^+ = F_2(\theta_{n-1}, \theta_n), \tag{5.27}$$

$$I_n^- = -F_1(\theta_n, \theta_{n+1}), \tag{5.28}$$

where F_i denotes the partial derivative of F with respect to its ith variable. Physically, these represent the momenta of the kicked rotor on either side of the kick at t_n, with I_n^- representing the momentum before the kick, and I_n^+ representing the momentum after the

kick. The difference between I_n^+ and I_n^- is given by [25,31]

$$\begin{aligned}\Delta I_n &= I_n^+ - I_n^- \\ &= F_2(\theta_{n-1}, \theta_n) + F_1(\theta_n, \theta_{n+1}),\end{aligned} \tag{5.29}$$

and it can be seen from Equation (5.25) that [25]

$$\Delta I_n = \frac{\partial S}{\partial \theta_n}. \tag{5.30}$$

Hence, ΔI_n will often be used as shorthand for the discrete-time action gradient $\partial S/\partial \theta_n$.

In analogy with continuous-time systems, we can define a **path** within a discrete-time Lagrangian system as a parametric curve that lies within the covering space $\mathbb{R} \times \mathbb{Z}$. If $\epsilon = p/q$, where p and q are integers that we have restricted to being mutually prime, then the path is said to be (p, q)-periodic, and satisfies the periodicity condition [25,31]

$$\theta_{n+q} = \theta_n + 2\pi p \tag{5.31}$$

for all $n \in \mathbb{Z}$. Discrete-time (p, q)-periodic paths have only q distinct coordinates $\{\theta_0, \ldots, \theta_{q-1}\}$, as opposed to the infinite number of coordinates that non-periodic discrete-time paths have [25]. When a discrete-time (p, q)-periodic path satisfies $\Delta I_n = 0$ for all n, it is called a **discrete-time (p, q)-periodic orbit**, and has the Euler-Lagrange equation [32]

$$F_2(\theta_{n-1}, \theta_n) + F_1(\theta_n, \theta_{n+1}) = 0. \tag{5.32}$$

However, if a discrete-time (p, q)-periodic path does not satisfy $\Delta I_n = 0$ for all n, but $\Delta I_n \approx 0$ is of order ε, then it is called a **discrete-time (p, q)-periodic pseudo-orbit**.

5.4 Symmetries of the Lagrangian Generating Function

The generating function $F(\theta, \bar{\theta})$ can have up to two main symmetries, which will be used in Chapter 7 to optimise and simplify the numerical computation. Suppose that $P(\Theta)$, $Q(\Theta)$ and $R(\Theta)$ are arbitrary functions, and that $F(\theta, \bar{\theta})$ is invariant under the transformation

$$F(\theta, \bar{\theta}) = F(\bar{\theta}, \theta) + Q(\theta) - Q(\bar{\theta}). \tag{5.33}$$

Then $F(\theta, \bar{\theta})$ is said to have **time-reversal symmetry** [33]. Similarly, if $(\theta, \bar{\theta})$ is invariant under the transformation

$$F(\theta, \bar{\theta}) = F(-\theta, -\bar{\theta}) + P(\theta) - P(\bar{\theta}), \tag{5.34}$$

where $P(\theta)$ is an odd function, then it is said to have **parity-reversal symmetry** [33]. These two symmetries are often called $\mathbb{T}$-symmetry and $\mathbb{P}$-symmetry, respectively, although the notation does tend to vary between authors [33]. When $F(\theta, \bar{\theta})$ has both $\mathbb{P}$-symmetry and $\mathbb{T}$-symmetry, it is said to have $\mathbb{PT}$-symmetry, and satisfies the relationship

$$F(\theta, \bar{\theta}) = F(-\bar{\theta}, -\theta) + R(\theta) - R(\bar{\theta}), \tag{5.35}$$

where $R(\theta) = Q(\theta) - P(\theta)$ is an even function, in addition to the previous two [33]. These symmetries are so-named because of the effects they have on the action, with $\mathbb{T}$-symmetry

implying that

$$S = \sum_{n=0}^{q-1} F(\theta_n, \theta_{n+1}) \doteq \sum_{n=1}^{q} F(\theta_n, \theta_{n-1}) \tag{5.36}$$

and $\mathbb{P}$-symmetry implying that

$$S = \sum_{n=0}^{q-1} F(\theta_n, \theta_{n+1}) \doteq \sum_{n=0}^{q-1} F(-\theta_n, -\theta_{n+1}), \tag{5.37}$$

where $\doteq$ denotes equality up to a constant plus terms depending only on the endpoints θ_0 and θ_n [33]. Combining these equations, it can be seen that $\mathbb{PT}$-symmetry implies that

$$S = \sum_{n=0}^{q-1} F(\theta_n, \theta_{n+1}) \doteq \sum_{n=1}^{q} F(-\theta_n, -\theta_{n-1}). \tag{5.38}$$

5.5 Derivation of the Standard Map from the Kicked Rotor

Returning to Equation (5.20), we use it to demonstrate the deep connection between the kicked rotor and the standard map by using the former to derive the latter. We start by differentiating Equation (5.20) with respect to I_{n+1} and θ_n for a specific n, which leads to the equations [21]

$$\frac{\partial S}{\partial I_{n+1}} = \theta_{n+1} - \theta_n - I_{n+1}\Delta t, \tag{5.39}$$

$$\frac{\partial S}{\partial \theta_n} = I_n - I_{n+1} - \Delta t \sin\theta_{n+1}. \tag{5.40}$$

Since these are just the gradients of the action, they will be zero when the action is a minimum. Hence, the action of the kicked rotor is minimised whenever [21, 22]

$$\theta_{n+1} - \theta_n - I_{n+1}\Delta t = 0, \tag{5.41}$$

$$I_n - I_{n+1} - \Delta t \sin\theta_{n+1} = 0. \tag{5.42}$$

Substituting in [21]

$$\theta_n = 2\pi x_n, \tag{5.43}$$

$$I_n = \frac{2\pi}{\Delta t} y_n, \tag{5.44}$$

and setting $k = (\Delta t)^2$, we find that [21, 22]

$$x_{n+1} = x_n + y_{n+1}, \tag{5.45}$$

$$y_{n+1} = y_n - \frac{k}{2\pi} \sin 2\pi x_n, \tag{5.46}$$

which is the definition of the standard map. Hence, the standard map captures the dynamics of the points at which the kicked rotor has stationary action.

5.6 Discrete-Time Almost-Invariant Curves

Suppose that $\theta_n = \theta_n(\theta_0)$ defines a one-parameter family of (p, q)-periodic pseudo-orbits, where n is an integer between 0 and $q-1$, θ_0 is the value of θ_n at $n = 0$, and $0 \leq \theta_0 < 2\pi/q$. Then the points $(\theta_n(\theta_0), I_n^{\pm}(\theta_0))$ are the loci of two different families of almost-invariant curves [25,31], defined by

$$C^{\pm} = \bigcup_{n=0}^{q-1} C_n^{\pm}, \tag{5.47}$$

where

$$C_n^{\pm} = \{(\theta_n(\theta_0), I_n^{\pm}(\theta_0))\}. \tag{5.48}$$

These families exist independently of the QFMin-AGMin-ghost-curve classification, meaning that there are two different kinds of QFMin curve, two different kinds of AGMin curve, and two different kinds of ghost curve, each of which is denoted by either C^+ or C^-. Because the C^+ curve is defined in terms of Equation (5.27) and the C^- curve is defined in terms of Equation (5.28), the C^+ and C^- curves can only be equal in the case of the standard map when $k = 0$. The term ΔI_n gives the vertical distance between the C^+ and C^- curves when plotted in (θ, I)-space, and unless $k = 0$, $\Delta I_n = 0$ if and only if there is an action-minimax or action-minimising orbit for that particular value of θ_n. Setting $T : (\theta_n, I_n^-) \mapsto (\theta_{n+1}, I_{n+1}^+)$, where I_n^+ and I_n^- are defined by Equations (5.27) and (5.28), it can be seen that the C^+ curves are the forward images of the C^- curves under the area-preserving twist map T [25]. Similarly, the C^- curves are the backward images of the C^+ curves.

5.7 Discrete-Time Almost-Invariant Tori

QFMin, AGMin and ghost tori can be defined for discrete-time Hamiltonian systems, just as they are for their continuous-time analogues. For example, the discrete-time version of a QFMin torus is given by the minimisation of the **discrete-time quadratic flux functional** [25]

$$\varphi_2[\Gamma] = \frac{1}{2} \sum_{n=0}^{q-1} \int_0^{2\pi/q} (\Delta I_n)^2 \, \mathrm{d}\theta_n \tag{5.49}$$

over an arbitrary toroidal surface Γ, whereas the discrete-time analogue of an AGMin torus is given by the minimisation of the modified **discrete-time action gradient functional**

$$f[\theta, \mu] = \sum_{n=0}^{q-1} \left[\frac{1}{2} (\Delta I_n)^2 - \mu \theta_n \right] \tag{5.50}$$

over an arbitrary discrete-time (p, q)-periodic path $\theta = \{\theta_0, \ldots, \theta_{q-1}\}$. Similarly, the discrete-time version of a ghost torus consists of all the points that lie on the paths of steepest descent of the **discrete-time action gradient flow equation** [25]

$$\theta_n'(\tau) = -\Delta I_n, \tag{5.51}$$

between an action-minimax and action-minimising orbit, where τ is a continuous, timelike parameter that labels the pseudo-orbits. In order to see that the definitions of discrete-time almost-invariant tori are equivalent to those of their continuous-time counterparts,

we note that ΔI_n is equivalent to $\partial S/\partial\theta_n$, where $n = t_n/2\pi$, and that we can change the boundaries of integration in the continuous-time quadratic flux functional in such a way that the shape of the QFMin tori remains unchanged. This gives

$$\int_0^{2\pi}\int_0^{2\pi}\left(\frac{\delta S}{\delta\theta}\right)^2 \mathrm{d}\theta\,\mathrm{d}t = \int_0^{2\pi q}\int_0^{2\pi/q}\left(\frac{\delta S}{\delta\theta}\right)^2 \mathrm{d}\theta\,\mathrm{d}t, \tag{5.52}$$

which explains why Equation (5.49) is the discrete-time analogue of Equation (3.13).

5.8 Original Lagrangian Formulation of Discrete-Time QFMin Tori

In addition to the discrete-time version of the quadratic flux functional, there is also a discrete-time version of the QFMin equation, which is the Euler-Lagrange equation of the discrete-time quadratic flux

$$\varphi_2[\Gamma] = \frac{1}{2}\sum_{n=0}^{q-1}\int_0^{2\pi/q}(\Delta I_n)^2\,\mathrm{d}\theta_n. \tag{5.53}$$

The discrete-time QFMin equation can be derived by the Lagrangian method by setting $\mathrm{d}\theta_n = \theta_n'(\theta_0)\,\mathrm{d}\theta_0$, taking the first variation of the quadratic flux and using integration by parts. Then

$$\delta\varphi_2[\Gamma] = \sum_{n=0}^{q-1}\int_0^{2\pi/q}\Delta I_n\left[\theta_n'(\theta_0)\,\delta(\Delta I_n) - \Delta I_n'(\theta_0)\,\delta\theta_n\right]\mathrm{d}\theta_0. \tag{5.54}$$

Recalling that

$$\Delta I_n = F_2(\theta_{n-1},\theta_n) + F_1(\theta_n,\theta_{n+1}), \tag{5.55}$$

we make the substitutions

$$\begin{aligned}\delta(\Delta I_n) = {} & F_{12}(\theta_{n-1},\theta_n)\,\delta\theta_{n-1} + F_{22}(\theta_{n-1},\theta_n)\,\delta\theta_n \\ & + F_{11}(\theta_n,\theta_{n+1})\,\delta\theta_n + F_{12}(\theta_n,\theta_{n+1})\,\delta\theta_{n+1}\end{aligned} \tag{5.56}$$

and

$$\begin{aligned}\Delta I_n'(\theta_0) = {} & F_{12}(\theta_{n-1},\theta_n)\theta_{n-1}'(\theta_0) + F_{22}(\theta_{n-1},\theta_n)\theta_n'(\theta_0) \\ & + F_{11}(\theta_n,\theta_{n+1})\theta_n'(\theta_0) + F_{12}(\theta_n,\theta_{n+1})\theta_{n+1}'(\theta_0).\end{aligned} \tag{5.57}$$

This leads to the equation

$$\begin{aligned}\delta\varphi_2[\Gamma] = \sum_{n=0}^{q-1}\int_0^{2\pi/q}\Delta I_n\big[&\theta_n'(\theta_0)F_{12}(\theta_{n-1},\theta_n)\,\delta\theta_{n-1} + \theta_n'(\theta_0)F_{12}(\theta_n,\theta_{n+1})\,\delta\theta_{n+1} \\ &-\theta_{n-1}'(\theta_0)F_{12}(\theta_{n-1},\theta_n)\,\delta\theta_n - \theta_{n+1}'(\theta_0)F_{12}(\theta_n,\theta_{n+1})\,\delta\theta_n\big]\,\mathrm{d}\theta_0.\end{aligned} \tag{5.58}$$

Setting $n \mapsto n+1$ in the first term inside the integrand and $n \to n-1$ in the second term, and using the fact that $\theta_{n+q} = \theta_n + 2\pi p$, it follows that [25]

$$\begin{aligned}\delta\varphi_2[\Gamma] = \sum_{n=0}^{q-1} \int_0^{2\pi/q} &\left[\theta'_{n+1}(\theta_0) F_{12}(\theta_n, \theta_{n+1})(\Delta I_{n+1} - \Delta I_n)\right. \\ &\left. -\theta'_{n-1}(\theta_0) F_{12}(\theta_{n-1}, \theta_n)(\Delta I_n - \Delta I_{n-1})\right] \delta\theta_n \, \mathrm{d}\theta_0.\end{aligned} \tag{5.59}$$

Hence, the Euler-Lagrange equations have the form [25]

$$\theta'_{n+1} f_{n+1} = \theta'_{n-1} f_n, \tag{5.60}$$

where

$$f_n = F_{12}(\theta_{n-1}, \theta_n)(\Delta I_n - \Delta I_{n-1}). \tag{5.61}$$

In order to determine ΔI_n as a function of ΔI_0, we rewrite Equation (5.61) as

$$\Delta I_n = \Delta I_{n-1} + \frac{f_n}{F_{12}(\theta_{n-1}, \theta_n)}, \tag{5.62}$$

where we have assumed that $F_{12}(\theta_{n-1}, \theta_n) \neq 0$, and evaluate it recursively, which yields

$$\Delta I_n = \Delta I_0 + \sum_{r=1}^{n} \frac{f_r}{F_{12}(\theta_{r-1}, \theta_r)}. \tag{5.63}$$

Similarly, evaluating Equation (5.60) recursively to find f_r in terms of f_1, we get

$$f_r = \frac{c}{\theta'_r \theta'_{r-1}}, \tag{5.64}$$

where $c = \theta'_0 \theta'_1 f_1$ is constant and we have assumed that $\theta'_2, \ldots, \theta'_r \neq 0$. This can be substituted into Equation (5.63) to give

$$\Delta I_n = \Delta I_0 + c \sum_{r=1}^{n} \frac{1}{\theta'_{r-1} \theta'_r F_{12}(\theta_{r-1}, \theta_r)}, \tag{5.65}$$

which differs slightly from Equation (17) of Dewar and Khorev [25] and Equation (3.57) of Khorev [34] in that the summation index is taken from 1 to n instead of from 0 to n. Because discrete-time (p, q)-periodic pseudo-orbits have only q distinct coordinates, we suspect that these previous calculations are in error, because they assume the existence of $q+1$ distinct coordinates. Returning to the calculation of the Euler-Lagrange equation for discrete-time QFMin tori, we note that because the individual pseudo-orbits θ_n are (p, q)-periodic, it is impossible for Equation (5.65) to hold unless $c = 0$. This implies that $\Delta I_n = \Delta I_0$, and because ΔI_0 depends on θ_0 but not n, we set $\Delta I_0 = \nu(\theta_0)$ to yield the discrete-time QFMin equation

$$\Delta I_n = \nu(\theta_0). \tag{5.66}$$

Because we have already seen that ΔI_n and $\partial S / \partial \theta_n$ are equivalent to each other, it is easy to see that the discrete-time definition of a QFMin torus is equivalent to the continuous-time definition. Note that in the case of the generalised standard map, which has arbitrary

potential, the generating function is given by

$$F(\theta, \bar{\theta}) = \frac{1}{2}(\theta - \bar{\theta})^2 - V(\theta), \tag{5.67}$$

and when this is combined with Equations (5.29) and (5.66), the QFMin equation becomes

$$\theta_{n+1} - 2\theta_n + \theta_{n-1} + V'(\theta_n) + \nu(\theta_0) = 0. \tag{5.68}$$

5.9 Alternative Lagrangian Formulation of Discrete-Time QFMin Tori

The discrete-time QFMin equation can also be derived by taking the continuous-time QFMin equation (Equation (3.27)) and substituting the action gradient of the generalised kicked rotor with semi-arbitrary potential into it. The continuous-time QFMin equation is given by

$$\frac{\delta S}{\delta \theta} \equiv L_\theta - \frac{\mathrm{d}}{\mathrm{d}t} L_{\dot{\theta}} = \nu, \tag{5.69}$$

where the dependence of ν on θ_0 has been omitted for simplicity. Assuming that L is of the form corresponding to the generalised kicked rotor

$$L = \frac{1}{2}\dot{\theta}^2 - \sum_{n=0}^{q-1} \delta(t - t_n) V(\theta), \tag{5.70}$$

it follows from Equation (5.69) that

$$\ddot{\theta} = -\nu - \sum_{n=0}^{q-1} \delta(t - t_n) V'(\theta), \tag{5.71}$$

so $\ddot{\theta} = -\nu$ between the nodes. This means that the **trial function** for θ must be a quadratic of the form $\theta(t) = at^2 + bt + c$, and have quadratic coefficient $a = -\frac{1}{2}\nu$. The other two coefficients can be determined from the boundary conditions $\theta(t_n) = \theta_n$ and $\theta(t_{n+1}) = \theta_{n+1}$, which can be substituted into the trial function and solved simultaneously to give

$$b = \frac{1}{\Delta t}\left[\theta_{n+1} - \theta_n + \frac{1}{2}\nu\left(t_{n+1}^2 - t_n^2\right)\right], \tag{5.72}$$

$$c = \frac{1}{\Delta t}\left[t_{n+1}\left(\theta_n + \frac{1}{2}\nu t_n^2\right) - t_n\left(\theta_{n+1} + \frac{1}{2}\nu t_{n+1}^2\right)\right]. \tag{5.73}$$

Substituting these into $\theta(t) = -\frac{1}{2}\nu t^2 + bt + c$ yields

$$\theta(t) = -\frac{1}{2}\nu t^2 + \frac{1}{\Delta t}\left[(t_{n+1} - t)\left(\theta_n + \frac{1}{2}\nu t_n^2\right) + (t - t_n)\left(\theta_{n+1} + \frac{1}{2}\nu t_{n+1}^2\right)\right], \quad t_n \le t \le t_{n+1}, \tag{5.74}$$

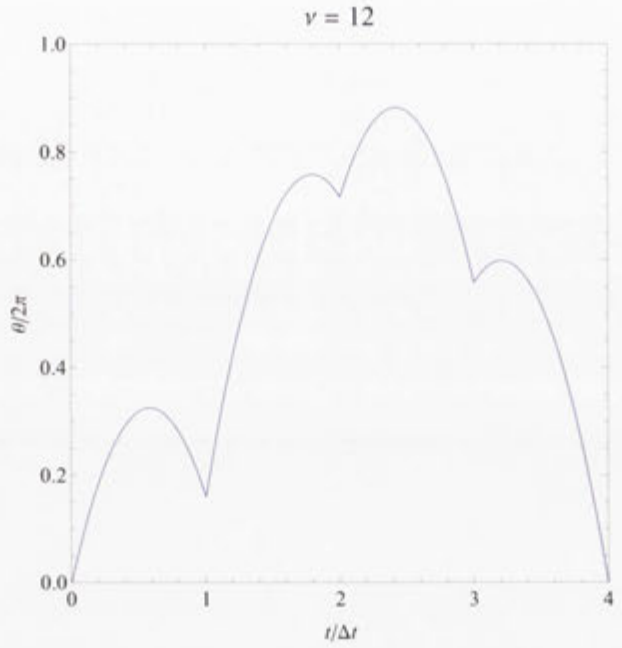

Figure 5.3: Schematic diagram of the quadratic trial function $\theta(t)$ for $\nu = 12$.

which can also be written as

$$\theta(t) = \sum_{n=0}^{q-1} \left\{ -\frac{1}{2}\nu t^2 + \frac{1}{\Delta t}\left[(t_{n+1} - t)\left(\theta_n + \frac{1}{2}\nu t_n^2\right) + (t - t_n)\left(\theta_{n+1} + \frac{1}{2}\nu t_{n+1}^2\right)\right]\right\} \times [U(t - t_n) - U(t - t_{n+1})], \quad t_0 \le t \le t_q, \tag{5.75}$$

where $U(t-t_n)$ is the Heaviside step function (or unit step function). A schematic diagram of the quadratic trial function is shown in Figure 5.3. Using the definitions

$$R(t - t_n) = (t - t_n)U(t - t_n), \tag{5.76}$$

$$P(t - t_n) = \frac{1}{2}(t - t_n)^2 U(t - t_n), \tag{5.77}$$

it can be shown that

$$\theta(t) = \sum_{n=0}^{q-1} \left\{ -\nu\left[P(t - t_n) - P(t - t_{n+1})\right] + \frac{\theta_{n+1} - \theta_n}{\Delta t}\left[R(t - t_n) - R(t - t_{n+1})\right] + \frac{1}{2}\nu\Delta t\left[R(t - t_n) + R(t - t_{n+1})\right] + \theta_n U(t - t_n) - \theta_{n+1} U(t - t_{n+1})\right\}. \tag{5.78}$$

Taking the derivative of Equation (5.78) with respect to t, it follows that

$$\dot{\theta}(t) = \sum_{n=0}^{q-1} \left\{ -\nu\left[R(t - t_n) - R(t - t_{n+1})\right] + \frac{\theta_{n+1} - \theta_n}{\Delta t}\left[U(t - t_n) - U(t - t_{n+1})\right] + \frac{1}{2}\nu\Delta t\left[U(t - t_n) + U(t - t_{n+1})\right]\right\}, \tag{5.79}$$

because $P'(t) = R(t)$, $R'(t) = U(t)$, $U'(t) = \delta(t)$, and $\sum_{n=0}^{q-1} \theta_n \delta(t - t_n) = \sum_{n=0}^{q-1} \theta_{n+1} \delta(t - t_{n+1})$. It also follows that the second derivative of Equation (5.78) with respect to t is given by

$$\ddot{\theta}(t) = \sum_{n=0}^{q-1} \left\{ -\nu \left[U(t - t_n) - U(t - t_{n+1}) \right] + \frac{\theta_{n+1} - \theta_n}{\Delta t} \left[\delta(t - t_n) - \delta(t - t_{n+1}) \right] + \frac{1}{2} \nu \Delta t \left[\delta(t - t_n) + \delta(t - t_{n+1}) \right] \right\}. \tag{5.80}$$

Noting that some of the expressions in Equation (5.80) can be simplified to

$$\sum_{n=0}^{q-1} -\nu [U(t - t_n) - U(t - t_{n+1})] = -\nu, \tag{5.81}$$

$$\sum_{n=0}^{q-1} \frac{\theta_{n+1} - \theta_n}{\Delta t} \left[\delta(t - t_n) - \delta(t - t_{n+1}) \right] = \sum_{n=0}^{q-1} \frac{\theta_{n+1} - 2\theta_n + \theta_{n-1}}{\Delta t} \delta(t - t_n), \tag{5.82}$$

$$\sum_{n=0}^{q-1} \left[\frac{1}{2} \nu \Delta t \delta(t - t_n) + \frac{1}{2} \nu \Delta t \delta(t - t_{n+1}) \right] = \sum_{n=0}^{q-1} \nu \Delta t \delta(t - t_n), \tag{5.83}$$

it can be seen that

$$\ddot{\theta}(t) = -\nu + \sum_{n=0}^{q-1} \left[\frac{1}{\Delta t} (\theta_{n+1} - 2\theta_n + \theta_{n-1}) + \nu \Delta t \right] \delta(t - t_n). \tag{5.84}$$

Substituting this into Equation (5.71) gives

$$\sum_{n=0}^{q-1} \left[\frac{1}{\Delta t} (\theta_{n+1} - 2\theta_n + \theta_{n-1}) + \nu \Delta t \right] \delta(t - t_n) = -\sum_{n=0}^{q-1} \delta(t - t_n) V'(\theta_n), \tag{5.85}$$

so the nodes obey the difference equation

$$\theta_{n+1} - 2\theta_n + \theta_{n-1} + V'(\theta_n) \Delta t + \nu (\Delta t)^2 = 0. \tag{5.86}$$

It is easy to see that the support of Equation (5.85) is zero between the nodes, and that Equation (5.86) is equivalent to Equation (5.68) whenever $\Delta t = 1$. However, we will continue to assume that Δt is arbitrary for the time being.

5.10 Generalised Discrete-Time AGMin Pseudo-Orbits and Tori

Generalised continuous-time AGMin pseudo-orbits can also be discretised, and shown to encompass both discrete-time QFMin pseudo-orbits and discrete-time AGMin pseudo-orbits, and by extension, generalised continuous-time AGMin tori can also be discretised, and shown to encompass both discrete-time QFMin tori and discrete-time AGMin tori. All these facts are shown by demonstrating the relationship between discrete-time QFMin pseudo-orbits and discrete-time AGMin pseudo-orbits, in a manner similar to that described in Section 3.7. First, we take the average of both sides of Equation (5.66) over one

full (p, q)-periodic pseudo-orbit with respect to n, and show that

$$\nu(\theta_0) = \frac{1}{q} \sum_{n=0}^{q-1} \Delta I_n. \tag{5.87}$$

Then, we formulate a variational principle for discrete-time QFMin pseudo-orbits by subtracting off the fluctuating part of ΔI_n, which gives

$$\mathcal{V}[\theta] = \frac{1}{2} \sum_{n=0}^{q-1} \left(\Delta I_n - \frac{1}{q} \sum_{n=0}^{q-1} \Delta I_n \right)^2, \tag{5.88}$$

where $\theta = \{\theta_0, \ldots, \theta_{q-1}\}$ is a (p, q)-periodic pseudo-orbit. Clearly, $\mathcal{V}[\theta] \geq 0$ with equality if and only if

$$\Delta I_n - \frac{1}{q} \sum_{n=0}^{q-1} \Delta I_n = 0. \tag{5.89}$$

That is, $\mathcal{V}[\theta]$ is minimised (to zero) by discrete-time QFMin pseudo-orbits. Next, we invoke the computational formula for the variance, which yields

$$\mathcal{V}[\theta] = \frac{1}{2} \sum_{n=0}^{q-1} (\Delta I_n)^2 - \frac{1}{2q} \left(\sum_{n=0}^{q-1} \Delta I_n \right)^2. \tag{5.90}$$

Comparing this with the modified discrete-time action gradient functional

$$f[\theta, \mu] = \sum_{n=0}^{q-1} \left[\frac{1}{2} (\Delta I_n)^2 - \mu \theta_n \right], \tag{5.91}$$

it can be seen that the discrete-time QFMin and AGMin pseudo-orbits belong to a larger class of pseudo-orbits called **generalised discrete-time AGMin pseudo-orbits**, defined as the minimum of

$$\mathcal{V}[\theta] = \frac{1}{2} \sum_{n=0}^{q-1} (\Delta I_n)^2 - \eta[\theta] \tag{5.92}$$

over an arbitrary discrete-time (p, q)-periodic pseudo-orbit $\theta = \{\theta_0, \ldots, \theta_{q-1}\}$. These generalised discrete-time AGMin pseudo-orbits correspond to discrete-time QFMin pseudo-orbits when

$$\eta[\theta] = \frac{1}{2q} \left(\sum_{n=0}^{q-1} \Delta I_n \right)^2 \tag{5.93}$$

and to discrete-time AGMin pseudo-orbits when

$$\eta[\theta] = \mu \sum_{n=0}^{q-1} \theta_n. \tag{5.94}$$

It is worth comparing this with the continuous-time AGMin pseudo-orbits defined in Sections 3.6 and 3.7, where $\eta[\vartheta] = \mu \int_0^{2\pi q} \vartheta \, \mathrm{d}t$, and in Dewar, Hudson, and Gibson [19], where $\eta[\vartheta] = 0$. When generalised discrete-time AGMin pseudo-orbits foliate a torus, the torus is called a **generalised discrete-time AGMin torus**. Hence, discrete-time QFMin tori

and discrete-time AGMin tori are both special cases of generalised discrete-time AGMin tori.

Chapter 6

Reconciliation of Almost-Invariant Tori for Discrete-Time Systems

This chapter determines a coordinate transformation for the momentum, and shows how it can be used to formulate reconciled QFMin-ghost tori in discrete-time systems. The transformed momentum J is written in terms of θ and I, and shown to have periodicity that depends on $\theta(\Theta)$. The dynamics of reconciled discrete-time almost-invariant tori are laid out in full, and related to their non-reconciled counterparts. The symmetries of the Lagrangian generating function are redefined in terms of the transformed coordinates, along with almost-invariant curves and tori. The variational principle is also discretised so it can be implemented numerically, and the generating function is expanded perturbatively so as to derive a first-order approximation to the transformation $\theta = \theta(\Theta)$ between the reconciled and unreconciled QFMin and ghost tori.

6.1 The Transformed Momentum

As stated in Chapter 4, we seek a coordinate transformation $\theta \mapsto \Theta(I, \theta, t)$ that makes QFMin and ghost tori equivalent. Although we have already shown in Section 4.5 that this transformation is independent of I, we still need an analogous transformation for I, because Hamilton's equations are not preserved under the transformation $(\theta, I) \mapsto (\Theta, I)$. Suppose that the coordinate transformation under which QFMin and ghost tori are reconciled is given by $(\theta, I) \mapsto (\Theta, J)$. Then because this transformation must preserve Hamilton's equations, it must be **canonical** [10, 18], and therefore area-preserving, so we define it such that the Jacobian is unity. This is done by introducing the **Poisson bracket** [18]

$$\{\Theta, J\}_{(\theta,I)} \equiv \frac{\partial\Theta}{\partial\theta}\frac{\partial J}{\partial I} - \frac{\partial\Theta}{\partial I}\frac{\partial J}{\partial\theta} \tag{6.1}$$

and setting it equal to one. Because Θ is independent of I, we get

$$\frac{\partial\Theta}{\partial I} = 0, \tag{6.2}$$

which leads to the condition

$$\frac{\partial\Theta}{\partial\theta}\frac{\partial J}{\partial I} = 1. \tag{6.3}$$

Dividing both sides by $\partial\Theta/\partial\theta$ and integrating with respect to I, this implies that

$$J = \frac{\partial\theta}{\partial\Theta}I + c. \tag{6.4}$$

Now we assume that θ is the form $\theta = \theta(\Theta)$, which means that θ can be both a coordinate and a function, depending on the context. If we then choose c to be zero, we get the relationship

$$J = \theta'(\Theta) I. \tag{6.5}$$

Hence, the complete Hamiltonian coordinate transformation for reconciled QFMin-ghost tori is given by $(\theta, I) \mapsto (\Theta, J)$, where Θ and J are defined implicitly by

$$\theta = \theta(\Theta), \tag{6.6}$$

$$I = \frac{J}{\theta'(\Theta)}. \tag{6.7}$$

6.2 Periodicity of the Transformed Momentum

By construction, θ, I and Θ all have periodicity 2π. In order to determine the periodicity of J, we take the standard map

$$\bar{I} = I - k \sin\theta, \tag{6.8}$$

$$\bar{\theta} = \theta + I - k \sin\theta, \tag{6.9}$$

and make the coordinate transformation

$$\theta \mapsto \theta(\Theta), \tag{6.10}$$

$$I \mapsto \frac{J}{\theta'(\Theta)}, \tag{6.11}$$

which gives the transformed standard map

$$\bar{J} = \theta'(\bar{\Theta}) \left\{ \frac{J}{\theta'(\Theta)} - k \sin\big[\theta(\Theta)\big] \right\}, \tag{6.12}$$

$$\theta(\bar{\Theta}) = \theta(\Theta) + \frac{J}{\theta'(\Theta)} - k \sin\big[\theta(\Theta)\big]. \tag{6.13}$$

Making another transformation

$$\Theta \mapsto \Theta + 2\pi n, \tag{6.14}$$

$$J \mapsto J + 2\pi f, \tag{6.15}$$

where $n \in \mathbb{Z}$ and f is, as yet, an unknown function, it can be seen from Equations (6.12) and (6.13) that

$$\bar{J} + 2\pi\bar{f} = \theta'\big(\bar{\Theta} + 2\pi(n+1)\big) \left\{ \frac{J + 2\pi f}{\theta'(\Theta + 2\pi n)} - k \sin\big[\theta(\Theta + 2\pi n)\big] \right\}, \tag{6.16}$$

$$\theta\big(\bar{\Theta} + 2\pi(n+1)\big) = \theta(\Theta + 2\pi n) + \frac{J + 2\pi f}{\theta'(\Theta + 2\pi n)} - k \sin\big[\theta(\Theta + 2\pi n)\big], \tag{6.17}$$

where we have used the relationship $\bar{n} = n + 1$. These equations can be greatly simplified by expressing $\theta(\Theta)$ as a Fourier series

$$\theta(\Theta) = \Theta + \sum_{m=-\infty}^{\infty} \theta_m e^{im\Theta} \tag{6.18}$$

with Fourier coefficients θ_m (not to be confused with θ_n from Chapter 5) and deriving the periodicity conditions

$$\theta(\Theta + 2\pi n) = \theta(\Theta) + 2\pi n, \tag{6.19}$$

$$\theta'(\Theta + 2\pi n) = \theta'(\Theta), \tag{6.20}$$

$$\sin\big[\theta(\Theta + 2\pi n)\big] = \sin\big[\theta(\Theta)\big]. \tag{6.21}$$

Substituting the periodicity conditions into Equations (6.16) and (6.17) gives

$$\bar{J} + 2\pi\bar{f} = \theta'(\bar{\Theta})\left\{\frac{J + 2\pi f}{\theta'(\Theta)} - k\sin\big[\theta(\Theta)\big]\right\}, \tag{6.22}$$

$$\theta(\bar{\Theta}) + 2\pi = \theta(\Theta) + \frac{J + 2\pi f}{\theta'(\Theta)} - k\sin\big[\theta(\Theta)\big], \tag{6.23}$$

from which it can be seen that Equation (6.13) will only be 2π-periodic (as required for consistency with Equation (6.9) under Transformation (6.10)) if $f = \theta'(\Theta)$, which is consistent with Equation (6.22). It then follows from Equation (6.22) that J is $2\pi\theta'(\Theta)$-periodic, which is not surprising considering the nature of the transformation. Suppose that (θ, I)-space is divided into narrow strips of width ε and height 2π. When these strips are transformed into (Θ, J)-space, they remain vertical because the transformation $\theta \mapsto \theta(\Theta)$ is independent of J. However, because Θ depends on θ, the distances between the strips still change, so their heights have to be readjusted in order to preserve their area $(2\pi\varepsilon)$. Unfortunately, because the distances between these strips depend on θ, their heights must also depend on θ, and because their heights determine the periodicity of J, the periodicity of J must also depend on θ. Hence, the periodicity of J has no fundamental significance, unlike the periodicity of I.

6.3 The Transformed Discrete-Time Action and Action Gradient

The Lagrangian and Hamiltonian generating functions (Equations (5.10) and (5.23)) can easily be used to define new generating functions that depend solely on the transformed coordinates Θ and J. These generating functions are denoted by G rather than F, in order to stress their independence of the original coordinates. In the Lagrangian case, the transformed generating function is given by [25]

$$G(\Theta, \bar{\Theta}) = F\big(\theta(\Theta), \theta(\bar{\Theta})\big) = \frac{1}{2}\big[\theta(\Theta) - \theta(\bar{\Theta})\big]^2 - V\big(\theta(\Theta)\big), \tag{6.24}$$

whereas in the Hamiltonian case, the transformed generating function is given by

$$G(\Theta, J) = F\big(\theta(\Theta), J\big) = \frac{1}{2}J^2 - V\big(\theta(\Theta)\big), \tag{6.25}$$

where Θ, $\bar{\Theta}$ and J are dummy variables. Because $\theta_n = \theta(\Theta_n)$, it follows that the **action** can also be expressed in terms of G instead of F. By analogy with Equation (5.25), we define the action in terms of the transformed coordinates as [25,31]

$$S = \sum_{n=0}^{q-1} G(\Theta_n, \Theta_{n+1}) = \sum_{n=0}^{q-1} F\big(\theta(\Theta_n), \theta(\Theta_{n+1})\big). \tag{6.26}$$

Assuming, once again, that the **twist condition** [25]

$$\frac{\partial^2 G}{\partial\Theta\partial\bar{\Theta}} < 0 \quad \forall\Theta,\bar{\Theta}\in\mathbb{R} \tag{6.27}$$

holds, we can define the transformed momenta for each Θ_n as [25,31]

$$\begin{aligned} J_n^+ &= G_2(\Theta_{n-1},\Theta_n) \\ &= \theta'(\Theta_n)F_2\big(\theta(\Theta_{n-1}),\theta(\Theta_n)\big) \\ &= \theta'(\Theta_n)I_n^+ \end{aligned} \tag{6.28}$$

and

$$\begin{aligned} J_n^- &= G_1(\Theta_n,\Theta_{n+1}) \\ &= \theta'(\Theta_n)F_1\big(\theta(\Theta_n),\theta(\Theta_{n+1})\big) \\ &= \theta'(\Theta_n)I_n^-, \end{aligned} \tag{6.29}$$

where F_i and G_i denote the respective partial derivatives of F and G with respect to their ith variables. Physically, these represent the transformed momenta of the kicked rotor on either side of the kick at t_n, with J_n^- representing the momentum before the kick, and J_n^+ representing the momentum after the kick. This leads to the natural definition of the transformed action gradient, given by [25,31]

$$\begin{aligned} \Delta J_n &= J_n^+ - J_n^- \\ &= G_2(\Theta_{n-1},\Theta_n) + G_1(\Theta_n,\Theta_{n+1}) \\ &= \theta'(\Theta_n)\Big[F_2\big(\theta(\Theta_{n-1}),\theta(\Theta_n)\big) + F_1\big(\theta(\Theta_n),\theta(\Theta_{n+1})\big)\Big] \\ &= \theta'(\Theta_n)\Delta I_n. \end{aligned} \tag{6.30}$$

In analogy with Equation (5.30), we also have [25]

$$\Delta J_n = \frac{\partial S}{\partial\Theta_n} = \theta'(\Theta_n)\frac{\partial S}{\partial\theta_n} = \theta'(\Theta_n)\Delta I_n. \tag{6.31}$$

6.4 Symmetries of the Transformed Lagrangian Generating Function

The transformed generating function admits the same families of symmetries as the original one. For arbitary functions $P(\Theta)$, $Q(\Theta)$ and $R(\Theta)$, $\mathbb{T}$-symmetry is defined as invariance under [33]

$$G(\Theta,\bar{\Theta}) = G(\bar{\Theta},\Theta) + Q(\Theta) - Q(\bar{\Theta}), \tag{6.32}$$

$\mathbb{P}$-symmetry is defined as invariance under [33]

$$G(\Theta,\bar{\Theta}) = G(-\Theta,-\bar{\Theta}) + P(\Theta) - P(\bar{\Theta}), \tag{6.33}$$

and $\mathbb{PT}$-symmetry is defined as invariance under [33]

$$G(\Theta,\bar{\Theta}) = G(-\bar{\Theta},-\Theta) + R(\Theta) - R(\bar{\Theta}), \tag{6.34}$$

where $P(\Theta)$ is odd and $R(\Theta) = Q(\Theta) - P(\Theta)$ is even. It is easy to see that these equations are equivalent to Equations (5.33)–(5.35). As a consequence, these symmetries have the same effects on the transformed action as they do on the untransformed action, with $\mathbb{T}$-symmetry implying that

$$S = \sum_{n=0}^{q-1} G(\Theta_n, \Theta_{n+1}) \doteq \sum_{n=1}^{q} G(\Theta_n, \Theta_{n-1}), \tag{6.35}$$

$\mathbb{P}$-symmetry implying that

$$S = \sum_{n=0}^{q-1} G(\Theta_n, \Theta_{n+1}) \doteq \sum_{n=0}^{q-1} G(-\Theta_n, -\Theta_{n+1}), \tag{6.36}$$

and $\mathbb{PT}$-symmetry implying that

$$S = \sum_{n=0}^{q-1} G(\Theta_n, \Theta_{n+1}) \doteq \sum_{n=1}^{q} G(-\Theta_n, -\Theta_{n-1}), \tag{6.37}$$

where $\doteq$ denotes equality up to a constant plus terms depending only on the endpoints Θ_0 and Θ_n [33]. These equations will be used in Section 7.3 to constrain the reconciliation to be unique.

6.5 Transformed Discrete-Time Almost-Invariant Curves

We have already defined QFMin and ghost tori in terms of the reconciled coordinates (Θ, J) and in terms of discrete-time coordinates, but not both of them at once. We now proceed to unify these two formulations, the result of which would have been difficult to obtain without these separate formulations. It is assumed by default that the rigidity principle also holds for discrete-time systems, because discrete-time systems are just a subset of continuous-time systems under the kicked rotor dynamics. We also define the transformed $C^{\pm}$ curves such that they depend on $J^{\pm}$ rather than $I^{\pm}$, so in the transformed coordinate system (Θ, J), we have [25,31]

$$C^{\pm} = \bigcup_{n=0}^{q-1} C_n^{\pm}, \tag{6.38}$$

where

$$C_n^{\pm} = \{(\Theta_n(\Theta_0), J_n^{\pm}(\Theta_0))\}, \tag{6.39}$$

$\Theta_n(\Theta_0) = \Theta_0 + \iota t_n$ defines a one-parameter family of (p, q)-periodic pseudo-orbits, and $0 \leq \Theta_0 < 2\pi/q$. As with the untransformed coordinates, the $C^{\pm}$ curves are only equal in the case of the standard map when $k = 0$. The term ΔJ_n gives the vertical distance between the $C^{\pm}$ curves in (Θ, J)-space, with similar implications to the untransformed case, and the $C^{\pm}$ curves are the respective forward and backward images of the $C^{\mp}$ curves under the area-preserving twist map $T : (\Theta_n, J_n^-) \mapsto (\Theta_{n+1}, J_{n+1}^+)$ [25].

6.6 Transformed Discrete-Time QFMin and Ghost Tori

By analogy with Equations (4.42) and (5.49), we specify that the reconciled discrete-time QFMin-ghost tori must be the minimum of the **modified discrete-time quadratic flux functional** [17,25]

$$\varphi_2[\Gamma] = \frac{1}{2}\sum_{n=0}^{q-1}\int_0^{2\pi/q}(\Delta J_n)^2\,\mathrm{d}\Theta_n \tag{6.40}$$

under arbitrary variations of Γ. Imposing the reconciliation condition $\Theta_n'(\Theta_0) = 1$, which is the discrete-time analogue of Equation (4.56), the modified discrete-time quadratic flux functional can also be written as

$$\varphi_2[\Gamma] = \frac{1}{2}\sum_{n=0}^{q-1}\int_0^{2\pi/q}(\Delta J_n)^2\,\mathrm{d}\Theta_0, \tag{6.41}$$

where the integration is taken over Θ_0 instead of Θ_n. As a consequence of the pseudo-dynamics defined in Chapter 4, the Euler-Lagrange equation of the modified discrete-time quadratic flux functional is given by

$$\Delta J_n = \nu(\Theta_0), \tag{6.42}$$

which is analogous to Equation (4.46). Also, by analogy with Equations (4.50) and (5.51), we specify that the reconciled discrete-time QFMin-ghost tori must also be the loci of the **modified discrete-time action gradient flow** [17,25]

$$\Theta_n'(T) = -\Delta J_n, \tag{6.43}$$

where T is a continuous, timelike parameter equivalent to that used to define the reconciliation condition in Chapter 4.

6.7 The Discrete-Time Variational Principle

Finally, in order to complete the reconciliation between QFMin and ghost tori, the continuous-time variational principle must be adapted to discrete-time systems. This is achieved by replacing integrals over t with sums over n, and replacing $\vartheta_\Theta\,\delta S/\delta\theta$ with ΔJ_n in Equation (4.66). Then the **discrete-time variational principle for reconciled QFMin-ghost tori** is given by

$$\mathcal{V}[\theta] = \frac{1}{2}\int_0^{2\pi/q}\sum_{n=0}^{q-1}\left[\tilde{\mathbb{P}}(\Delta J_n)\right]^2\Big|_{\Theta_n=\Theta_0+\epsilon t_n}\mathrm{d}\Theta_0, \tag{6.44}$$

where $\theta = \{\theta_0,\ldots,\theta_{q-1}\}$ is a (p,q)-periodic pseudo-orbit, ϵ is the rational rotational transform $\epsilon = p/q$ corresponding to mutually prime integers p and q, $\mathcal{V}[\theta]$ is the objective function and

$$\tilde{\mathbb{P}}(\Delta J_n) = \Delta J_n - \frac{1}{q}\sum_{n=0}^{q-1}\Delta J_n. \tag{6.45}$$

By construction, $\mathcal{V}[\theta] = 0$ on all (p,q)-periodic pseudo-orbits that satisfy the discrete-time QFMin equation $\Delta J_n = \nu$, because both ΔJ_n and $\frac{1}{q}\sum_{n=0}^{q-1}\Delta J_n$ are equal to ν.

6.8 Perturbative Construction of the Reconciled QFMin-Ghost Tori

Now that we have defined the discrete-time variational principle, it is worthwhile doing a perturbative construction of the reconciled QFMin-ghost tori in order to double-check the numerical results that will be obtained in Chapters 7 and 8. Suppose that the generating function is given by

$$G(\Theta,\bar{\Theta}) \equiv F\big(\theta(\Theta),\theta(\bar{\Theta})\big) = \frac{1}{2}\big[\theta(\Theta)-\theta(\bar{\Theta})\big]^2 - \varepsilon \sum_{m=-\infty}^{\infty} V_m \mathrm{e}^{\mathrm{i}m\theta(\Theta)}, \tag{6.46}$$

where the potential $V(\theta(\Theta))$ is expressed as a complex Fourier series, $\mathrm{i} = \sqrt{-1}$ denotes the imaginary unit, t_n is 2π-periodic (thus implying that $\Delta t = 2\pi$), and the parameter ε is assumed to be small. Then the modified action gradient is given by substituting Equation (6.46) into Equation (6.30), which gives

$$\Delta J_n = \theta'(\Theta_n)\Delta I_n, \tag{6.47}$$

where

$$\Delta I_n = -\theta(\Theta_{n-1}) + 2\theta(\Theta_n) - \theta(\Theta_{n+1}) - \mathrm{i}\varepsilon \sum_{m=-\infty}^{\infty} m V_m \mathrm{e}^{\mathrm{i}m\theta(\Theta_n)}. \tag{6.48}$$

This is just the original action gradient written in terms of the transformed coordinates. As part of the perturbative construction, we also express $\theta(\Theta_n)$ as a Fourier series

$$\theta(\Theta_n) = \Theta_n + \sum_{m=-\infty}^{\infty} \theta_m \mathrm{e}^{\mathrm{i}m\Theta_n} \tag{6.49}$$

and differentiate it with respect to Θ_n, to find

$$\theta'(\Theta_n) = 1 + \mathrm{i} \sum_{m=-\infty}^{\infty} m\theta_m \mathrm{e}^{\mathrm{i}m\Theta_n}. \tag{6.50}$$

In accordance with the variational principle defined by Equation (6.44), we proceed to eliminate Θ_n from these equations by evaluating them at $\Theta_n = \Theta_0 + \iota t_n$, where $t_n = 2\pi n$ is the discretised time and $\iota = p/q$ is the rational rotational transform corresponding to mutually prime integers p and q. This implies that $\Delta t = 2\pi$, and gives

$$\theta(\Theta_n)\Big|_{\Theta_n=\Theta_0+\iota t_n} = \Theta_0 + \iota t_n + \sum_{m=-\infty}^{\infty} \theta_m \mathrm{e}^{\mathrm{i}m(\Theta_0+\iota t_n)}, \tag{6.51}$$

$$\theta'(\Theta_n)\Big|_{\Theta_n=\Theta_0+\iota t_n} = 1 + \mathrm{i} \sum_{m=-\infty}^{\infty} m\theta_m \mathrm{e}^{\mathrm{i}m(\Theta_0+\iota t_n)}. \tag{6.52}$$

We also proceed to eliminate Θ_n from Equation (6.48) by substituting Equation (6.51) into the exponential term, which yields

$$\begin{aligned} \mathrm{e}^{\mathrm{i}m\theta(\Theta_n)}\Big|_{\Theta_n=\Theta_0+\mathfrak{k}t_n} &= \mathrm{e}^{\mathrm{i}m\left[\Theta_0+\mathfrak{k}t_n+\sum_{l=-\infty}^{\infty}\theta_l\mathrm{e}^{\mathrm{i}l(\Theta_0+\mathfrak{k}t_n)}\right]} \\ &= \mathrm{e}^{\mathrm{i}m(\Theta_0+\mathfrak{k}t_n)}\mathrm{e}^{\mathrm{i}m\sum_{l=-\infty}^{\infty}\theta_l\mathrm{e}^{\mathrm{i}l(\Theta_0+\mathfrak{k}t_n)}} \\ &= \mathrm{e}^{\mathrm{i}m(\Theta_0+\mathfrak{k}t_n)}\sum_{r=0}^{\infty}\frac{\left[\mathrm{i}m\sum_{l=-\infty}^{\infty}\theta_l\mathrm{e}^{\mathrm{i}l(\Theta_0+\mathfrak{k}t_n)}\right]^r}{r!}, \end{aligned} \tag{6.53}$$

where in the last line, the second exponential has been expanded as a Taylor series. For the remaining terms of Equation (6.48), we have

$$\begin{aligned} \left[-\theta(\Theta_{n-1})+2\theta(\Theta_n)-\theta(\Theta_{n+1})\right]\Big|_{\Theta_n=\Theta_0+\mathfrak{k}t_n} &= -\sum_{m=-\infty}^{\infty}\theta_m\mathrm{e}^{\mathrm{i}m[\Theta_0+\mathfrak{k}(t_n-2\pi)]} \\ &\quad +2\sum_{m=-\infty}^{\infty}\theta_m\mathrm{e}^{\mathrm{i}m(\Theta_0+\mathfrak{k}t_n)} \\ &\quad -\sum_{m=-\infty}^{\infty}\theta_m\mathrm{e}^{\mathrm{i}m[\Theta_0+\mathfrak{k}(t_n+2\pi)]} \\ &= \sum_{m=-\infty}^{\infty}\Big[\theta_m\mathrm{e}^{\mathrm{i}m(\Theta_0+\mathfrak{k}t_n)} \\ &\qquad \times\left(2-\mathrm{e}^{2\pi\mathrm{i}m\mathfrak{k}}-\mathrm{e}^{-2\pi\mathrm{i}m\mathfrak{k}}\right)\Big], \end{aligned} \tag{6.54}$$

where we have used the periodicity condition $t_{n\pm1}=t_n\pm2\pi$ derived from $t_n=n\Delta t=2\pi n$. Hence, the original action gradient can be written in terms of the transformed coordinates as

$$\begin{aligned} \Delta I_n\Big|_{\Theta_n=\Theta_0+\mathfrak{k}t_n} &= \sum_{m=-\infty}^{\infty}\theta_m\mathrm{e}^{\mathrm{i}m(\Theta_0+\mathfrak{k}t_n)}\left(2-\mathrm{e}^{2\pi\mathrm{i}m\mathfrak{k}}-\mathrm{e}^{-2\pi\mathrm{i}m\mathfrak{k}}\right) \\ &\quad -\mathrm{i}\varepsilon\sum_{m=-\infty}^{\infty}mV_m\mathrm{e}^{\mathrm{i}m(\Theta_0+\mathfrak{k}t_n)}\sum_{r=0}^{\infty}\frac{\left[\mathrm{i}m\sum_{l=-\infty}^{\infty}\theta_l\mathrm{e}^{\mathrm{i}l(\Theta_0+\mathfrak{k}t_n)}\right]^r}{r!}. \end{aligned} \tag{6.55}$$

Substituting Equations (6.52) and (6.55) into Equation (6.47), and noting that $\Delta J_n=\nu$ on each reconciled QFMin-ghost pseudo-orbit, leads to the condition

$$\begin{aligned} &\left[1+\mathrm{i}\sum_{m=-\infty}^{\infty}m\theta_m\mathrm{e}^{\mathrm{i}m(\Theta_0+\mathfrak{k}t_n)}\right] \\ &\quad\times\left\{\sum_{m=-\infty}^{\infty}\theta_m\mathrm{e}^{\mathrm{i}m(\Theta_0+\mathfrak{k}t_n)}\left(2-\mathrm{e}^{2\pi\mathrm{i}m\mathfrak{k}}-\mathrm{e}^{-2\pi\mathrm{i}m\mathfrak{k}}\right)\right. \\ &\qquad\left.-\mathrm{i}\varepsilon\sum_{m=-\infty}^{\infty}mV_m\mathrm{e}^{\mathrm{i}m(\Theta_0+\mathfrak{k}t_n)}\sum_{r=0}^{\infty}\frac{\left[\mathrm{i}m\sum_{l=-\infty}^{\infty}\theta_l\mathrm{e}^{\mathrm{i}l(\Theta_0+\mathfrak{k}t_n)}\right]^r}{r!}\right\}=\nu. \end{aligned} \tag{6.56}$$

Expanding ν and θ_m as $\nu = \sum_{m=1}^{\infty} \varepsilon^m \nu_m$ and $\theta_m = \sum_{j=1}^{\infty} \varepsilon^j \theta_m^{(j)}$, respectively, and substituting them into Equation (6.56), it can be seen that the perturbative expansion for reconciled QFMin-ghost tori is given by

$$\begin{aligned}
&\left[1 + \mathrm{i} \sum_{m=-\infty}^{\infty} m \mathrm{e}^{\mathrm{i}m(\Theta_0 + \mathfrak{t}t_n)} \sum_{j=1}^{\infty} \varepsilon^j \theta_m^{(j)}\right] \\
&\quad \times \left\{ \sum_{m=-\infty}^{\infty} \mathrm{e}^{\mathrm{i}m(\Theta_0 + \mathfrak{t}t_n)} \left(2 - \mathrm{e}^{2\pi \mathrm{i}m\mathfrak{t}} - \mathrm{e}^{-2\pi \mathrm{i}m\mathfrak{t}}\right) \sum_{j=1}^{\infty} \varepsilon^j \theta_m^{(j)} \right. \\
&\qquad \left. -\mathrm{i}\varepsilon \sum_{m=-\infty}^{\infty} m V_m \mathrm{e}^{\mathrm{i}m(\Theta_0 + \mathfrak{t}t_n)} \sum_{r=0}^{\infty} \frac{\left[\mathrm{i}m \sum_{l=-\infty}^{\infty} \mathrm{e}^{\mathrm{i}l(\Theta_0 + \mathfrak{t}t_n)} \sum_{j=1}^{\infty} \varepsilon^j \theta_l^{(j)}\right]^r}{r!} \right\} = \sum_{m=1}^{\infty} \varepsilon^m \nu_m,
\end{aligned} \tag{6.57}$$

which provides an excellent check for the numerical results that will be obtained in Chapters 7 and 8.

6.9 First-Order Perturbative Expansion

The most basic check for the numerical results is a first-order perturbative expansion. Equating the components of ε on both sides of Equation (6.57) with each other, it can be seen that the first-order perturbative expansion at $\mathcal{O}(\varepsilon)$ is given by

$$\sum_{m=-\infty}^{\infty} \theta_m^{(1)} \mathrm{e}^{\mathrm{i}m(\Theta_0 + \mathfrak{t}t_n)} \left(2 - \mathrm{e}^{2\pi \mathrm{i}m\mathfrak{t}} - \mathrm{e}^{-2\pi \mathrm{i}m\mathfrak{t}}\right) - \mathrm{i} \sum_{m=-\infty}^{\infty} m V_m \mathrm{e}^{\mathrm{i}m(\Theta_0 + \mathfrak{t}t_n)} = \nu_1. \tag{6.58}$$

However, ν_1 should exclude all but the **resonant terms**, which occur precisely when

$$2 - \mathrm{e}^{2\pi \mathrm{i}m\mathfrak{t}} - \mathrm{e}^{-2\pi \mathrm{i}m\mathfrak{t}} = 0. \tag{6.59}$$

Multiplying both sides by $\mathrm{e}^{2\pi \mathrm{i}m\mathfrak{t}}$ and completing the square, it can be seen that resonance occurs when

$$\mathrm{e}^{2\pi \mathrm{i}m\mathfrak{t}} = 1, \tag{6.60}$$

or more simply, when

$$m\mathfrak{t} \in \mathbb{Z}. \tag{6.61}$$

However, we can take this one step further by noting that because the unperturbed system has rational rotational transform, $\mathfrak{t} = p/q$, where p and q are mutually prime integers, so p cannot be an integer multiple of q, which implies that m must be an integer multiple of q in order to cancel out the denominator when $\mathfrak{t} = p/q$ is substituted into Equation (6.61). Hence, the **resonance condition** can also be written as

$$m \in q\mathbb{Z}. \tag{6.62}$$

Because the support of ν_1 must satisfy the resonance condition, it follows that

$$\nu_1 = \begin{cases} -\mathrm{i} \displaystyle\sum_{m=-\infty}^{\infty} m V_m \mathrm{e}^{\mathrm{i}m\Theta_0}, & \text{if } m \in q\mathbb{Z}; \\ 0, & \text{otherwise,} \end{cases} \tag{6.63}$$

which can be substituted back into Equation (6.58) to yield the first-order Fourier coefficients

$$\theta_m^{(1)} = \begin{cases} \dfrac{\mathrm{i}mV_m}{2 - \mathrm{e}^{2\pi \mathrm{i}m\hbar} - \mathrm{e}^{-2\pi \mathrm{i}m\hbar}}, & \text{if } m \notin q\mathbb{Z}; \\ c, & \text{otherwise,} \end{cases} \tag{6.64}$$

where c is any constant. However, because this creates a non-unique solution to Equation (6.58), we will set $c = 0$, which gives

$$\theta_m^{(1)} = \begin{cases} \dfrac{\mathrm{i}mV_m}{2 - \mathrm{e}^{2\pi \mathrm{i}m\hbar} - \mathrm{e}^{-2\pi \mathrm{i}m\hbar}}, & \text{if } m \notin q\mathbb{Z}; \\ 0, & \text{otherwise.} \end{cases} \tag{6.65}$$

This is in line with the conjugacy constraint imposed by Equation (7.31) in Section 7.4.

In order to facilitate the comparison between the perturbative construction and the numerical analysis, we now suppose that the generating function has the form

$$G(\Theta, \bar{\Theta}) \equiv F\big(\theta(\Theta), \theta(\bar{\Theta})\big) = \frac{1}{2}\big[\theta(\Theta) - \theta(\bar{\Theta})\big]^2 + k \cos\big[\theta(\Theta)\big], \tag{6.66}$$

where $k \equiv \varepsilon$. Because the potential of $G(\Theta, \bar{\Theta})$ has the form $V\big(\theta(\Theta)\big) = -k \cos\big[\theta(\Theta)\big]$ when compared with Equation (6.24), and because it has the complex Fourier series expansion

$$\cos\big[\theta(\Theta)\big] = \frac{\mathrm{e}^{\mathrm{i}\theta(\Theta)} + \mathrm{e}^{-\mathrm{i}\theta(\Theta)}}{2}, \tag{6.67}$$

the Fourier coefficients corresponding to this potential are given by

$$V_m = \begin{cases} -\dfrac{1}{2}, & \text{for } |m| = 1; \\ 0, & \text{otherwise.} \end{cases} \tag{6.68}$$

This can easily be verified by substituting Equation (6.68) into Equation (6.46), and checking that it yields Equation (6.66). The Fourier coefficients corresponding to the potential can also be used to determine the first-order Fourier coefficients corresponding to $\theta(\Theta_n)$, by substituting Equation (6.68) into Equation (6.65), which gives

$$\theta_m^{(1)} = \begin{cases} -\dfrac{\mathrm{i}m}{2(2 - \mathrm{e}^{2\pi \mathrm{i}\hbar} - \mathrm{e}^{-2\pi \mathrm{i}\hbar})}, & \text{for } |m| = 1 \text{ and } 1 \notin q\mathbb{Z}; \\ 0, & \text{otherwise.} \end{cases} \tag{6.69}$$

They can also be used to verify that the first-order Fourier coefficients corresponding to $\theta(\Theta_n)$ satisfy the reality condition $\theta_m^{(j)*} = \theta_{-m}^{(j)}$, where * denotes the complex conjugate,

because

$$\theta_1^{(1)*} = \theta_{-1}^{(1)} = \frac{\mathrm{i}}{2(2 - \mathrm{e}^{2\pi \mathrm{i}t} - \mathrm{e}^{-2\pi \mathrm{i}t})}, \quad \text{whenever } 1 \notin q\mathbb{Z}. \tag{6.70}$$

Chapter 7

Numerical Construction and Implementation of the Discrete-Time Reconciliation

This chapter discusses the variational construction that allows the discrete-time variational principle to be implemented numerically, which is accomplished by expanding the transformation function $\theta(\Theta_n)$ as a Fourier series and substituting it into the variational principle. A reality condition is also applied to the variational construction in order to ensure that the transformation does not produce any points with an imaginary component, and the Fourier series is restricted to contain only odd basis functions because the generating function has $\mathbb{PT}$-symmetry, which implies that the transformation function is overdetermined. Finally, the resonant terms are excluded from the transformation function so as to remove the last remaining piece of non-uniqueness from it. The implementation of the numerical algorithm is then discussed in detail, with special discussions devoted to the speed of the algorithm, the numerical integration method and the numerical minimisation method.

7.1 Variational Construction of the Reconciled QFMin-Ghost Tori

We now proceed to construct $\theta(\Theta_n)$ in such a way that the Fourier coefficients θ_m can be determined numerically. Although this method still uses Fourier series, it is distinctly different to the perturbative construction because it seeks to determine each Fourier coefficient θ_m as a whole, rather than splitting them up into an infinite number of subcoefficients $\theta_m^{(1)}, \theta_m^{(2)}, \theta_m^{(3)}, \ldots$ and calculating them individually. Because of the practical impossibility of calculating an infinite number of subcoefficients for each Fourier coefficient explicitly, it would seem that the variational construction necessarily leads to a much more accurate set of results than the perturbative construction, at least for individual Fourier coefficients, provided that the computational resources exist to implement it. However, this is not necessarily the case, because the perturbative construction is able to calculate approximations to an infinite number of Fourier coefficients simultaneously, whereas the variational construction is only able to calculate solutions to a finite number of Fourier coefficients within a finite amount of time, and although those solutions are extremely accurate, that still leaves an infinite number of Fourier coefficients without even an approximation, even if they do not contribute much to the final result. Whether the perturbative construction or the variational construction is more accurate depends on the problem, but because the

variational construction is easier to implement numerically, we will use it to construct reconciled QFMin-ghost tori instead of the perturbative construction. Suppose that the generating function is given by

$$G(\Theta,\bar{\Theta}) \equiv F\big(\theta(\Theta),\theta(\bar{\Theta})\big) = \frac{1}{2}\big[\theta(\Theta)-\theta(\bar{\Theta})\big]^2 + k\cos\big[\theta(\Theta)\big]. \tag{7.1}$$

Then the modified action gradient is given by substituting Equation (7.1) into Equation (6.30), which gives

$$\Delta J_n = \theta'(\Theta_n)\Delta I_n, \tag{7.2}$$

where

$$\Delta I_n = -\theta(\Theta_{n-1}) + 2\theta(\Theta_n) - \theta(\Theta_{n+1}) - k\sin\big[\theta(\Theta_n)\big]. \tag{7.3}$$

This is just the original action gradient written in terms of the transformed coordinates. Also suppose that $\theta(\Theta_n)$ can be written as a truncated Fourier series

$$\theta(\Theta_n) = \Theta_n + \lim_{j\to\infty}\sum_{m=-j}^{j}\theta_m \mathrm{e}^{\mathrm{i}m\Theta_n}, \tag{7.4}$$

where $\mathrm{i} = \sqrt{-1}$ and $j \in \mathbb{Z}^+$, and that it can be differentiated with respect to Θ_n to give

$$\theta'(\Theta_n) = 1 + \mathrm{i}\lim_{j\to\infty}\sum_{m=-j}^{j} m\theta_m \mathrm{e}^{\mathrm{i}m\Theta_n}. \tag{7.5}$$

(Note that j has a different meaning in Chapter 7 to what it did in Chapter 6.) Then, in accordance with the variational principle defined by Equation (6.44), we eliminate Θ_n from these equations by evaluating them at $\Theta_n = \Theta_0 + \epsilon t_n$, where $t_n = 2\pi n$ is the discretised time and $\epsilon = p/q$ is the rational rotational transform corresponding to mutually prime integers p and q. This implies that $\Delta t = 2\pi$, and gives

$$\theta(\Theta_n)\Big|_{\Theta_n=\Theta_0+\epsilon t_n} = \Theta_0 + \epsilon t_n + \lim_{j\to\infty}\sum_{m=-j}^{j}\theta_m \mathrm{e}^{\mathrm{i}m(\Theta_0+\epsilon t_n)}, \tag{7.6}$$

$$\theta'(\Theta_n)\Big|_{\Theta_n=\Theta_0+\epsilon t_n} = 1 + \mathrm{i}\lim_{j\to\infty}\sum_{m=-j}^{j} m\theta_m \mathrm{e}^{\mathrm{i}m(\Theta_0+\epsilon t_n)}. \tag{7.7}$$

Substituting the first of these equations into $\sin\big[\theta(\Theta_n)\big]$ yields

$$\sin\big[\theta(\Theta_n)\big]\Big|_{\Theta_n=\Theta_0+\epsilon t_n} = \sin\left[\Theta_0 + \epsilon t_n + \lim_{j\to\infty}\sum_{m=-j}^{j}\theta_m \mathrm{e}^{\mathrm{i}m(\Theta_0+\epsilon t_n)}\right] \tag{7.8}$$

for the potential. We also have

$$\begin{aligned}\left[-\theta(\Theta_{n-1})+2\theta(\Theta_n)-\theta(\Theta_{n+1})\right]\Big|_{\Theta_n=\Theta_0+\imath t_n} &= -\lim_{j\to\infty}\sum_{m=-j}^{j}\theta_m \mathrm{e}^{\mathrm{i}m[\Theta_0+\imath(t_n-2\pi)]}\\ &\quad+2\lim_{j\to\infty}\sum_{m=-j}^{j}\theta_m \mathrm{e}^{\mathrm{i}m(\Theta_0+\imath t_n)}\\ &\quad-\lim_{j\to\infty}\sum_{m=-j}^{j}\theta_m \mathrm{e}^{\mathrm{i}m[\Theta_0+\imath(t_n+2\pi)]}\\ &=\lim_{j\to\infty}\sum_{m=-j}^{j}\Big[\theta_m \mathrm{e}^{\mathrm{i}m(\Theta_0+\imath t_n)}\\ &\qquad\times\left(2-\mathrm{e}^{2\pi\mathrm{i}m\imath}-\mathrm{e}^{-2\pi\mathrm{i}m\imath}\right)\Big],\end{aligned} \tag{7.9}$$

where we have used the periodicity condition $t_{n\pm1}=t_n\pm 2\pi$ derived from $t_n=n\Delta t=2\pi n$. Hence, the original action gradient is given by

$$\begin{aligned}\Delta I_n\Big|_{\Theta_n=\Theta_0+\imath t_n} &= \lim_{j\to\infty}\sum_{m=-j}^{j}\theta_m \mathrm{e}^{\mathrm{i}m(\Theta_0+\imath t_n)}\left(2-\mathrm{e}^{2\pi\mathrm{i}m\imath}-\mathrm{e}^{-2\pi\mathrm{i}m\imath}\right)\\ &\quad-k\sin\left[\Theta_0+\imath t_n+\lim_{j\to\infty}\sum_{m=-j}^{j}\theta_m \mathrm{e}^{\mathrm{i}m(\Theta_0+\imath t_n)}\right].\end{aligned} \tag{7.10}$$

Multiplying this by Equation (7.7) yields the modified action gradient

$$\begin{aligned}\Delta J_n\Big|_{\Theta_n=\Theta_0+\imath t_n} &= \left[1+\mathrm{i}\lim_{j\to\infty}\sum_{m=-j}^{j}m\theta_m \mathrm{e}^{\mathrm{i}m(\Theta_0+\imath t_n)}\right]\\ &\quad\times\left\{\lim_{j\to\infty}\sum_{m=-j}^{j}\theta_m \mathrm{e}^{\mathrm{i}m(\Theta_0+\imath t_n)}\left(2-\mathrm{e}^{2\pi\mathrm{i}m\imath}-\mathrm{e}^{-2\pi\mathrm{i}m\imath}\right)\right.\\ &\quad\left.-k\sin\left[\Theta_0+\imath t_n+\lim_{j\to\infty}\sum_{m=-j}^{j}\theta_m \mathrm{e}^{\mathrm{i}m(\Theta_0+\imath t_n)}\right]\right\}.\end{aligned} \tag{7.11}$$

Finally, in order to complete the variational construction, the modified action gradient is substituted into the discrete-time variational principle

$$\mathcal{V}[\theta_{-j},\ldots,\theta_j]=\frac{1}{2}\int_0^{2\pi/q}\sum_{n=0}^{q-1}\left[\tilde{\mathbb{P}}\left(\Delta J_n\right)\right]^2\Big|_{\Theta_n=\Theta_0+\imath t_n}\mathrm{d}\Theta_0, \tag{7.12}$$

where

$$\tilde{\mathbb{P}}\left(\Delta J_n\right)=\Delta J_n-\frac{1}{q}\sum_{n=0}^{q-1}\Delta J_n \tag{7.13}$$

and

$$\Delta J_n=\Delta J_n[\theta_{-j},\ldots,\theta_j]. \tag{7.14}$$

7.2 Imposition of the Reality Condition

Because $\theta(\Theta_n)$ is real, we must impose a reality condition on the Fourier coefficients in order to ensure that the results we obtain from the numerical analysis are not imaginary or complex-valued. This **reality condition** is given by [16,17]

$$\theta_m^* = \theta_{-m}, \tag{7.15}$$

where * denotes the complex conjugate and m ranges over $1 \leq m \leq j$. Applying this constraint to Equation (7.11) reveals that

$$\begin{aligned}\Delta J_n\Big|_{\Theta_n=\Theta_0+\epsilon t_n} = &\left\{1 + \mathrm{i}\lim_{j\to\infty}\sum_{m=1}^{j} m\left[\theta_m \mathrm{e}^{\mathrm{i}m(\Theta_0+\epsilon t_n)} - \theta_m^* \mathrm{e}^{-\mathrm{i}m(\Theta_0+\epsilon t_n)}\right]\right\} \\ &\times \left(\lim_{j\to\infty}\sum_{m=1}^{j}\left\{\left[\theta_m \mathrm{e}^{\mathrm{i}m(\Theta_0+\epsilon t_n)} + \theta_m^* \mathrm{e}^{-\mathrm{i}m(\Theta_0+\epsilon t_n)}\right]\right.\right. \\ &\qquad \left.\times\left(2 - \mathrm{e}^{2\pi\mathrm{i}m\epsilon} - \mathrm{e}^{-2\pi\mathrm{i}m\epsilon}\right)\right\} \\ &- k\sin\left\{\Theta_0 + \epsilon t_n + \theta_m\Big|_{m=0}\right. \\ &\qquad \left.\left. + \lim_{j\to\infty}\sum_{m=1}^{j}\left[\theta_m \mathrm{e}^{\mathrm{i}m(\Theta_0+\epsilon t_n)} + \theta_m^* \mathrm{e}^{-\mathrm{i}m(\Theta_0+\epsilon t_n)}\right]\right\}\right),\end{aligned} \tag{7.16}$$

whereas applying it to Equations (7.6) and (7.7) gives

$$\theta(\Theta_n)\Big|_{\Theta_n=\Theta_0+\epsilon t_n} = \Theta_0 + \epsilon t_n + \theta_m\Big|_{m=0} + \lim_{j\to\infty}\sum_{m=1}^{j}\left[\theta_m \mathrm{e}^{\mathrm{i}m(\Theta_0+\epsilon t_n)} + \theta_m^* \mathrm{e}^{-\mathrm{i}m(\Theta_0+\epsilon t_n)}\right], \tag{7.17}$$

$$\theta'(\Theta_n)\Big|_{\Theta_n=\Theta_0+\epsilon t_n} = 1 + \mathrm{i}\lim_{j\to\infty}\sum_{m=1}^{j} m\left[\theta_m \mathrm{e}^{\mathrm{i}m(\Theta_0+\epsilon t_n)} - \theta_m^* \mathrm{e}^{-\mathrm{i}m(\Theta_0+\epsilon t_n)}\right], \tag{7.18}$$

where $\theta_m\big|_{m=0}$ is the Fourier coefficient at $m = 0$, which should not be written as θ_0 so as to avoid confusion with the parameter $\theta_0 = \theta_n\big|_{n=0}$ described in Chapters 3–5. This confusion arises because θ_m is used to represent the Fourier coefficients of $\theta(\Theta_n)$, whereas θ_n is used to represent the value of θ at time t_n. Nevertheless, because $\theta_m\big|_{m=0}$ merely represents a translational symmetry about the origin, we have chosen to set $\theta_m\big|_{m=0} = 0$ throughout the rest of this thesis. Hence, the modified action gradient takes the form

$$\Delta J_n = \Delta J_n[\theta_1, \ldots, \theta_j, \theta_1^*, \ldots, \theta_j^*] \tag{7.19}$$

and the variational principle takes the form

$$\mathcal{V}[\theta_1, \ldots, \theta_j, \theta_1^*, \ldots, \theta_j^*] = \frac{1}{2}\int_0^{2\pi/q}\sum_{n=0}^{q-1}\left[\tilde{\mathbb{P}}\left(\Delta J_n\right)\right]^2\Big|_{\Theta_n=\Theta_0+\epsilon t_n} \mathrm{d}\Theta_0. \tag{7.20}$$

7.3 Restriction to Odd Basis Functions

Recall the definitions of $\mathbb{T}$-symmetry and $\mathbb{P}$-symmetry that we introduced in Sections 5.4 and 6.4. We know from Meiss [7] that in the case of the standard map, $G(\Theta, \bar{\Theta})$ has $\mathbb{T}$-symmetry. Now we assume that $G(\Theta, \bar{\Theta})$ also has $\mathbb{PT}$-symmetry, which unlike $\mathbb{P}$-symmetry and $\mathbb{T}$-symmetry in general, implies that the signs of $\theta_{n+1} - \theta_n$ and $\Theta_{n+1} - \Theta_n$ are not reversed [33]. It follows that the QFMin equation of a generating function that admits $\mathbb{PT}$-symmetry has its own special symmetries that preserve the rotational transform ι [33]. Hence, the QFMin equation has a multiplicity of solutions, which can be reduced by constraining the Fourier series to only contain odd basis functions. To do this, we assume that the Fourier coefficients θ_m are purely imaginary, so that they have the form

$$\theta_m = \mathrm{i} y_m, \tag{7.21}$$

where $y_m \in \mathbb{R}$ and $m \in \mathbb{Z}^+$. Substituting this into Equation (7.16) with $\theta_m\big|_{m=0} = 0$ gives the modified action gradient as

$$\begin{aligned}\Delta J_n\Big|_{\Theta_n = \Theta_0 + \iota t_n} = &\left\{1 - \lim_{j\to\infty} \sum_{m=1}^{j} m y_m \left[\mathrm{e}^{\mathrm{i}m(\Theta_0 + \iota t_n)} + \mathrm{e}^{-\mathrm{i}m(\Theta_0 + \iota t_n)}\right]\right\} \\ &\times \left(\mathrm{i} \lim_{j\to\infty} \sum_{m=1}^{j} y_m \left[\mathrm{e}^{\mathrm{i}m(\Theta_0 + \iota t_n)} - \mathrm{e}^{-\mathrm{i}m(\Theta_0 + \iota t_n)}\right]\left(2 - \mathrm{e}^{2\pi \mathrm{i} m \iota} - \mathrm{e}^{-2\pi \mathrm{i} m \iota}\right)\right. \\ &\left. -k \sin\left\{\Theta_0 + \iota t_n + \mathrm{i} \lim_{j\to\infty} \sum_{m=1}^{j} y_m \left[\mathrm{e}^{\mathrm{i}m(\Theta_0 + \iota t_n)} - \mathrm{e}^{-\mathrm{i}m(\Theta_0 + \iota t_n)}\right]\right\}\right).\end{aligned} \tag{7.22}$$

However, this can be greatly simplified by replacing the exponentials with sines and cosines, so that the modified action gradient becomes

$$\begin{aligned}\Delta J_n\Big|_{\Theta_n = \Theta_0 + \iota t_n} = &\left\{1 - 2 \lim_{j\to\infty} \sum_{m=1}^{j} m y_m \cos\big[m(\Theta_0 + \iota t_n)\big]\right\} \\ &\times \left(-4 \lim_{j\to\infty} \sum_{m=1}^{j} y_m \sin\big[m(\Theta_0 + \iota t_n)\big]\big[1 - \cos(2\pi m \iota)\big]\right. \\ &\left. -k \sin\left\{\Theta_0 + \iota t_n - 2 \lim_{j\to\infty} \sum_{m=1}^{j} y_m \sin\big[m(\Theta_0 + \iota t_n)\big]\right\}\right).\end{aligned} \tag{7.23}$$

Moreover, substituting Equation (7.21) into Equation (7.17) with $\theta_m\big|_{m=0} = 0$, it can be seen that $\theta(\Theta_n)$ is given by

$$\theta(\Theta_n)\Big|_{\Theta_n = \Theta_0 + \iota t_n} = \Theta_0 + \iota t_n + \mathrm{i} \lim_{j\to\infty} \sum_{m=1}^{j} y_m \left[\mathrm{e}^{\mathrm{i}m(\Theta_0 + \iota t_n)} - \mathrm{e}^{-\mathrm{i}m(\Theta_0 + \iota t_n)}\right], \tag{7.24}$$

which can also be written in terms of trigonometric functions as

$$\theta(\Theta_n)\Big|_{\Theta_n = \Theta_0 + \iota t_n} = \Theta_0 + \iota t_n - 2 \lim_{j\to\infty} \sum_{m=1}^{j} y_m \sin\big[m(\Theta_0 + \iota t_n)\big]. \tag{7.25}$$

Similarly, substituting Equation (7.21) into Equation (7.18) shows that the derivative of $\theta(\Theta_n)$ is given by

$$\theta'(\Theta_n)\Big|_{\Theta_n=\Theta_0+\imath t_n} = 1 - 2\lim_{j\to\infty}\sum_{m=1}^{j} m y_m \cos\left[m(\Theta_0+\imath t_n)\right], \tag{7.26}$$

so that the modified action gradient takes the form

$$\Delta J_n = \Delta J_n[y_1,\ldots,y_j] \tag{7.27}$$

and the variational principle takes the form

$$\mathcal{V}[y_1,\ldots,y_j] = \frac{1}{2}\int_0^{2\pi/q}\sum_{n=0}^{q-1}\left[\tilde{\mathbb{P}}\left(\Delta J_n\right)\right]^2\Big|_{\Theta_n=\Theta_0+\imath t_n} \mathrm{d}\Theta_0. \tag{7.28}$$

7.4 Exclusion of the Resonant Terms

Even after restricting the Fourier series expansion of $\theta(\Theta_n)$ to contain only odd basis functions, there is still a certain amount of multiplicity in the solution to the variational principle because it is invariant under an arbitrary relabelling of the pseudo-orbits $\Theta \mapsto \bar{\Theta}$. This lack of uniqueness can also be seen in Equation (6.65) of the perturbative construction, and is discussed more fully in Dewar and Khorev [25]. In order to remove this arbitrariness and ensure the uniqueness of the pseudo-orbits, we constrain

$$\sum_{n=0}^{q-1}\theta(\Theta_n(\Theta_0)) \tag{7.29}$$

to be monotone by making it a linear function of Θ_0 [25]. This is looser than the condition that every term in the sum, $\theta(\Theta_n(\Theta_0))$, be monotone in Θ_0, which Dewar and Meiss [33] found to be too restrictive because the monotonicity of $\theta(\Theta_n(\Theta_0))$ breaks down at much lower k values than the monotonicity of $\sum_{n=0}^{q-1}\theta(\Theta_n(\Theta_0))$. The first step in constraining $\theta(\Theta_n(\Theta_0))$ to be monotone is to separate the part that's linear in Θ_0 from that which is nonlinear, i.e.

$$\theta(\Theta_n(\Theta_0)) = \theta(\Theta_0+\imath t_n) = \Theta_0 + \imath t_n + \xi_n, \tag{7.30}$$

where $\xi_n = \xi(\Theta_0+\imath t_n)$ is the nonlinear part of $\theta(\Theta_n(\Theta_0))$ [25]. Thus, to ensure the linearity and therefore monotonicity of $\sum_{n=0}^{q-1}\theta(\Theta_n(\Theta_0))$, we set

$$\sum_{n=0}^{q-1}\xi_n = 0, \tag{7.31}$$

so the nonlinear component of $\sum_{n=0}^{q-1}\theta(\Theta_n(\Theta_0))$ is zero [25]. It then follows that because $\sum_{n=0}^{q-1}\mathrm{d}\xi_n/\mathrm{d}\Theta_0 = 0$,

$$\sum_{n=0}^{q-1}\frac{\mathrm{d}\theta(\Theta_n(\Theta_0))}{\mathrm{d}\Theta_0} = 1 > 0 \quad \forall\Theta_0, \tag{7.32}$$

so $\sum_{n=0}^{q-1}\Theta_n(\Theta_0)$ is monotone (as required). Returning to Equation (7.25), which is evaluated at $\Theta_n = \Theta_0 + \imath t_n$, where $\imath$ is the rational rotational transform $\imath = p/q$ corresponding

to mutually prime integers p and q, we notice from Equation (7.30) that

$$\xi_n = -2 \lim_{j\to\infty} \sum_{m=1}^{j} y_m \sin\left[m(\Theta_0 + \epsilon t_n)\right]. \tag{7.33}$$

Substituting Equation (7.33) into Equation (7.31), it can be seen that

$$-2 \lim_{j\to\infty} \sum_{m=1}^{j} y_m \sum_{n=0}^{q-1} \sin\left[m(\Theta_0 + \epsilon t_n)\right] = 0 \tag{7.34}$$

is the condition we need to ensure the monotonicity of $\sum_{n=0}^{q-1} \theta(\Theta_n(\Theta_0))$. Because p and q are mutually prime integers and $t_n = 2\pi n$, it follows that $\sum_{n=0}^{q-1} \sin\left[m(\Theta_0+\epsilon t_n)\right] = 0$ whenever m is not an integer multiple of q, so these terms automatically satisfy the constraint (Equation (7.34)) [25]. However, when m is an integer multiple of q, the corresponding terms in the Fourier series may contribute to $\sum_{n=0}^{q-1} \xi_n$ and must be eliminated by setting their Fourier coefficients to zero [25] (compare Section 6.9). Hence, the requirement that $\sum_{n=0}^{q-1} \theta(\Theta_n(\Theta_0))$ be monotone is equivalent to the constraint that the resonant terms of the Fourier series be equal to zero. This is called a **conjugacy constraint**, and it implies that the action gradient is given by

$$\begin{aligned} \Delta J_n\Big|_{\Theta_n=\Theta_0+\epsilon t_n} = &\left\{1 - 2 \lim_{j\to\infty} \sum_{m=1}^{j}{}' m y_m \cos\left[m(\Theta_0 + \epsilon t_n)\right]\right\} \\ &\times \left(-4 \lim_{j\to\infty} \sum_{m=1}^{j}{}' y_m \sin\left[m(\Theta_0 + \epsilon t_n)\right]\left[1 - \cos(2\pi m\epsilon)\right]\right. \\ &\left. -k \sin\left\{\Theta_0 + \epsilon t_n - 2 \lim_{j\to\infty} \sum_{m=1}^{j}{}' y_m \sin\left[m(\Theta_0 + \epsilon t_n)\right]\right\}\right), \end{aligned} \tag{7.35}$$

where the prime on the sum denotes the exclusion of the resonant terms with $m \in q\mathbb{Z}$. It also implies that

$$\theta(\Theta_n)\Big|_{\Theta_n=\Theta_0+\epsilon t_n} = \Theta_0 + \epsilon t_n - 2 \lim_{j\to\infty} \sum_{m=1}^{j}{}' y_m \sin\left[m(\Theta_0 + \epsilon t_n)\right], \tag{7.36}$$

$$\theta'(\Theta_n)\Big|_{\Theta_n=\Theta_0+\epsilon t_n} = 1 - 2 \lim_{j\to\infty} \sum_{m=1}^{j}{}' m y_m \cos\left[m(\Theta_0 + \epsilon t_n)\right], \tag{7.37}$$

where the prime on the sum has the same meaning as for Equation (7.35).

7.5 Stages of the Implementation

All stages of the numerical implementation were performed using the Wolfram *Mathematica*® software package (versions 7 [35] and 8 [36]). The first stage was to draw Poincaré plots of the standard map, overlayed with the unreconciled QFMin and ghost curves, by using Equations (5.27) and (5.28). Although this stage was rather elementary, it was important to develop a numerical solution for the unreconciled QFMin and ghost curves

so their plots could be compared with those of the reconciled QFMin-ghost curves later on. In particular, the unreconciled QFMin curves were plotted by finding the differences $\Delta I_{n+1} - \Delta I_n = 0$ in the Euler-Lagrange equation $\Delta I_n = \nu(\theta_0)$ between successive time intervals and minimising the sum of their squares, which is equivalent to minimising Equation (5.90). A constraint similar to that imposed in Section 7.4 was used to ensure the uniqueness of the QFMin pseudo-orbits, which involved minimising the sum of the squares of $\xi_n = \theta_n - \theta_0 - \epsilon t_n$. This constraint was unnecessary in the analytical case (Equation (5.49)), because we were integrating and summing over a single action gradient, whereas in the numerical case, we wish to dispense with the integration altogether, and in order to do this, we have to minimise the *differences* between the action gradients. This causes the integrability parameter $\nu(\theta_0)$ to vanish identically from the variational principle, thus necessitating a new constraint $\sum_{n=0}^{q-1} \xi_n = 0$ that sets ΔI_n to be constant with respect to n. Cross-sections of the action-minimax and action-minimising orbits were also plotted by minimising the sum of the squares of Equation (5.29), in order to check that the unreconciled QFMin and ghost curves passed through them. Code was written to convert the Poincaré plots from the topological covering space to the topological base space, thereby producing polar plots.

The next stage of the implementation was to write an algorithm to minimise Equation (7.28), with $\tilde{\mathbb{P}}(\Delta J_n)$ given by Equation (7.13) and ΔJ_n given by Equation (7.35). The resulting Fourier coefficients were then plotted in a power spectrum to compare their relative and absolute values, along with a plot of the minima of Equation (7.28). After this, the Fourier series were truncated in order to exclude terms that were no longer approaching convergence, and the terms that remained were substituted into Equations (7.36) and (7.37) in order to determine whether Equation (7.36) was monotone for each particular combination of k and ϵ. If Equation (7.36) ceased to be monotone, then the plot of Equation (7.37) would intersect the horizontal axis, in which case the reconciliation was deemed to be invalid for that particular combination of k and ϵ. If Equation (7.36) was monotone, then Equations (5.27) and (5.28) were used in combination with Equation (7.36) and $\theta_n = \theta(\Theta_n)$ in order to plot the reconciled QFMin-ghost curves in both (θ, I)-space and (Θ, I)-space. The (θ, I) plots were useful for comparing the reconciled QFMin-ghost curves with their unreconciled counterparts, whereas the (Θ, I) plots were useful for testing the correctness and accuracy of the transformation. This was facilitated by converting the action-minimax and action-minimising orbits to (Θ, I)-space using Equation (7.36) with $\theta_n = \theta(\Theta_n)$, and checking that the Poincaré plots of the action-minimax and action-minimising orbits formed straight, vertical, equidistant lines in (Θ, I)-space. The reconciled QFMin-ghost curves were also plotted in (Θ, J)-space, but these plots were not included in this thesis because J does not have a constant periodicity with respect to Θ. Next, the differences between the reconciled QFMin-ghost curves C^+ and C^- were plotted in (Θ, J)-space, in order to show that their amplitudes were constant with respect to Θ. Finally, the amplitudes of the difference curves were plotted as a function of $1/q$ for each k value, and the gradients of the linear interpolations between the amplitudes of constant k were used to determine flux-leakage exponents α_k. Three different approximations were obtained to each flux-leakage exponent, and because these approximations were interpolated, extrapolated and plotted as a function of k, it was easy to get an idea as to whether the reconciled QFMin-ghost curves were consistent with Greene's residue criterion and the existence of KAM tori within the standard map with rotational transform equal to two minus the golden mean for $k < 0.971635\ldots$, which is the value at which the last KAM curves break up.

7.6 Speed of the Algorithm

The speed of the numerical algorithm depended heavily on the integration and minimisation methods, which will be discussed in Sections 7.7 and 7.8, respectively. However, there were also some other factors that had an impact on this, which will be discussed here. For example, it was found that because of the nonlinearity of the integrand of Equation (7.28), the integration had to be performed numerically. Because the coefficients of the Fourier series were unknown variables, they had to be restricted to numerical values, and this had a small but noticeable impact on the code's performance. It was important to find ways to maximise the code's speed, so that calculations could be performed within a reasonable timeframe.

One of the more obvious ways to increase the code's speed was to use the computational formula for the variance

$$\sum_{n=0}^{q-1}\left[\tilde{\mathbb{P}}(\Delta J_n)\right]^2 = \sum_{n=0}^{q-1}(\Delta J_n)^2 - \frac{1}{q}\left(\sum_{n=0}^{q-1}\Delta J_n\right)^2 \tag{7.38}$$

in order to eliminate a large number of terms from the integrand that would ultimately have been equal to zero. However, because this code was already much faster than the rest of the algorithm, the variance formula was never substituted into the objective function unless differentiation was required. Another way to increase the code's speed was to exclude the resonant terms from the integrand right at the very beginning of the algorithm, rather than setting them equal to zero towards the end of it. Changing the accuracy and precision goals also had an impact on the performance of the algorithm, and it was generally found that setting the accuracy goal to 6 and the precision goal to ∞ provided the best trade-off between accuracy and speed. Setting the accuracy goal too low made it difficult to get the Fourier series to converge, whereas setting the accuracy goal too high often led to computer-generated warnings about insufficient working precision, and these could only be avoided by decreasing the accuracy goal and therefore increasing the code's speed. The precision goal had very little impact on the code's speed, so it was set to ∞ in order to maximise the accuracy of the results. Some attempts were also made to increase the working precision and the number of recursions that were used by the integration algorithm, in the hope that this would reduce the number of errors that were encountered when increasing the accuracy goal. However, because they dramatically reduced the speed of the algorithm without providing any noticeable improvement in the accuracy of the results, such plans eventually had to be abandoned. It is thought that hardware may have been the limiting factor in this case.

Besides increasing the working precision, it was also believed that employing the **continuation method** [37], which was used extensively to increase the accuracy of the action-minimax and action-minimising orbits, would also increase the accuracy of the Fourier coefficients. In the case of the action-minimax and action-minimising orbits, the continuation method reduced errors by minimising the risk of ending up on the wrong node of a bifurcation, and of the computational algorithm producing an action-minimax orbit when asked for an action-minimising orbit, or vice versa. Because it is significantly easier to calculate action-minimax and action-minimising orbits when k is small than when k is large, the continuation method yielded a five- to ten-fold increase in the computational speed when it was used for this purpose. Unfortunately, for the numerical algorithm that was used to calculate the Fourier coefficients in the reconciliation between QFMin and

ghost tori, the amount of time that it takes to run the algorithm at low k is of a similar magnitude to the amount of time that it takes to run the algorithm at high k, so the continuation method invariably slowed the algorithm down. Because many tests also showed that the continuation method did little, if anything, to increase the accuracy of the Fourier coefficients, and because it typically increased the computational time by a factor of five to ten, it was decided to avoid using the continuation method for these purposes.

Attempts were also made to see whether calculating the first few coefficients of the Fourier series and then using them as initial conditions to calculate the rest of the coefficients would increase the speed of the calculation. Although in some special cases, success was obtained, there was no simple formula for determining when and under what conditions this would be the case, and because this method tended to decrease the algorithm's speed in generic cases, it had to be abandoned for practical reasons.

7.7 The Integration Method

As stated in Section 7.6, the integral over Θ_0 in Equation (7.28) was performed numerically because the nonlinearity of the integrand made it impossible to perform the integration symbolically. *Mathematica* offers a wide variety of methods to perform this integration using its `NIntegrate` routine, and some of the methods, including the Global Adaptive and Local Adaptive methods, contain a large number of submethods. The Global and Local Adaptive methods were generally found to be many times faster than the other methods, including the Double Exponential Method and several versions of the Monte Carlo Method. However, the Local Adaptive Method still took about 50% longer than the Global Adaptive Method, and because there was a high degree of agreement between these two methods, most of the calculations were performed using the Global Adaptive Method.

This is only a very general result, because not all submethods of the Global and Local Adaptive methods work equally well. For example, the Cartesian and Multidimensional rules only work for multidimensional data, so *Mathematica* was unable to get a result using these submethods. Problems were also encountered with some of the other submethods, a few of which had computational times that rivalled the Double Exponential Method and the Monte Carlo methods. However, three of the submethods were found to produce results to within six figures of accuracy within several seconds for small numbers of Fourier coefficients (less than ten) and within several minutes for large numbers of Fourier coefficients (greater than ten), although this also depended on k. They were the Multipanel Rule, the Newton-Cotes Rule, and the Trapezoidal Rule, of which the Multipanel Rule was usually the quickest. Hence, most calculations of the integral in Equation (7.28) were performed using the Global Adaptive Method with the Multipanel Rule used as the submethod. A comparison of the fastest and most reliable integration methods when $p = 3$, $q = 8$ and $k = 1.75$ is shown in Figure 7.1.

7.8 The Minimisation Method

The minimisation of Equation (7.28) was performed using *Mathematica*'s `FindMinimum` routine, which offers seven different methods of minimisation. Only four of these methods were found to give decent results, namely the Principal Axis, Conjugate Gradient, Newton, and Quasi-Newton methods. Early calculations were performed using the Principal

Axis Method. However, it was soon discovered that the Quasi-Newton Method provided just as accurate results within about a sixth of the time of the Principal Axis and Conjugate Gradient methods, and about a third of the time of the Newton Method. Many attempts were made to increase the speed of the Newton Method, because there were strong theoretical reasons for believing that the Newton Method would be faster than the Quasi-Newton Method if its Hessian matrix were to be supplied accurately. However, even after calculating the gradient and Hessian of Equation (7.28) analytically (except for the integration over Θ_0), the speed of the Newton Method was not improved, so the Quasi-Newton Method continued to be used. A comparison of the various minimisation methods $p = 3$, $q = 8$ and $k = 1.75$ is shown in Figure 7.2.

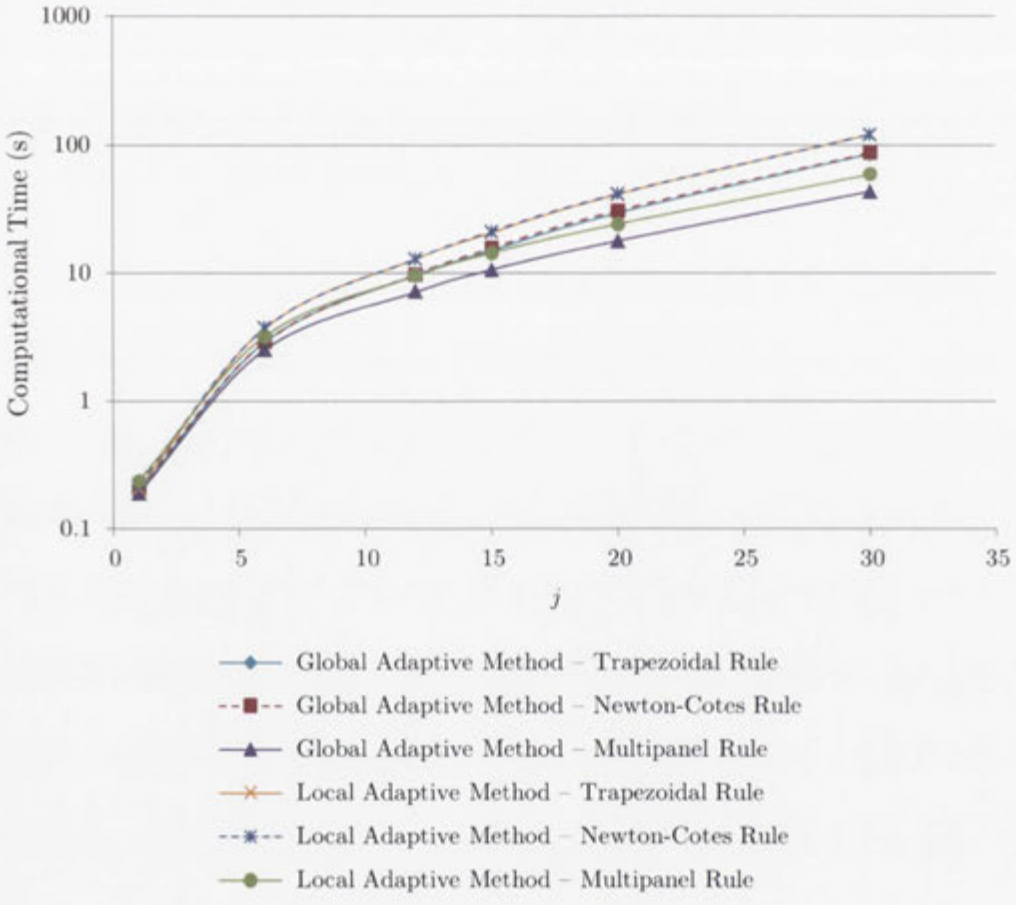

Figure 7.1: Computational times for the fastest and most reliable integration methods when $p = 3$, $q = 8$ and $k = 1.75$. These times are inclusive of the time taken to complete a minimisation routine that was held fixed while varying the integration method. The speed of the algorithm was significantly improved after these calculations were made.

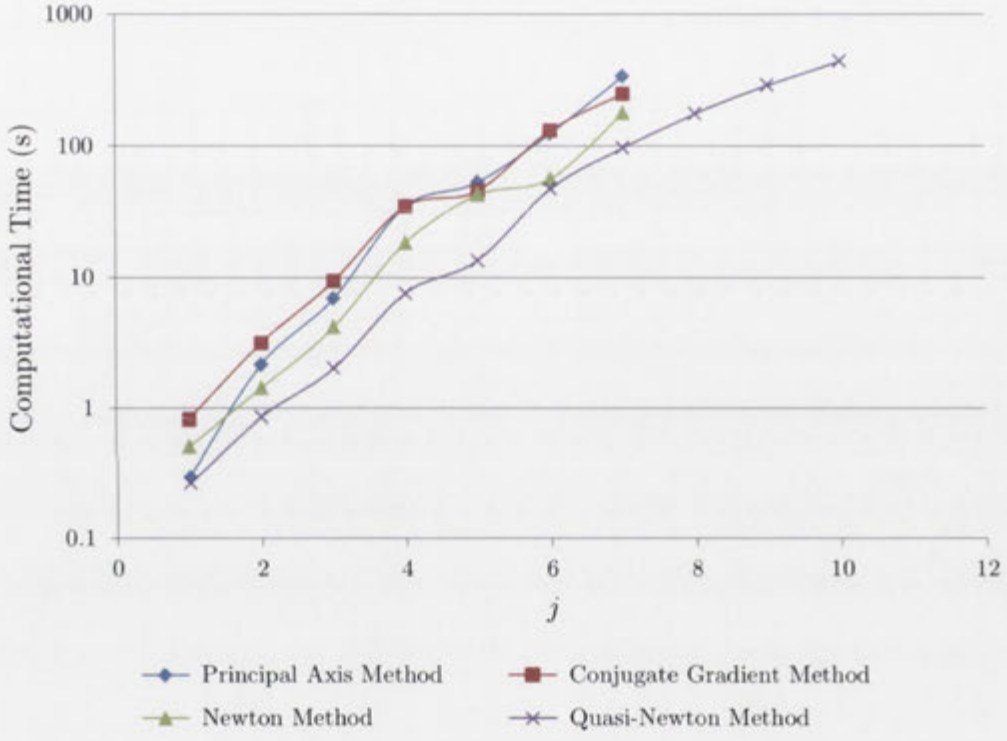

Figure 7.2: Computational times for various minimisation methods when $p = 3$, $q = 8$ and $k = 1.75$. These times are inclusive of the time taken to complete an integration routine that was held fixed while varying the minimisation method. The speed of the algorithm was significantly improved after these calculations were made.

Chapter 8

Results and Conclusions

This chapter begins with a discussion of test case selection for the reconciliation between QFMin and ghost tori, before discussing the results of the numerical implementation of the discrete-time variational principle. Diagrams have been provided in order to show the convergence of the Fourier coefficients for different values of ι, as well as to show the apparent breakdown of the reconciliation $\theta(\Theta_n)$ for large k values. The reconciled QFMin-ghost curves have also been plotted in (Θ, J)-space, along with the action-minimax and action-minimising orbits. Finally, Greene's residue criterion is introduced, and the amplitudes of the differences between the reconciled QFMin-ghost curves C^+ and C^- are shown to be consistent with Greene's residue criterion and the existence of KAM tori within the standard map for $k < 0.971635\ldots$.

8.1 Selection of the Test Cases

In order to select the test cases that will provide the broadest set of results, it is necessary to understand the significance of some results pertaining to the breakup of KAM curves as k is increased. According to KAM theory, some of the invariant tori with irrational rotational transform survive the perturbation away from integrability (where $k = 0$), although the number of these invariant tori slowly decreases as k increases. For the standard map, the last of these tori to disappear is a family of tori that have rotational transforms of the form [7]

$$\iota = n \pm \varphi, \tag{8.1}$$

where $n \in \mathbb{Z}$ and φ is the **golden mean**

$$\varphi = \frac{1 + \sqrt{5}}{2}. \tag{8.2}$$

These rotational transforms define an equivalence class of numbers called the **golden numbers**, which are a subset of another class of numbers called the **noble numbers**, whose significance is best understood by studying their continued-fraction expansions. A **continued-fraction expansion** is an expression of the form [7]

$$\omega = a_0 + \cfrac{1}{a_1 + \cfrac{1}{a_2 + \cfrac{1}{a_3 + \ddots}}}, \tag{8.3}$$

where $a_i \in \mathbb{Z}$. If $\omega \in \mathbb{Q}$, then the sequence terminates at a_n for some n, meaning that $a_i = 0$ for all $i > n$ and the continued-fraction expansion has the form [7]

$$\omega = \frac{p}{q} = a_0 + \cfrac{1}{a_1 + \cfrac{1}{a_2 + \ddots + \cfrac{1}{a_n}}}. \tag{8.4}$$

However, if $\omega \notin \mathbb{Q}$, then the sequence does not terminate, but ω can still be approximated by truncating the sequence at a_i for some $i \in \mathbb{Z}$. Then

$$\omega_i = \frac{p_i}{q_i} = a_0 + \cfrac{1}{a_1 + \cfrac{1}{a_2 + \ddots + \cfrac{1}{a_i}}}, \tag{8.5}$$

where ω_i is called the ***i*th convergent** of ω [7]. By definition,

$$\lim_{i \to \infty} \omega_i = \omega \tag{8.6}$$

for any sequence of ith convergents of ω. The continued-fraction expansions of ω are also its **best approximants** [7], meaning that if p/q is a convergent of ω, then

$$\left| \omega - \frac{p}{q} \right| < \left| \omega - \frac{p'}{q'} \right| \quad \forall p', q' \in \mathbb{Z} \text{ such that } q' \leq q. \tag{8.7}$$

Some irrationals are easier to approximate than others. For example, if a_i is large, then $1/a_i$ is small, meaning that the ith term makes little difference to the approximation and the $(i-1)$th convergent is extremely accurate for its order of approximation to the irrational [7]. Similarly, if a_i is small, then $1/a_i$ is large, so adding this term makes a considerable difference to the accuracy of the approximation [7]. The noble numbers are the most difficult numbers to approximate using continued-fraction expansions (and any other kind of expansion), because they have the property that $|a_i| = 1$ for all $i \geq j$ for some j [7]. The golden mean is the noblest and most irrational of numbers [7,38], having the continued-fraction expansion

$$\varphi = 1 + \cfrac{1}{1 + \cfrac{1}{1 + \cfrac{1}{1 + \ddots}}}. \tag{8.8}$$

The more irrational a number is, the more difficult it is to approximate using continued-fraction convergents, and the greater the size of the perturbation that is required to get the KAM curve with the corresponding rotational transform to break up. Hence, KAM curves with rotational transforms corresponding to golden numbers require the largest perturbation to break up, whereas those with rotational transforms corresponding to a rational number require the smallest (which, in this case, is infinitesimal). When selecting the test cases for the reconciliation between QFMin and ghost tori, it is important to use rotational transforms that are the continued-fraction convergents of a golden number.

This is because the golden numbers are the most irrational of numbers, being equivalent to the golden mean, so their continued-fraction expansions require a greater number of convergents than all other numbers to be within the same distance δ of the irrational they are approximating. This places an upper bound on the number of convergents required to get the Fourier series to converge to a particular accuracy for a certain k value, so if we can achieve convergence in this instance, then we can guarantee the convergence of all other rotational transforms to that same accuracy for that same k value provided that they are less irrational (that is, because the continued-fraction convergents are all rational, the rotational transform is also rational and the absolute value of its denominator is less than or equal to that of the continued-fraction convergent that is being used to approximate the golden number). Because we want to be able to plot the reconciled QFMin-ghost curves alongside the standard map, we need $0 < \epsilon < 1$, so we will choose $\phi \equiv 2 - \varphi = 0.381966\ldots$ to be representative of the equivalence class of golden numbers and study reconciled QFMin-ghost curves for which the rotational transforms are the continued-fraction convergents of ϕ. The first eight continued-fraction convergents of ϕ are given by [39]

$$0, \frac{1}{2}, \frac{1}{3}, \frac{2}{5}, \frac{3}{8}, \frac{5}{13}, \frac{8}{21}, \frac{13}{34}, \tag{8.9}$$

from which it can be seen that the continued-fraction convergents of ϕ are the ratios of two sequences of **Fibonacci numbers** [39]. From this list, we have chosen

$$\frac{1}{3}, \frac{2}{5}, \frac{3}{8}, \frac{5}{13} \tag{8.10}$$

to be test cases for the reconciliation between QFMin and ghost tori, so if we can obtain convergence to a particular accuracy and k value for $\epsilon = p/q$, where p and q are mutually prime integers and $q = 3$, 5, 8 or 13, then we must also be able to obtain convergence to that same accuracy and k value for all other $\epsilon = p/q$, where p and q are mutually prime integers and $q \leq 3$, 5, 8 or 13, respectively.

8.2 Convergence of the Objective Function

The first set of results concerns the convergence of the Fourier coefficients y_m obtained by minimising Equation (7.28) subject to Equations (7.13) and (7.35) for the rational rotational transform convergents of ϕ listed in Sequence 8.10. The minima of Equation (7.28) are shown in Figure 8.1, which can be used to determine the accuracy of the rest of the results contained in this thesis. The computed values of the Fourier coefficients are shown in Figures 8.2–8.9. Because the threshold required for convergence is completely arbitrary, the values of the Fourier coefficients were plotted as a line plot of the power spectra for various values of k. As discussed in Section 7.4, the resonant terms have been omitted. Diagrams of both the absolute and the relative values of the Fourier coefficients with respect to the first coefficient have been plotted to facilitate comparisons between the coefficients without losing information about the first coefficient. The lines interpolated between the Fourier coefficients are provided only as a visual aid. Some of the y_1 values were compared with those obtained from the first-order perturbation theory described in Section 6.9, and found to agree with it up to two or three significant figures.

When determining the accuracy of the Fourier coefficients, it is important to distinguish between the accuracy and the accuracy goal. The **accuracy** is a measure of the magnitudes of the Fourier coefficients that we obtain *after* the numerical optimisation,

whereas the **accuracy goal** is the number of digits of accuracy we specify *before* the numerical optimisation. This is important because although the accuracy goal was always set to either 8 or 9, the computational resources used to compute the Fourier coefficients weren't capable of determining their values to within an accuracy of less than 10^{-8}, so stating the accuracy goal of the Fourier coefficients is not meaningful (and often misleading) when they don't converge to the requested accuracy. This is particularly important when interpreting the results of the $\iota = 1/3$ case, because the accuracy goal was set to 9 rather than 8.

For a given accuracy, we seek the Fourier series truncation mode number for each k and ι. The **truncation mode number** is the maximum mode number beyond which the Fourier terms have contribution less than a particular accuracy, defined in terms of $|y_m|$ rather than $|y_m/y_1|$. We define such solutions to be **converged** to a particular accuracy, with that accuracy being slightly greater than the maximum absolute value that we can assert for all y_m with m greater than the Fourier truncation mode number. For example, in Figure 8.2, the $k = 0.2$ solution converges to an accuracy of 10^{-8}, and the Fourier truncation mode number is 7. Similarly, in Figure 8.6, the $k = 0.8$ solution converges to an accuracy of 10^{-7}, and the Fourier truncation mode number is 21. However, care must be taken when computing the truncation mode number, as the Fourier coefficients y_m do not always decrease monotonically with increasing m. Hence, we cannot say that in Figure 8.8, the $k = 0.4$ solution has a Fourier truncation mode number of 15, because the absolute value of y_{16} is greater than the absolute value of y_{15}. The full list of truncation mode numbers that were used to derive the plots in Sections 8.3–8.7 (Figures 8.11–8.35) are shown in Table 8.1.

As long as k was sufficiently small, none of the lines in any of the power spectra overlapped for $|y_m|$ greater than the convergence accuracy. This was expected because the nonlinearity of the map increases with increasing k, thereby increasing the truncation mode number. The convergence generally required a greater truncation mode number for each particular k value as ι was increased to higher orders of approximation to ϕ, whereas the absolute value of the first Fourier coefficient increased as k increased for the same value of ι. This suggests that the reconciled QFMin-ghost curves corresponding to rotational transforms with lower orders of approximation to ϕ and lower k values converge to a given accuracy for lower truncation mode numbers than the reconciled QFMin-ghost curves corresponding to rotational transforms with higher orders of approximation to ϕ and higher k values, which agrees with theory.

For $\iota = 1/3$, the Fourier series converges to an accuracy of at least 10^{-6} for all $k \leq 1.4$. This is ideal for practical purposes, because k usually stays well below the critical value $k_c = 0.971635\ldots$ at which the last KAM curves (with $\iota = n \pm \varphi$ for some $n \in \mathbb{Z}$) break up. It also means that for all dynamical systems with rational rotational transform $\iota = p/q$ (where p and q are mutually prime integers) that are not totally chaotic, QFMin and ghost curves are equivalent as long as $q \leq 3$. A similar result can also be drawn from the data for $\iota = 2/5$, for which there is convergence to an accuracy of at least 10^{-6} for all $k \leq 1.2$, and for $\iota = 3/8$ and $\iota = 5/13$, for which there is convergence to an accuracy of at least 10^{-6} for all $k \leq 1.0$. Hence, we know that for all $\iota = p/q$ with p and q mutually prime integers, QFMin and ghost tori are equivalent to an accuracy of at least 10^{-6} up to at least $k = 1.0$ if $q \leq 13$, at least $k = 1.2$ if $q \leq 5$, and at least $k = 1.4$ if $q \leq 3$. If convergence to an accuracy of only 10^{-5} is required, a similar set of results can be obtained by reading them off the plots.

	$\epsilon = 1/3$	$\epsilon = 2/5$	$\epsilon = 3/8$	$\epsilon = 5/13$
$k = 0.2$	7	6	6	6
$k = 0.4$	10	9	7	9
$k = 0.6$	13	13	13	12
$k = 0.8$	16	18	21	21
$k = 1.0$	22	33	45	47
$k = 1.2$	25	48	45	47
$k = 1.4$	25	48	45	-
$k = 1.6$	25	48	-	-
$k = 1.8$	26	-	-	-
$k = 2.0$	26	-	-	-
$k = 2.2$	26	-	-	-

Table 8.1: Fourier series truncation mode numbers used to derive Figures 8.11–8.35.

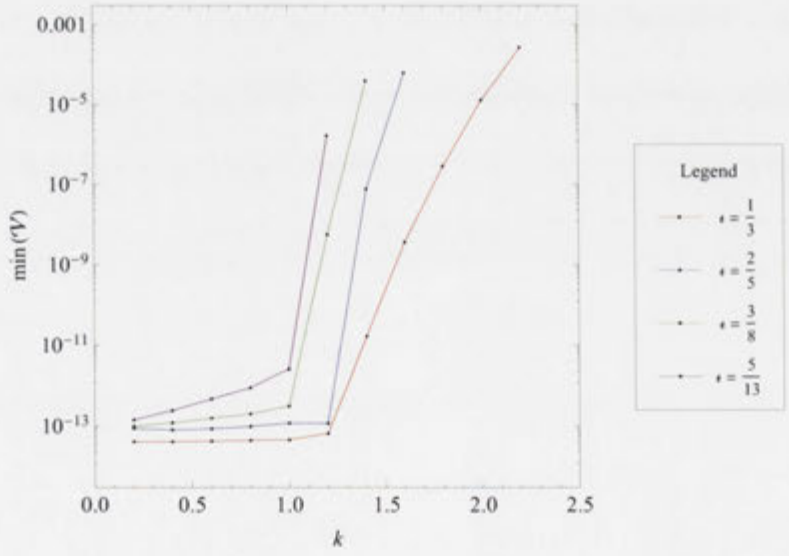

Figure 8.1: Line plot of the minimum of $\mathcal{V}$ (Equation (7.28)) for various values of k and ϵ. In the $\epsilon = 1/3$ case, $j = 27$ and the accuracy goal is 9, whereas in the $\epsilon = 2/5$ case, $j = 50$ and the accuracy goal is 8. Similarly, in the $\epsilon = 3/8$ case, $j = 48$ and the accuracy goal is 8, whereas in the $\epsilon = 5/13$ case, $j = 52$ and the accuracy goal is 8.

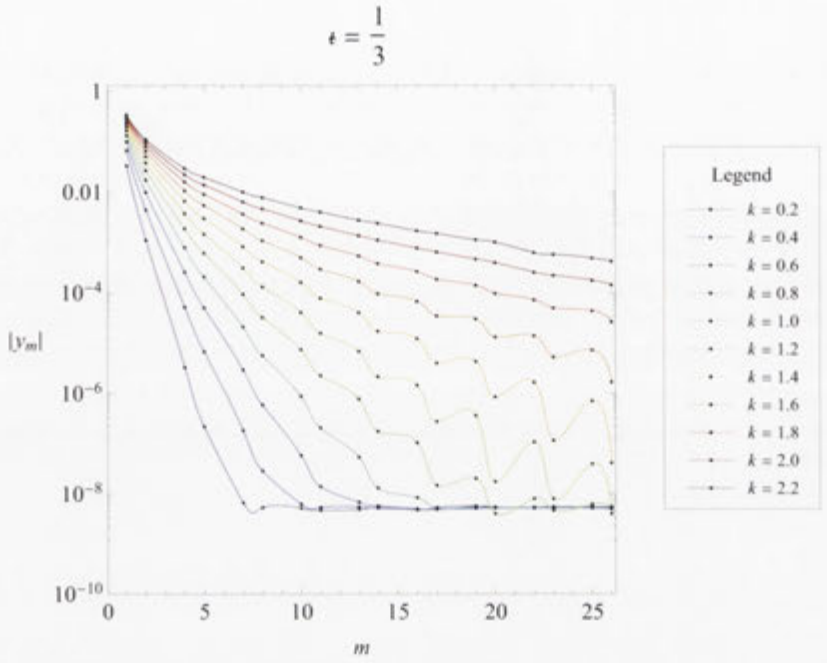

Figure 8.2: Line plot of the absolute power spectrum for $\epsilon = 1/3$ when $j = 27$ and the accuracy goal is 9. Note that the Fourier coefficients corresponding to integer multiples of q are equal to zero and have been omitted from the power spectra in accordance with the conjugacy constraint defined in Section 7.4.

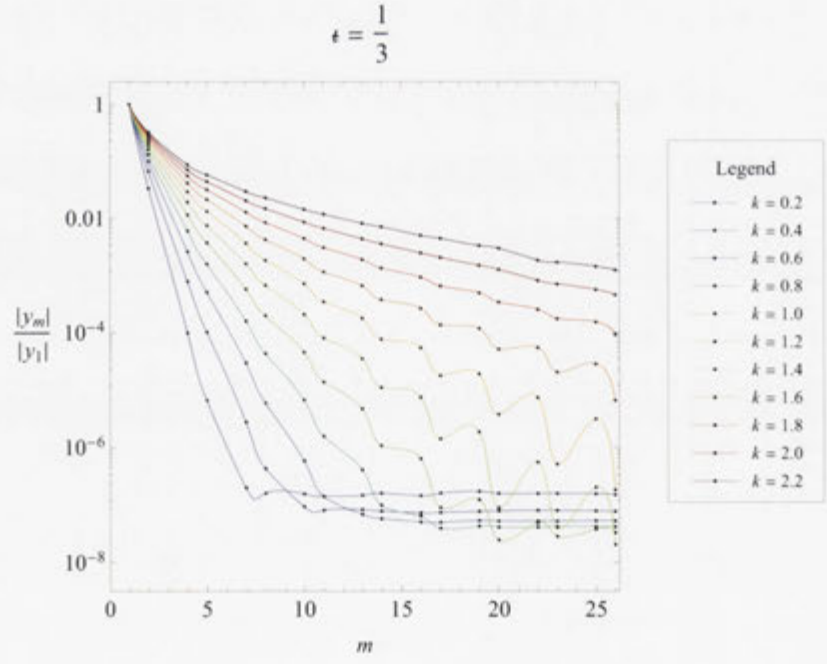

Figure 8.3: Line plot of the relative power spectrum for $\epsilon = 1/3$ when $j = 27$ and the accuracy goal is 9. Note that the Fourier coefficients corresponding to integer multiples of q are equal to zero and have been omitted from the power spectra in accordance with the conjugacy constraint defined in Section 7.4.

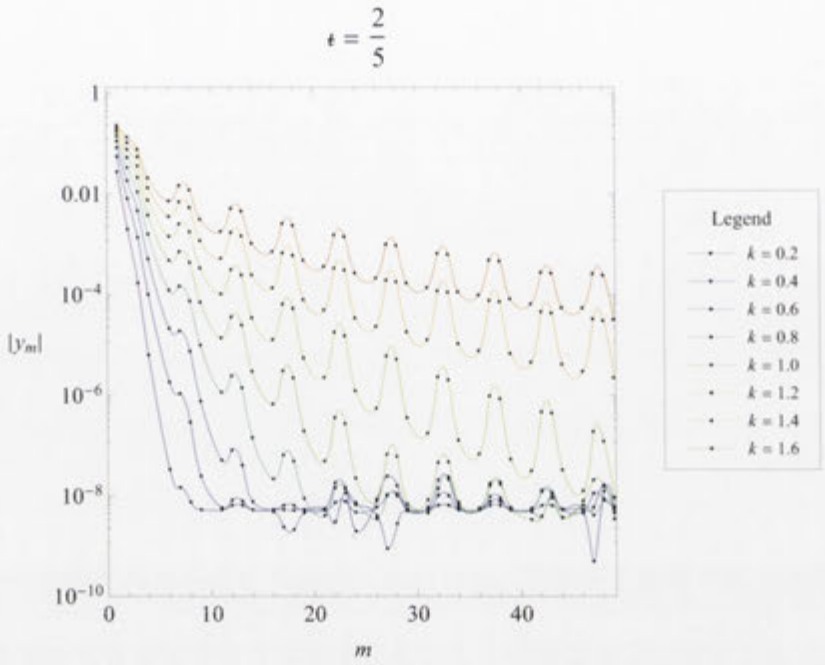

Figure 8.4: Line plot of the absolute power spectrum for $\epsilon = 2/5$ when $j = 50$ and the accuracy goal is 8. Note that the Fourier coefficients corresponding to integer multiples of q are equal to zero and have been omitted from the power spectra in accordance with the conjugacy constraint defined in Section 7.4.

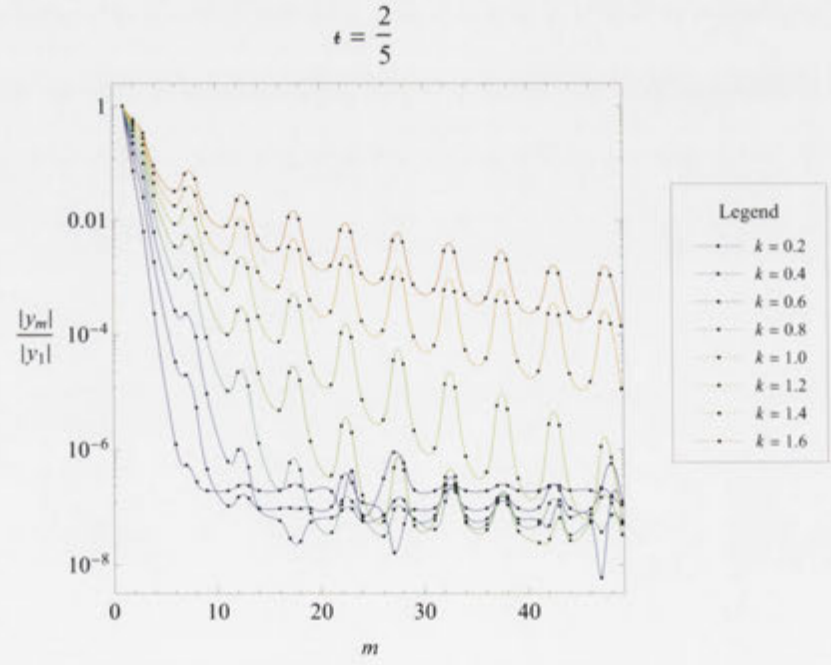

Figure 8.5: Line plot of the relative power spectrum for $\epsilon = 2/5$ when $j = 50$ and the accuracy goal is 8. Note that the Fourier coefficients corresponding to integer multiples of q are equal to zero and have been omitted from the power spectra in accordance with the conjugacy constraint defined in Section 7.4.

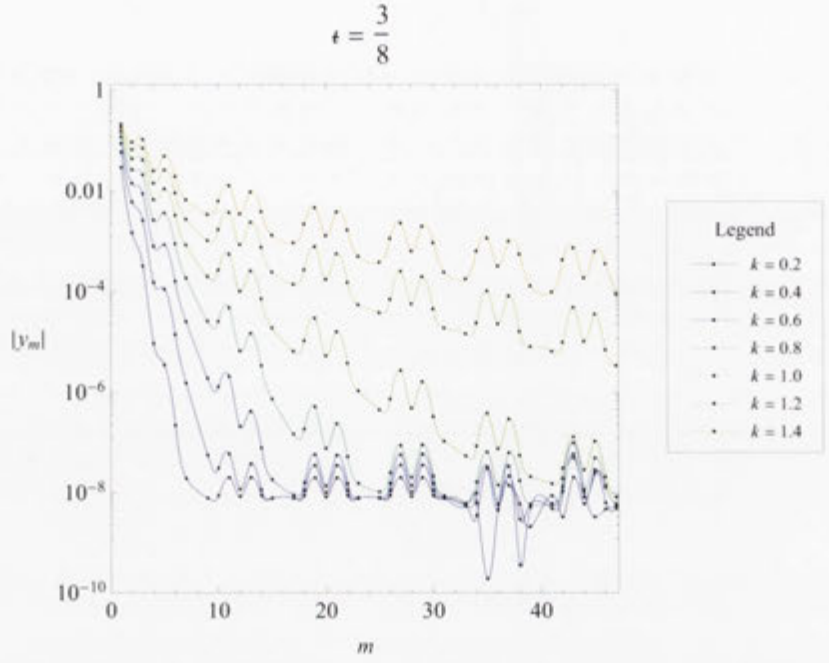

Figure 8.6: Line plot of the absolute power spectrum for $\epsilon = 3/8$ when $j = 48$ and the accuracy goal is 8. Note that the Fourier coefficients corresponding to integer multiples of q are equal to zero and have been omitted from the power spectra in accordance with the conjugacy constraint defined in Section 7.4.

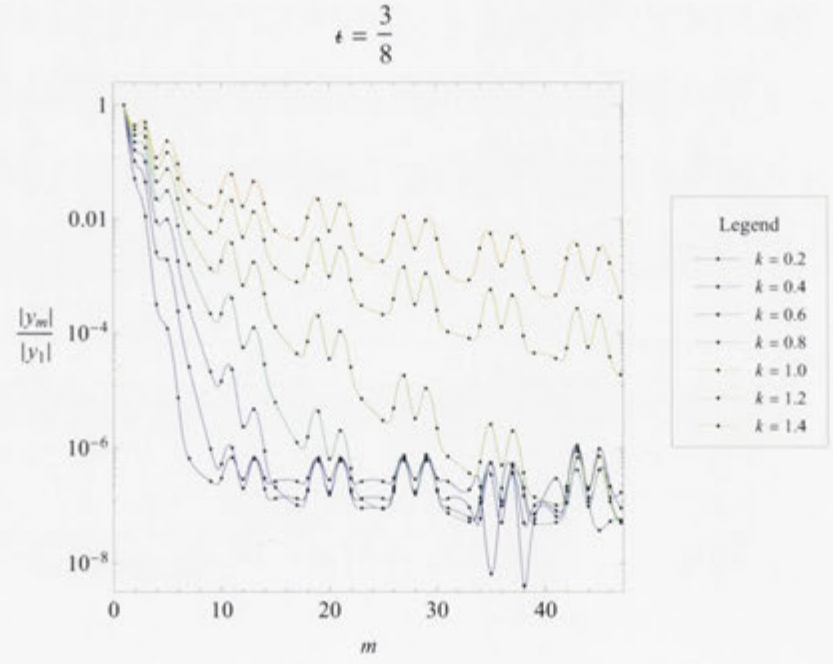

Figure 8.7: Line plot of the relative power spectrum for $\epsilon = 3/8$ when $j = 48$ and the accuracy goal is 8. Note that the Fourier coefficients corresponding to integer multiples of q are equal to zero and have been omitted from the power spectra in accordance with the conjugacy constraint defined in Section 7.4.

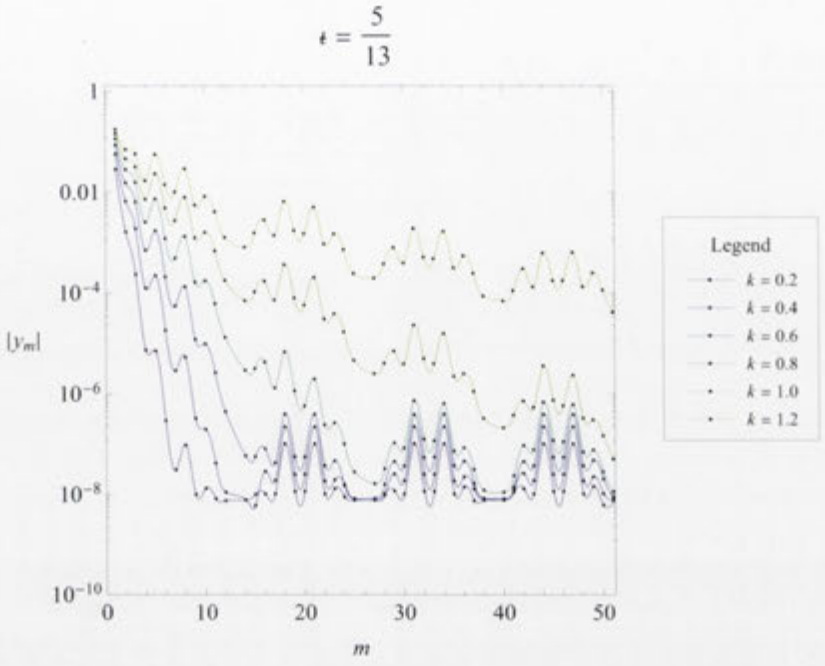

Figure 8.8: Line plot of the absolute power spectrum for $\epsilon = 5/13$ when $j = 52$ and the accuracy goal is 8. Note that the Fourier coefficients corresponding to integer multiples of q are equal to zero and have been omitted from the power spectra in accordance with the conjugacy constraint defined in Section 7.4.

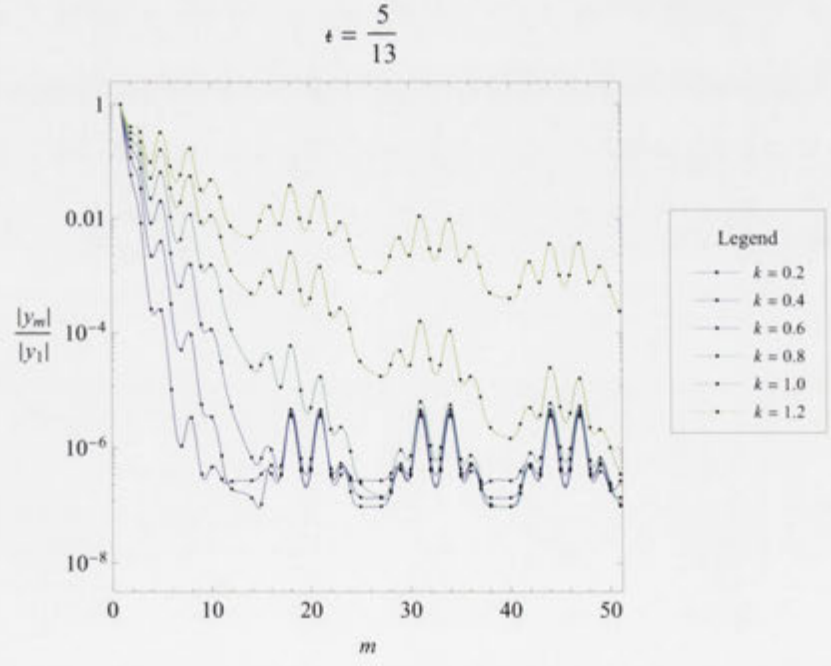

Figure 8.9: Line plot of the relative power spectrum for $\epsilon = 5/13$ when $j = 52$ and the accuracy goal is 8. Note that the Fourier coefficients corresponding to integer multiples of q are equal to zero and have been omitted from the power spectra in accordance with the conjugacy constraint defined in Section 7.4.

8.3 Monotonicity of the Transformation

Once the Fourier coefficients had been calculated, they were substituted into Equations (7.36) and (7.37) and plotted in Figures 8.11–8.18, along with Poincaré sections of their action-minimax and action-minimising orbits. This provides a vital test for determining the values of k and ϵ for which the transformation is guaranteed hold, and by extension, when the reconciliation between QFMin and ghost tori is guaranteed to hold. Because we are seeking a global coordinate transformation rather than a local one, not only do we require $\sum_{n=0}^{q-1} \theta(\Theta_n)$ to be monotone (according to Section 7.4), but we also require the transformation of the entire space $\theta(\Theta)$ to be monotone in order to avoid having a coordinate singularity when $\theta'(\Theta) = 0$. This is because the transformation cannot possibly be global if $J = \theta'(\Theta)I$ changes sign with respect to I, which suggests that the reconciliation may have broken down. However, in such cases, the reconciliation may still hold under a different coordinate transformation such as $\theta = \theta(\Theta, J)$, but this is well beyond the scope of this thesis.

When k is large, the Fourier series have much larger truncation mode numbers than when k is low. Unfortunately, this can cause the Fourier series to converge insufficiently for high k values, and because the unconverged terms can contribute substantially to $\theta'(\Theta)$, its sign can be altered, thus causing the lack of convergence of the Fourier series to mimic the breakdown of the monotonicity of $\theta(\Theta)$. The situation is further complicated by the existence of plots such as Figure 8.10, which clearly demonstrate that for $\epsilon = 3/8$ and $k = 1.6$, the first seven terms of the Fourier series have a similar convergence pattern to that of their lower-k counterparts, whereas the remaining terms of the $k = 1.6$ Fourier series follow a convergence pattern that's very different to that of its lower-k counterparts. This is illustrated by the fact that the lines corresponding to the $k = 1.6$ Fourier series overlap those of their lower-k counterparts for $10^{-4} < |y_m| < 10^{-2}$, whereas if the $k = 1.6$ Fourier series was removed, the lines corresponding to the remaining Fourier series would not overlap those of their lower- or higher-k counterparts for $|y_m| < 10^{-7}$. This suggests that the monotonicity of $\theta(\Theta)$ may well have broken down after all, but because we cannot prove this without making further calculations, we have to accept that the problem could still be due to the lack of convergence of the Fourier series.

Some of the other possible reasons for the apparent loss of monotonicity of the transformation at high k may include:

1. The boxcar filter that was used to compute the y_m versus m Fourier series may be causing Gibbs-like oscillations in the Fourier terms.

2. The sharp truncation of the Fourier series may be causing undershooting in the Fourier representation, which could also be attributed to the **Gibbs phenomenon** [40, 41] and is manifest as spikes.

3. Our failure to constrain $\theta'(\Theta)$ to be strictly positive in the numerical algorithm could be allowing *Mathematica* to overshoot in the numerical minimisation of the variational principle and obtain negative values for $\theta'(\Theta)$, even though such values would destroy monotonicity and potentially violate the graph property.

4. The particular conjugacy constraint we are using (Equation (7.31)) may be causing spurious nonmonotonicity.

The first possibility is likely because the oscillations in the Fourier series become larger with increasing k. It could be eliminated by applying a non-boxcar windowing function to

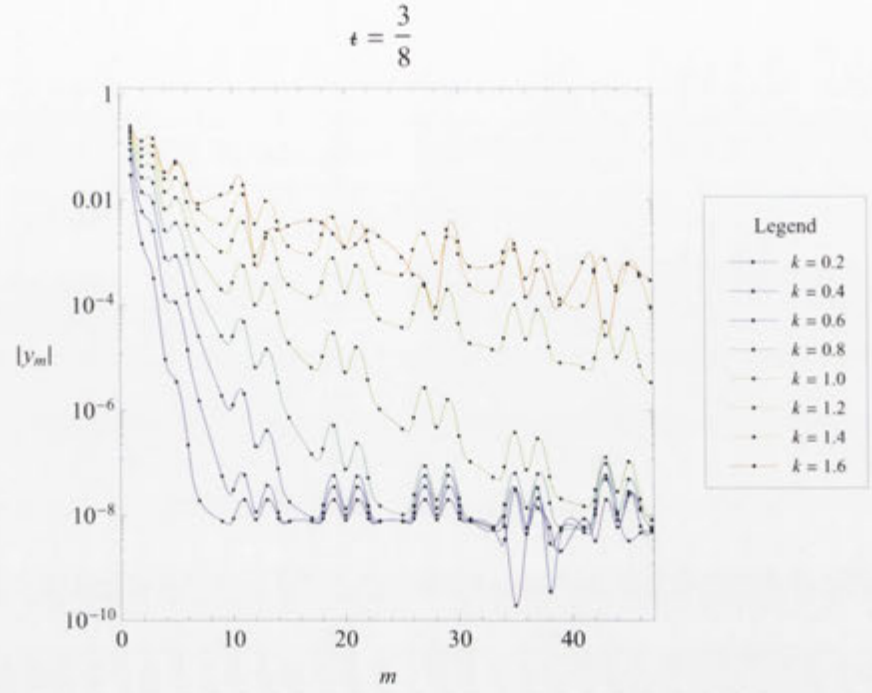

Figure 8.10: Line plot of the absolute power spectrum for $\epsilon = 3/8$ when $j = 48$ and the accuracy goal is 8, including the $k = 1.6$ terms. Note that the Fourier coefficients corresponding to integer multiples of q are equal to zero and have been omitted from the power spectra in accordance with the conjugacy constraint defined in Section 7.4.

ΔJ_n in Equation (7.35), thereby minimising the effect of ringing due to high j truncation. The second possibility is precluded by the fact that $\theta(\Theta)$ does not take the form of a step function, as would be expected if the Gibbs phenomenon were to occur. This possibility could also be eliminated by introducing a smoother truncation via a high-k roll-off filter. The third possibility is likely, and could be eliminated by constraining $\theta'(\Theta)$ to be strictly positive. The fourth possibility is also likely, and is supported by the existence of a similar observation in Dewar and Khorev [25], who implemented a different conjugacy constraint in order to resolve a problem with their own calculations. This possibility could be eliminated by finding a different conjugacy constraint and imposing it on the Fourier coefficients.

Because the monotonicity of $\theta(\Theta)$ could still potentially have broken down, the lowest k value at which this breakdown could have occurred places an upper bound on the values of k for which the reconciliation is guaranteed to hold for each value of ϵ. These upper-limit k values enable the comparison of the potential breakdown of both the coordinate transformation and the reconciliation for different values of ϵ. Assuming that the Fourier coefficients have adequately converged, and that the potential breakdown in the reconciliation is due to our particular choice of conjugacy constraint, the lowest k values at which the reconciliation breaks down can be identified as the k values at which $\theta(\Theta)$ is no longer monotonic. This lack of monotonicity can be most easily identified by inspecting crossings of its derivative $\theta'(\Theta)$ with zero. In the $\epsilon = 1/3$ case, the reconciliation potentially breaks down at around $k = 2.1$, whereas in the $\epsilon = 2/5$ case, the reconciliation potentially breaks down at around $k = 1.5$. Similarly, in the $\epsilon = 3/8$ case, the reconciliation potentially breaks down at around $k = 1.3$, whereas in the $\epsilon = 5/13$ case, the reconciliation potentially breaks down at just under $k = 1.2$. One would expect the reconciliation to break

down at increasingly lower k values as the order of the approximation to $\epsilon = \phi$ increases, and it can be seen from Figures 8.11–8.18 that this trend was followed. Another result that can be obtained from these plots is the values of Θ at which the reconciliation first appears to break down, and by extension, the values of θ. This can be achieved by inspecting the minima of $\theta'(\Theta)$ and determining the Θ values at which these minima are negative. Because these minima always occur at an action-minimax orbit, it's easy to determine the corresponding θ values by inspecting the plots of $\theta(\Theta)$. However, for the sake of brevity, these results have not been listed explicitly.

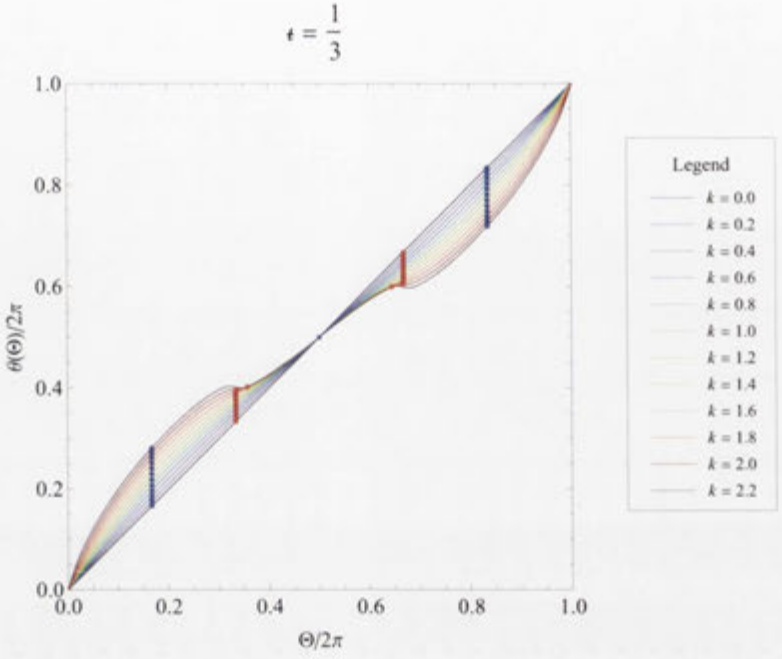

Figure 8.11: Plot of the inverse transformation $\theta(\Theta)$ for $\epsilon = 1/3$ when $j = 27$ and the accuracy goal is 9. The red dots are the action-minimax orbits, whereas the blue dots are the action-minimising orbits.

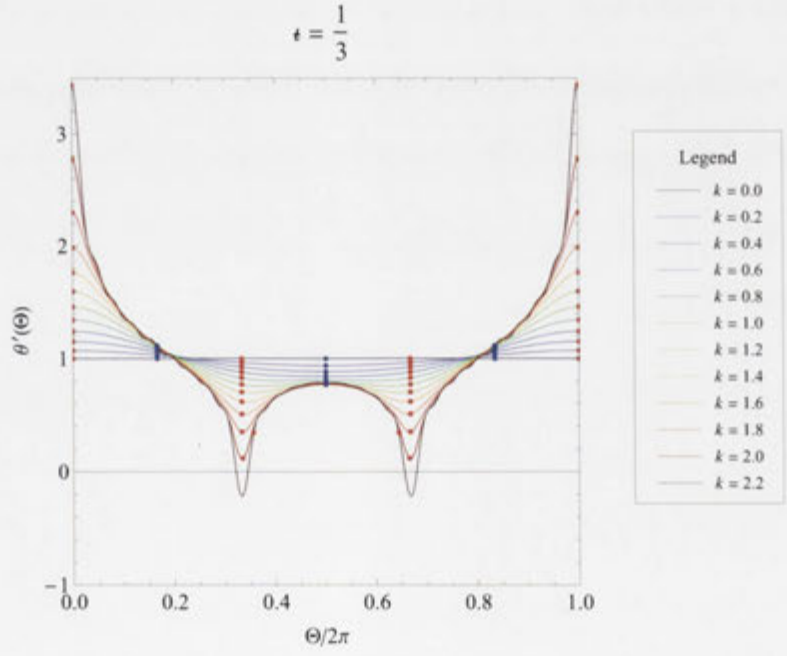

Figure 8.12: Plot of the derivative of the inverse transformation $\theta'(\Theta)$ for $\epsilon = 1/3$ when $j = 27$ and the accuracy goal is 9. The red dots are the action-minimax orbits, whereas the blue dots are the action-minimising orbits.

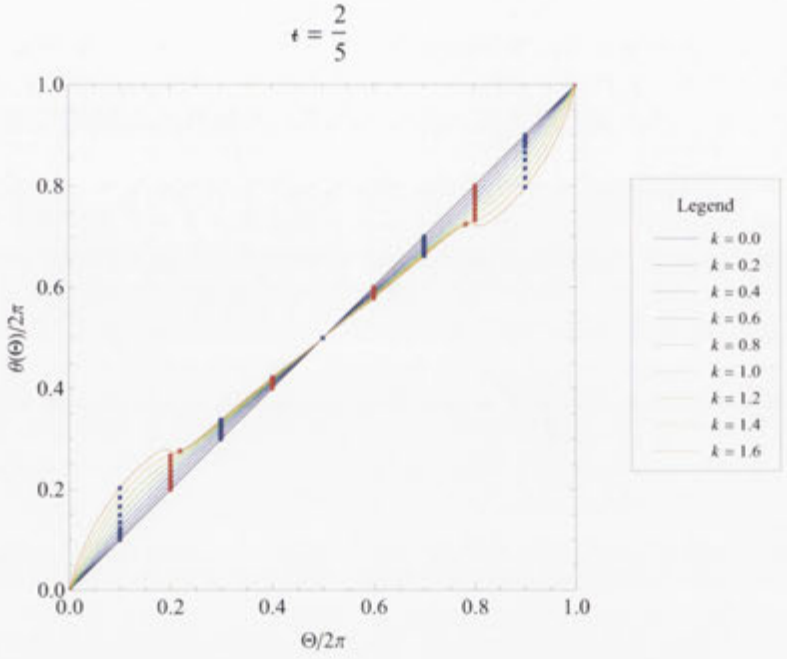

Figure 8.13: Plot of the inverse transformation $\theta(\Theta)$ for $\epsilon = 2/5$ when $j = 50$ and the accuracy goal is 8. The red dots are the action-minimax orbits, whereas the blue dots are the action-minimising orbits.

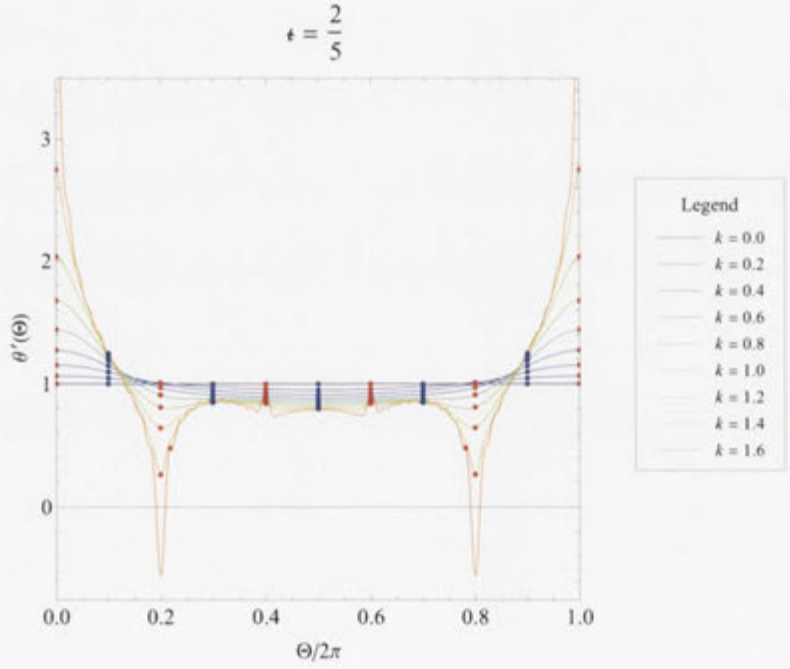

Figure 8.14: Plot of the derivative of the inverse transformation $\theta'(\Theta)$ for $\epsilon = 2/5$ when $j = 50$ and the accuracy goal is 8. The red dots are the action-minimax orbits, whereas the blue dots are the action-minimising orbits.

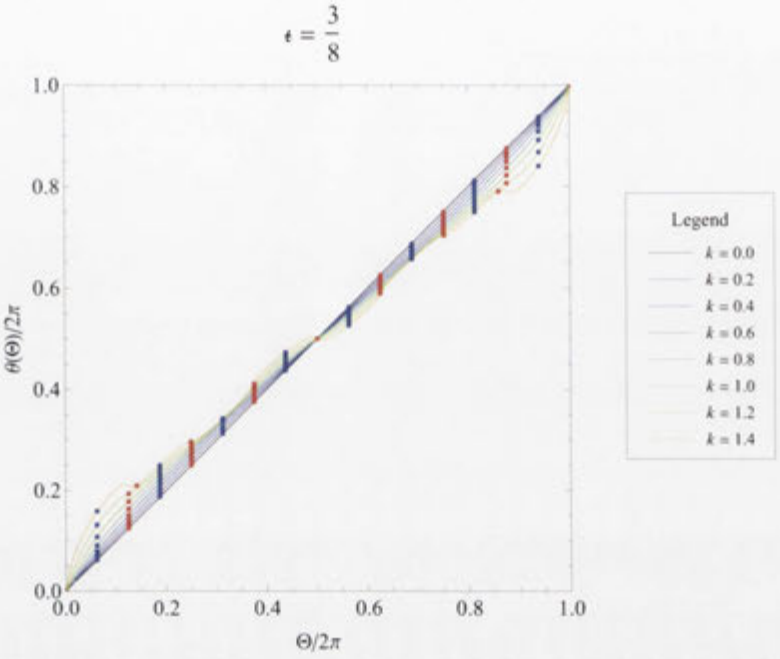

Figure 8.15: Plot of the inverse transformation $\theta(\Theta)$ for $\epsilon = 3/8$ when $j = 48$ and the accuracy goal is 8. The red dots are the action-minimax orbits, whereas the blue dots are the action-minimising orbits.

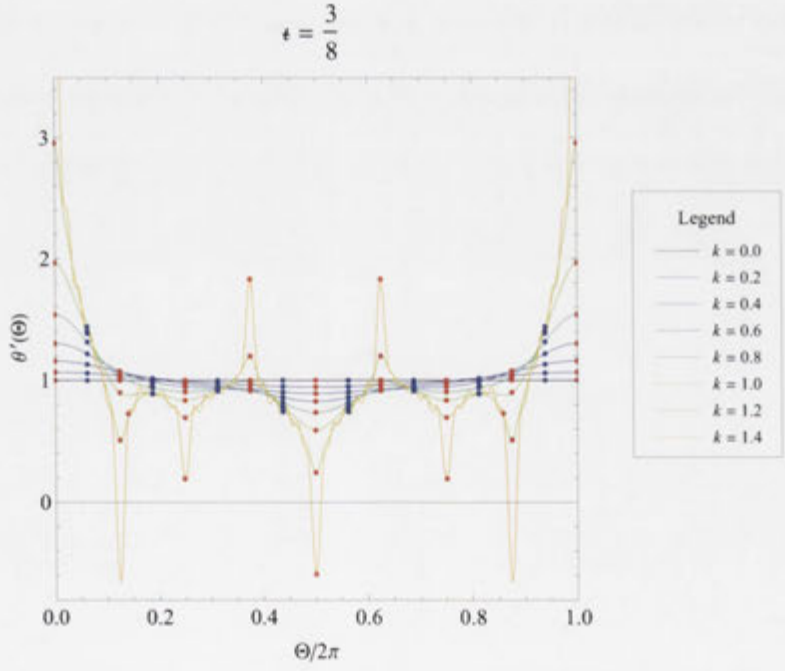

Figure 8.16: Plot of the derivative of the inverse transformation $\theta'(\Theta)$ for $\epsilon = 3/8$ when $j = 48$ and the accuracy goal is 8. The red dots are the action-minimax orbits, whereas the blue dots are the action-minimising orbits.

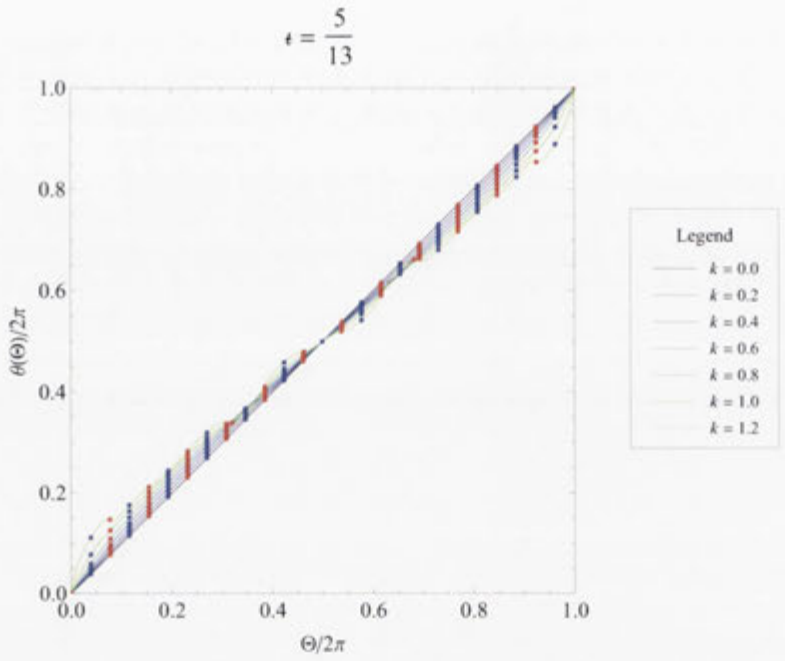

Figure 8.17: Plot of the inverse transformation $\theta(\Theta)$ for $\epsilon = 5/13$ when $j = 52$ and the accuracy goal is 8. The red dots are the action-minimax orbits, whereas the blue dots are the action-minimising orbits.

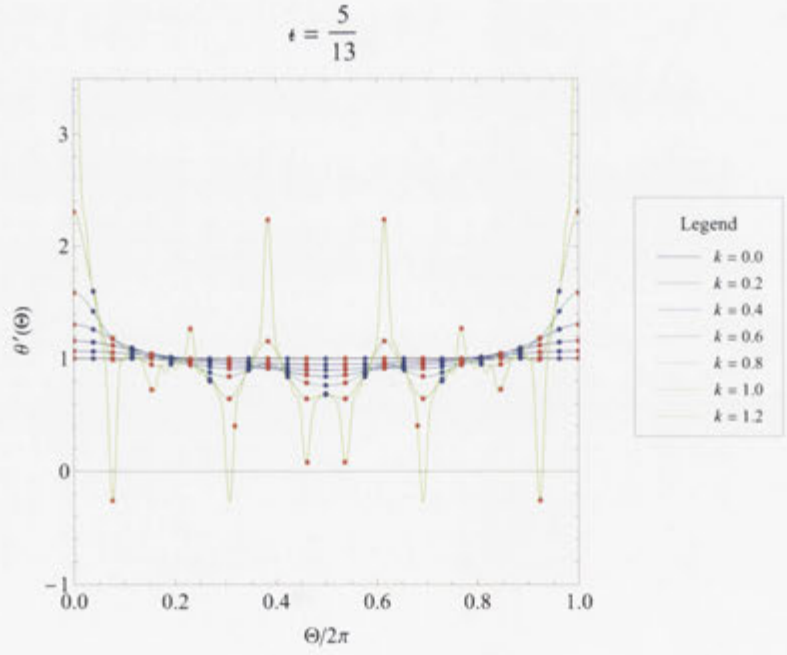

Figure 8.18: Plot of the derivative of the inverse transformation $\theta'(\Theta)$ for $\epsilon = 5/13$ when $j = 52$ and the accuracy goal is 8. The red dots are the action-minimax orbits, whereas the blue dots are the action-minimising orbits.

8.4 Poincaré Plots of the Reconciled QFMin-Ghost Tori

Once the Fourier coefficients had been used to plot $\theta(\Theta_n)$ and its derivative, they were then substituted into Equations (5.27) and (5.28) with $\theta_n = \theta(\Theta_n)$, so that the reconciled QFMin-ghost curves C^+ and C^- could be plotted in both (θ, I)-space and (Θ, I)-space for various k values. These curves have been plotted in Figures 8.19–8.26, except for those for which $\theta(\Theta)$ was shown to be nonmonotonic in Section 8.3. As shown in Section 6.2, the periodicity of J depends on Θ, so it made more sense to plot the reconciled QFMin-ghost curves in (Θ, I)-space than in (Θ, J)-space, because I has the same periodicity for all Θ. Poincaré sections of the action-minimax and action-minimising orbits have also been plotted, in order to demonstrate that the reconciled QFMin-ghost curves pass through them. This has another benefit when Θ is plotted instead of θ, in that it demonstrates that Θ_n really does have the expected form of $\Theta_n = \Theta_0 + \iota t_n$, where $t_n = 2\pi n$, because the plots satisfy the implication that Θ_n is $2\pi\iota$-periodic for rational rotational transforms $\iota = p/q$, where p and q are mutually prime integers. Each plot of the action-minimax and action-minimising orbits is separated from the other plots of the same orbit by integer multiples of $\Theta/2\pi = 1/q$, with $\Theta_0/2\pi$, the offset from the vertical axis, being an integer multiple of $1/q$ in the action-minimax case and an odd integer multiple of $1/2q$ in the action-minimising case. For example, in the $\iota = 1/3$ case, shown in Figure 8.20, the action-minimax orbits are separated by integer multiples of $\Theta/2\pi = 1/3$ and offset from the vertical axis by an integer multiple of $1/3$, whereas the action-minimising orbits are separated by integer multiples of $\Theta/2\pi = 1/3$ and offset from the vertical axis by an odd integer multiple of $1/6$. Curiously, in the $\iota = 1/3$ case, the action-minimax orbits at $\Theta/2\pi = 1/3$ and $\Theta/2\pi = 2/3$ are slightly askew when $k = 2.0$. This is due to the Fourier series failing to converge to within five or six decimal places within the specified number of Fourier terms.

It should be noted that because QFMin and ghost curves are automatically reconciled in the $k = 0$ case, these same principles apply to the $k = 0$ curve when plotted in (θ, I)-space (recall that $k = 0$ implies that $C^+ = C^-$). In fact, it is the intrinsic reconciliation between QFMin and ghost curves for $k = 0$ that makes it convenient to calculate the action-minimax and action-minimising orbits in (θ, I)-space by using the continuation method. The action-minimax and action-minimising orbits are given initial values of $\theta_n = \theta_0 + 2\pi n\iota$, where $\theta_0 = 0$ (or an integer multiple of $2\pi/q$) in the action-minimax case and $\theta_0 = \pi/q$ (or an odd integer multiple of π/q) in the action-minimising case. We have gradually increased k from $k = 0$, and found the action-minimax and action-minimising orbits for each value of k, for which the periodic orbits intersect the QFMin and ghost curves. In contrast, if the initial guess for k is sufficiently large, then the QFMin and ghost curves may not intersect the periodic orbits.

Unfortunately, there appears to be either a numerical error or a bifurcation phenomenon in the $\iota = 5/13$ case, which causes the action-minimax and action-minimising orbits to be plotted in the wrong locations when $\theta_n = 2\pi n\iota$ and $\theta_n = 2\pi n\iota + \pi/q$ are used as the respective initial conditions. It was found that in the action-minimax case, the correct orbit was obtained by summing n from 0 to $q - 1$ instead of from 1 to q, which had been used for the other rotational transforms. Because the periodicity of θ implies that both initial conditions are equivalent, it was possible to make this change in the summation indices without adversely affecting the results. On the other hand, the action-minimising orbits remained sensitive to the initial conditions even after changing the summation in-

dices, but only for $k < 0.6$. Regrettably, the cause of these inconsistencies has not been identified yet.

One of the most interesting observations concerning the Poincaré plots of the reconciled QFMin-ghost curves in (θ, I)-space is the apparent violation of the graph property for high k. This is due to the apparent breakdown in the monotonicity of $\theta(\Theta)$, and corresponds to the same θ values as does the breakdown in the monotonicity of $\theta(\Theta)$ obtained from Figures 8.11–8.18. Because violation of the graph property implies breakdown in the monotonicity of $\theta(\Theta)$, it is believed that if the reason for the apparent breakdown in the monotonicity of $\theta(\Theta)$ is primarily numerical, and not analytical, then this apparent violation of the graph property will be eliminated as a better numerical algorithm is obtained. However, if the reason for the apparent breakdown in the monotonicity of $\theta(\Theta)$ is primarily analytical, and not numerical, then this violation of the graph property is real and represents a fundamental limitation of the particular conjugacy constraint we have chosen. Hence, it is best to be cautious when interpreting the results for high k.

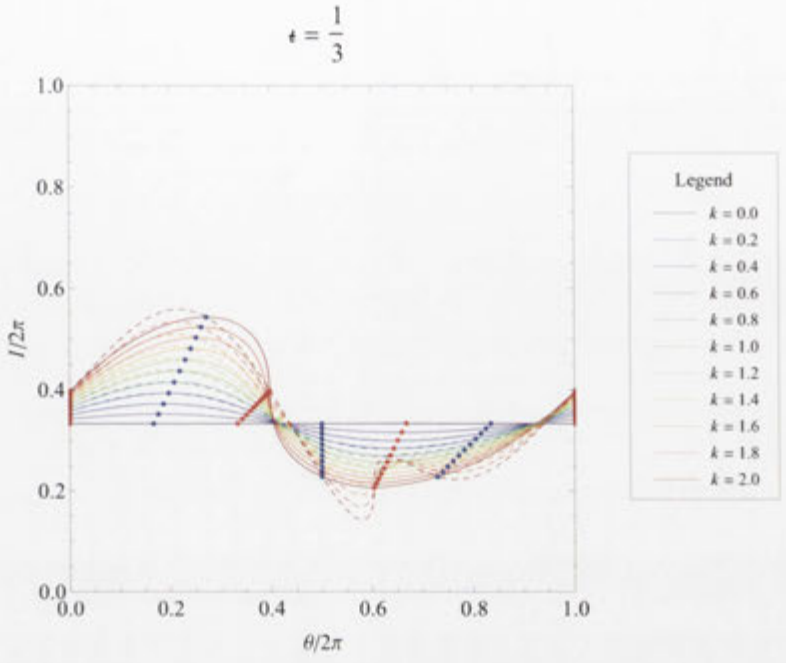

Figure 8.19: Plot of the reconciled QFMin-ghost curves in (θ, I)-space for $\epsilon = 1/3$ when $j = 27$ and the accuracy goal is 9. The solid lines are the C^+ curves and the dashed lines are the C^- curves, whereas the red dots are the action-minimax orbits and the blue dots are the action-minimising orbits.

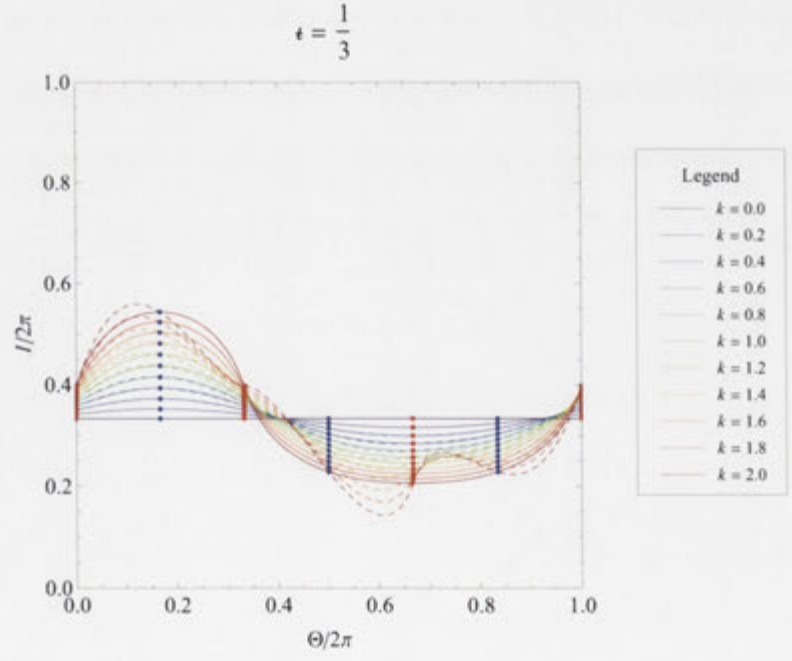

Figure 8.20: Plot of the reconciled QFMin-ghost curves in (Θ, I)-space for $\epsilon = 1/3$ when $j = 27$ and the accuracy goal is 9. The solid lines are the C^+ curves and the dashed lines are the C^- curves, whereas the red dots are the action-minimax orbits and the blue dots are the action-minimising orbits.

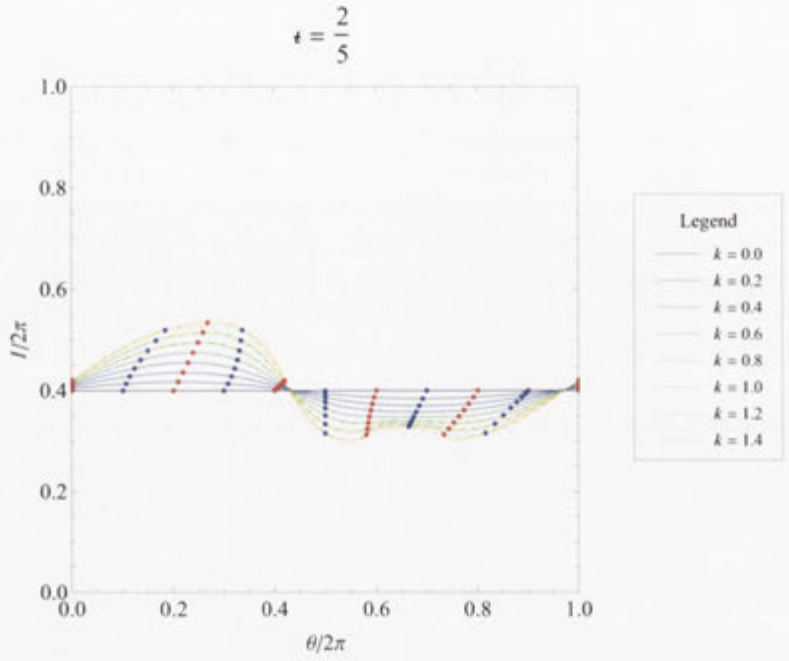

Figure 8.21: Plot of the reconciled QFMin-ghost curves in (θ, I)-space for $\epsilon = 2/5$ when $j = 50$ and the accuracy goal is 8. The solid lines are the C^+ curves and the dashed lines are the C^- curves, whereas the red dots are the action-minimax orbits and the blue dots are the action-minimising orbits.

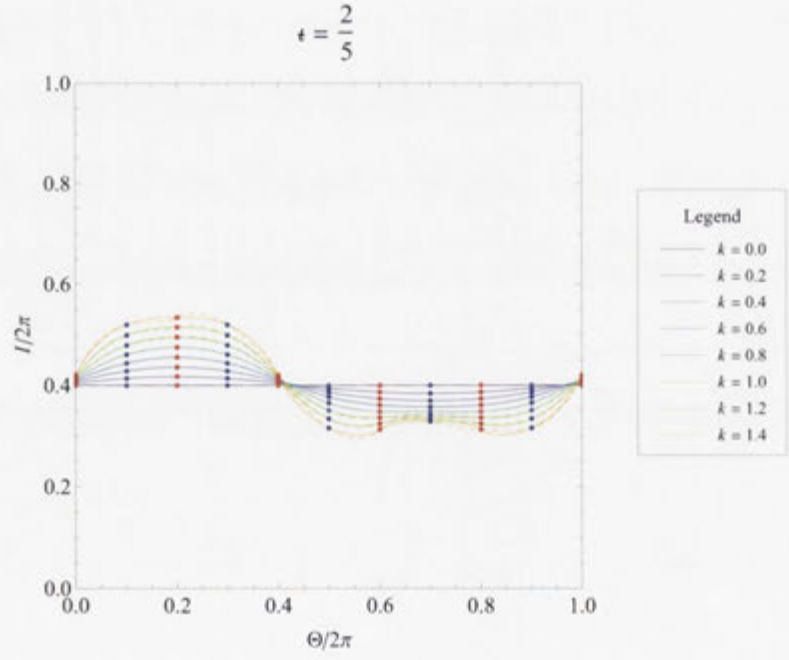

Figure 8.22: Plot of the reconciled QFMin-ghost curves in (Θ, I)-space for $\epsilon = 2/5$ when $j = 50$ and the accuracy goal is 8. The solid lines are the C^+ curves and the dashed lines are the C^- curves, whereas the red dots are the action-minimax orbits and the blue dots are the action-minimising orbits.

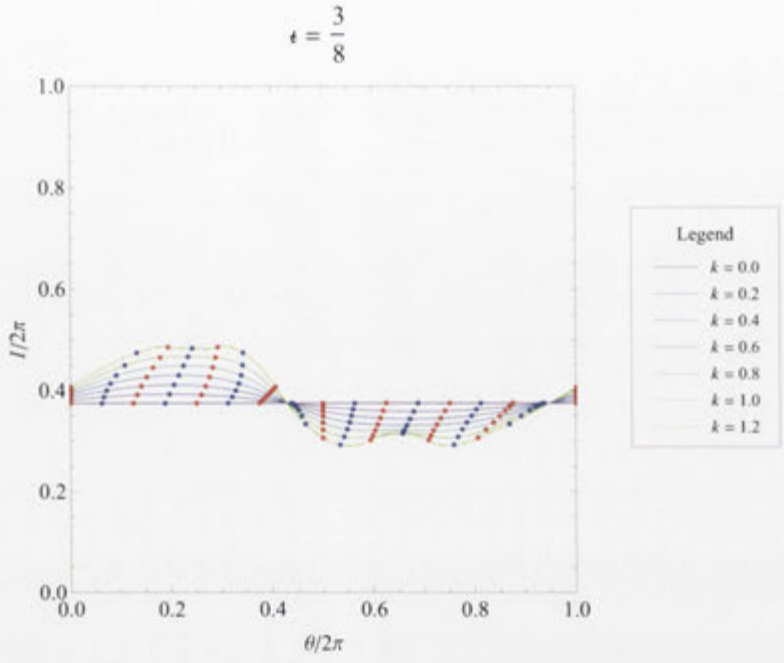

Figure 8.23: Plot of the reconciled QFMin-ghost curves in (θ, I)-space for $\epsilon = 3/8$ when $j = 48$ and the accuracy goal is 8. The solid lines are the C^+ curves and the dashed lines are the C^- curves, whereas the red dots are the action-minimax orbits and the blue dots are the action-minimising orbits.

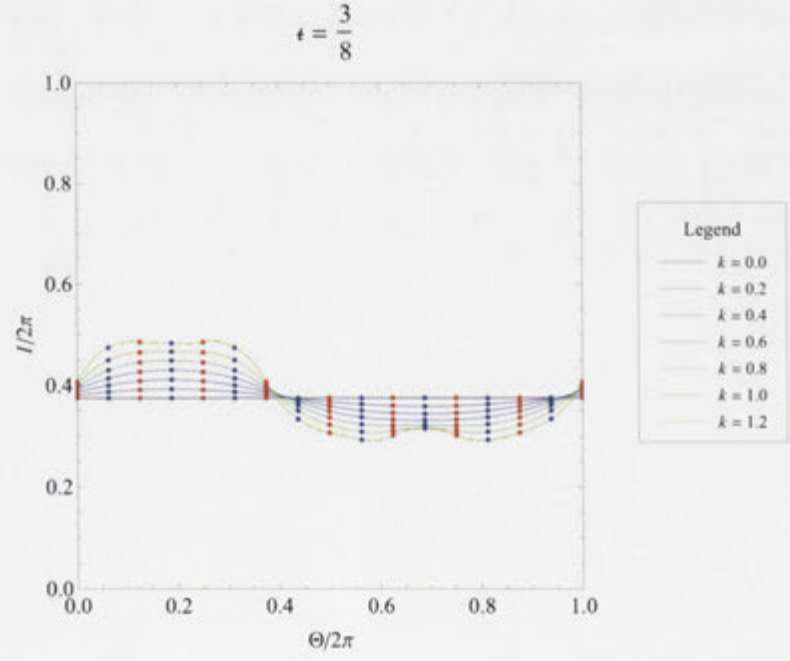

Figure 8.24: Plot of the reconciled QFMin-ghost curves in (Θ, I)-space for $\epsilon = 3/8$ when $j = 48$ and the accuracy goal is 8. The solid lines are the C^+ curves and the dashed lines are the C^- curves, whereas the red dots are the action-minimax orbits and the blue dots are the action-minimising orbits.

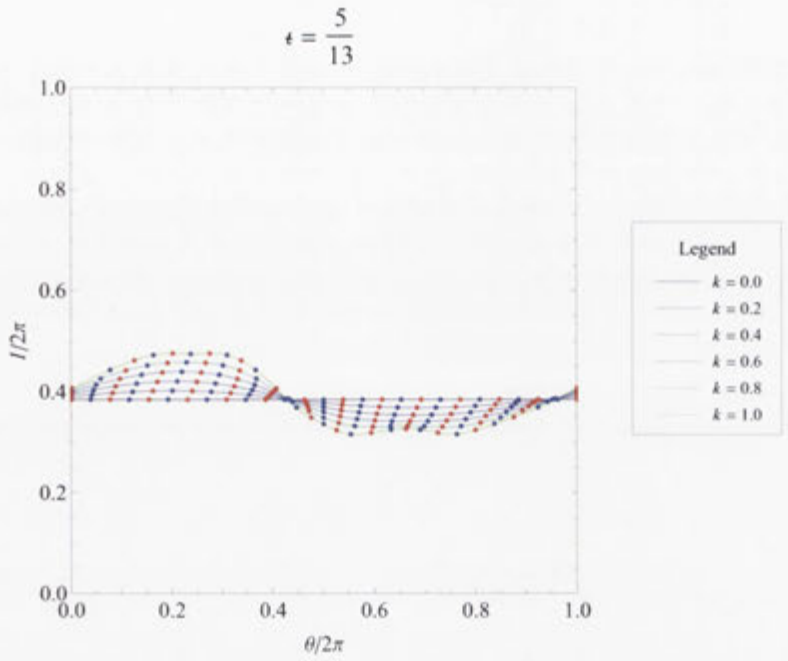

Figure 8.25: Plot of the reconciled QFMin-ghost curves in (θ, I)-space for $\epsilon = 5/13$ when $j = 52$ and the accuracy goal is 8. The solid lines are the C^+ curves and the dashed lines are the C^- curves, whereas the red dots are the action-minimax orbits and the blue dots are the action-minimising orbits.

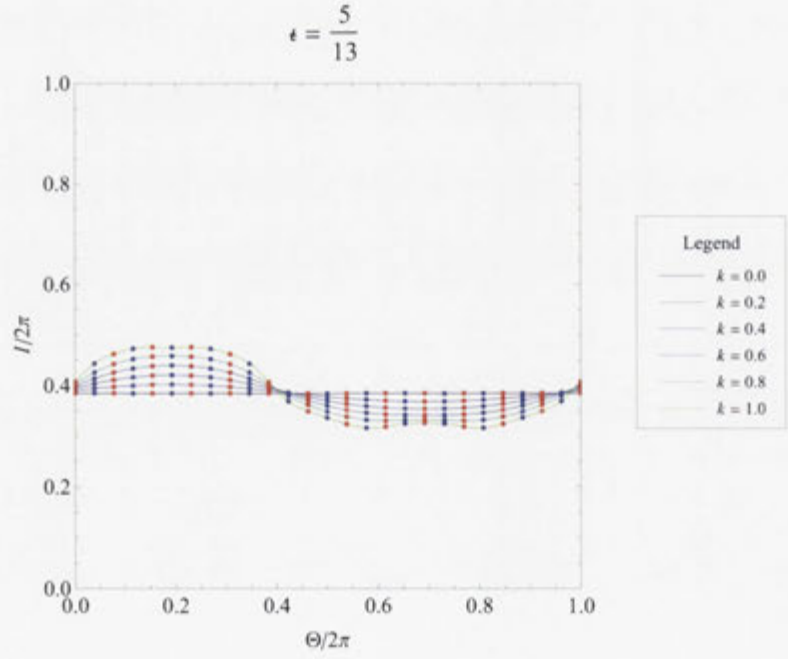

Figure 8.26: Plot of the reconciled QFMin-ghost curves in (Θ, I)-space for $\epsilon = 5/13$ when $j = 52$ and the accuracy goal is 8. The solid lines are the C^+ curves and the dashed lines are the C^- curves, whereas the red dots are the action-minimax orbits and the blue dots are the action-minimising orbits.

8.5 Linear Stability of the Orbits

In order to understand the significance of the final result of this thesis, it is necessary to introduce the concept of a "residue" by studying the linear stability of the orbits within a small neighbourhood of a periodic orbit. Although most of these orbits have irrational rotational transform, the essential information about their stability is still retained via the linear approximation [7]

$$\delta\mathbf{x}_{n+1} = M(\mathbf{x}_n)\,\delta\mathbf{x}_n, \tag{8.11}$$

where for a two-dimensional area-preserving twist map with coordinates (x_n, y_n),

$$\delta\mathbf{x}_n = \begin{pmatrix} \delta x_n \\ \delta y_n \end{pmatrix} \tag{8.12}$$

is the first variation of $\mathbf{x}_n = \left(\begin{smallmatrix} x_n \\ y_n \end{smallmatrix}\right)$ and

$$M(\mathbf{x}_n) = \begin{pmatrix} \frac{\partial x_{n+1}}{\partial x_n} & \frac{\partial x_{n+1}}{\partial y_n} \\ \frac{\partial y_{n+1}}{\partial x_n} & \frac{\partial y_{n+1}}{\partial y_n} \end{pmatrix} \tag{8.13}$$

is the Jacobian matrix. Iterating Equation (8.11) n times, beginning with $\mathbf{x}_0$, it can be seen that [7]

$$\delta\mathbf{x}_n = M(\mathbf{x}_{n-1})M(\mathbf{x}_{n-2})\cdots M(\mathbf{x}_0)\,\delta\mathbf{x}_0. \tag{8.14}$$

However, because x_i and x_{i+1} both lie on the same orbit, $M(\mathbf{x}_i) = M(\mathbf{x}_{i+1})$, so we simplify Equation (8.14) to [7]

$$\delta\mathbf{x}_n = M^n\,\delta\mathbf{x}_0, \tag{8.15}$$

where $M = M(\mathbf{x}_i)$ for all $i \in \mathbb{Z}$. We then define **Greene's residue** [42]

$$R = \frac{1}{4}\left[2 - \operatorname{tr}(M^n)\right], \tag{8.16}$$

which assigns a numerical value to the stability of the orbits within a neighbourhood of a periodic orbit. Although a residue of zero does not always imply integrability, the residue is defined such that it is always equal to zero within integrable systems. The relationship between the residue and the stability of the orbits within a neighbourhood of a periodic orbit is defined by Table 8.2 [7, 43].

Residue	**Stability**	**Structural Stability**
$R < 0$	Hyperbolic	Unstable
$R = 0$	Parabolic	Unstable
$0 < R < 1$	Elliptic	Stable
$R = 1$	Parabolic	Unstable
$R > 1$	Reflection hyperbolic	Unstable

Table 8.2: Relationship between the linear stability and residue of the orbits within a neighbourhood of a periodic orbit for two-dimensional area-preserving twist maps.

In the case of the standard map, the Jacobian matrix is given by

$$M = \begin{pmatrix} 1 - k\cos 2\pi x_n & 1 \\ -k\cos 2\pi x_n & 1 \end{pmatrix}, \tag{8.17}$$

so that after one iteration, the residue is given by

$$R = \frac{k}{4}\cos 2\pi x_n. \tag{8.18}$$

Assuming that $k \geq 0$, this residue implies that the standard map has no periodic orbits with reflection hyperbolic stability for $k \leq 4$, although periodic orbits with elliptic and parabolic stability exist for all $k > 0$.

8.6 Existence of KAM Tori

By definition, the reconciled QFMin-ghost curves C^+ and C^- are equivalent to each other in the limit as $k \to 0$, because they must lie on an invariant torus. However, for $k > 0$, these invariant tori do not exist for all ϵ, and they cannot exist whenever ϵ is rational. Those invariant tori that do exist for $k > 0$ are called **KAM tori**, and their existence can be determined by calculating the residue. According to **Greene's residue criterion** [42,44], the existence of a KAM torus can be determined by studying the linear stability of the periodic orbits with ϵ equal to the continued-fraction convergents of the KAM torus's rotational transform. As the order of the approximation to irrational ϵ increases, the action-minimax and action-minimising orbits cover increasingly greater regions of phase space, and in the limit as

$$\lim_{i\to\infty} \frac{p_i}{q_i} \to \omega, \tag{8.19}$$

the action-minimax and action-minimising orbits form a complete KAM torus. The only stipulations are that ω is irrational, p_i/q_i is a set of continued-fraction convergents of ω, and the residue of the periodic orbits with $\epsilon = p_i/q_i$ is between zero and one inclusive. In the standard map, a residue of zero corresponds to $k = 0$, whereas a residue of ≈ 0.25 corresponds to $k = 0.971635\ldots$ [45]. Because the residue diverges for $k > 0.971635\ldots$, the last remaining KAM torus must be destroyed at this point [45].

Another way to determine the existence of a KAM torus is by minimising the action gradient in any norm over a series of tori that have rotational transform equal to the continued-fraction convergents of the KAM torus, and observing whether the action gradient converges to zero as the order of the approximation to irrational ϵ increases. This behaviour can be seen in Figures 8.19–8.26, where the C^+ and C^- curves become more and more similar to each other not only as $k \to 0$, but also as $\epsilon \to \phi$, which implies the existence of a KAM torus for some $k > 0$. The reason for this implication is that the difference between the reconciled QFMin-ghost curves C^+ and C^- is the discrete-time action gradient ΔI or ΔJ, and the minimum of the action gradient under any norm provides a measure of the "distance" of an almost-invariant torus from being an invariant torus (compare Sections 3.3, 3.4, 5.7 and 6.6). Hence, $\delta S/\delta\theta \to 0$, $\Delta I \to 0$ and $\Delta J \to 0$ as $k \to 0$ and $\epsilon \to \phi$, so the reconciled QFMin-ghost curves C^+ and C^- should be equivalent to each other in the limits as $k \to 0$ and $\epsilon \to \phi$. Whether this is actually the case for the reconciliation described throughout the bulk of this thesis will be the subject of Section 8.7.

8.7 Difference Plots of the Reconciled QFMin-Ghost Curves

According to Greene's residue criterion, the standard map contains invariant tori with $\epsilon = \phi$ for all $k < 0.971635\ldots$. Because the reconciliation between QFMin and ghost tori was only performed for Hamiltonian systems that obey the standard map, and because the modified quadratic flux functional under which the QFMin-ghost tori were minimised (Equation (4.42)) provides a suitable action gradient norm, the accuracy of the reconciliation can be double-checked by ensuring that it agrees with Greene's residue criterion. In order to demonstrate that the reconciled QFMin-ghost tori do indeed approach an invariant torus in the limit as $\epsilon_i = p_i/q_i \to \phi$, where p_i/q_i are the continued-fraction convergents of ϕ and $k < 0.971635\ldots$, the differences $\Delta J = \delta S/\delta\Theta = \theta'(\Theta)(J^+ - J^-)$ between the reconciled QFMin-ghost curves C^+ and C^- were plotted in (Θ, J)-space. These plots are shown in Figures 8.27-8.33.

When the rotational transform is rational, there are exactly q peaks and q troughs in the ΔJ curves. This is because the action-minimax and action-minimising orbits both intersect the Poincaré section q times before they return to their starting points. The QFMin equation $\Delta J = \nu(\Theta_0)$ implies that the amplitude of the ΔJ curves is constant with respect to Θ. Based on Figures 8.27-8.33, the difference plots look approximately sinusoidal, with the amplitude depending only on k and ϵ. It can also be seen from Figures 8.27-8.33 that the amount of flux, quantified by ΔJ, decreases for each particular k value as $\epsilon \to \phi$, which shows that the reconciled QFMin-ghost curves and tori are consistent with Greene's residue criterion and the existence of KAM tori within the standard map for $\epsilon = \phi$ when $k < 0.971635\ldots$. When $k = 1.0$ and $\epsilon = 1/3$, the maximum difference between the C^+ and C^- curves is about 6×10^{-3}, but when $k = 1.0$ and $\epsilon = 5/13$, the maximum difference between the C^+ and C^- curves is about 9×10^{-5}, which is a difference of almost two orders of magnitude.

Due to limited relative numerical resolution, we have not shown the difference curves for all k and ϵ presented in Sections 8.2–8.4. For $\epsilon = 3/8$, we have not shown the $k = 0.2$ curve, and for $\epsilon = 5/13$, we have not shown the $k = 0.2$, $k = 0.4$ and $k = 0.6$ curves, because as $k \to 0$ and $\epsilon \to \phi$, $\Delta J \to 0$ and the Fourier coefficients dip below the threshold for which they can be calculated with sufficient accuracy to determine accurate ΔJ curves. For $\epsilon = 1/3$ and $\epsilon = 2/5$, the Fourier coefficients are sufficiently large that the zeroes of ΔJ for nonzero k are separated by integer multiples of $\Theta/2\pi = 1/2q$, which is required by the fact that the action-minimax and action-minimising orbits are separated by distances of $\Theta/2\pi = 1/2q$ and have $\Delta J = 0$ (see Section 8.4). However, when k is low and $\epsilon = 3/8$ or $\epsilon = 5/13$, the interval spacing of zeroes of ΔJ is not consistent with the location of the action-minimax and action-minimising orbits predicted by our transformation. We attribute this to the smaller Fourier coefficients in these cases, which we have been forced to omit due to their low resolution. For all ϵ cases considered, we have also omitted the difference curves for high k. This is because the truncation mode number is too low, and because the transformation $\theta(\Theta)$ approaches the loss of monotonicity as k increases.

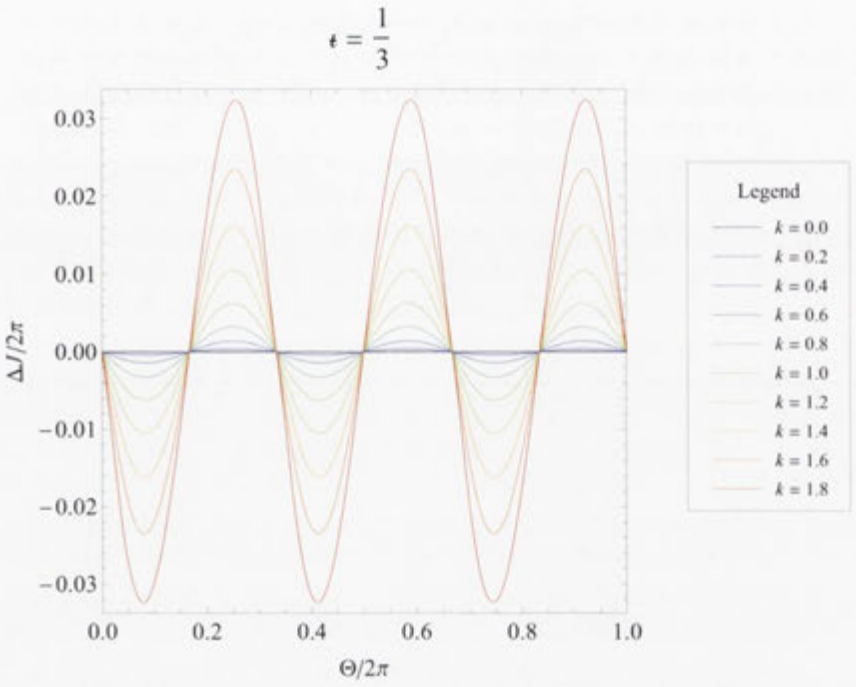

Figure 8.27: Plot of the difference between the reconciled QFMin-ghost curves C^+ and C^- in (Θ, J)-space for $\epsilon = 1/3$ when $j = 27$ and the accuracy goal is 9.

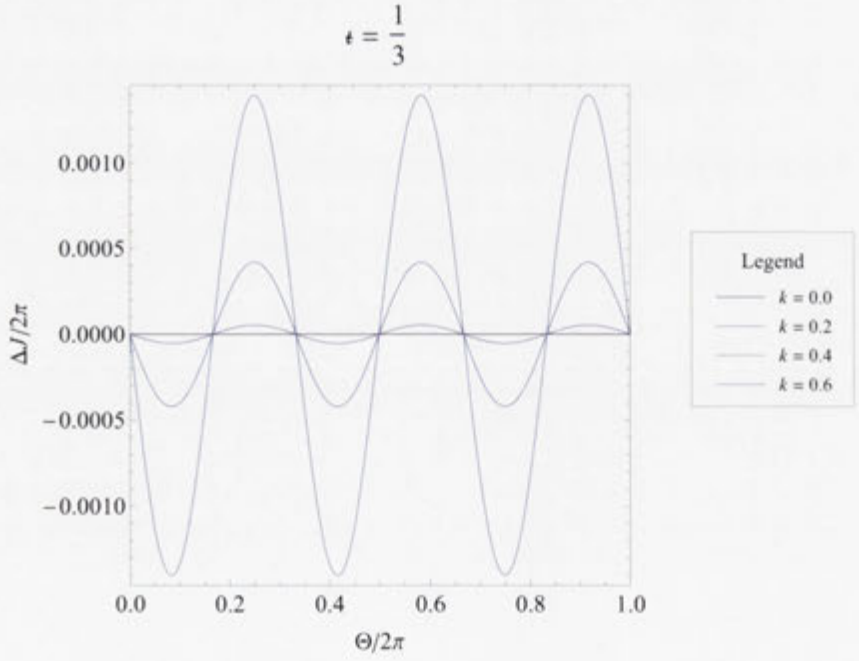

Figure 8.28: Magnified plot of the difference between the reconciled QFMin-ghost curves C^+ and C^- in (Θ, J)-space for $\epsilon = 1/3$ when $j = 27$ and the accuracy goal is 9.

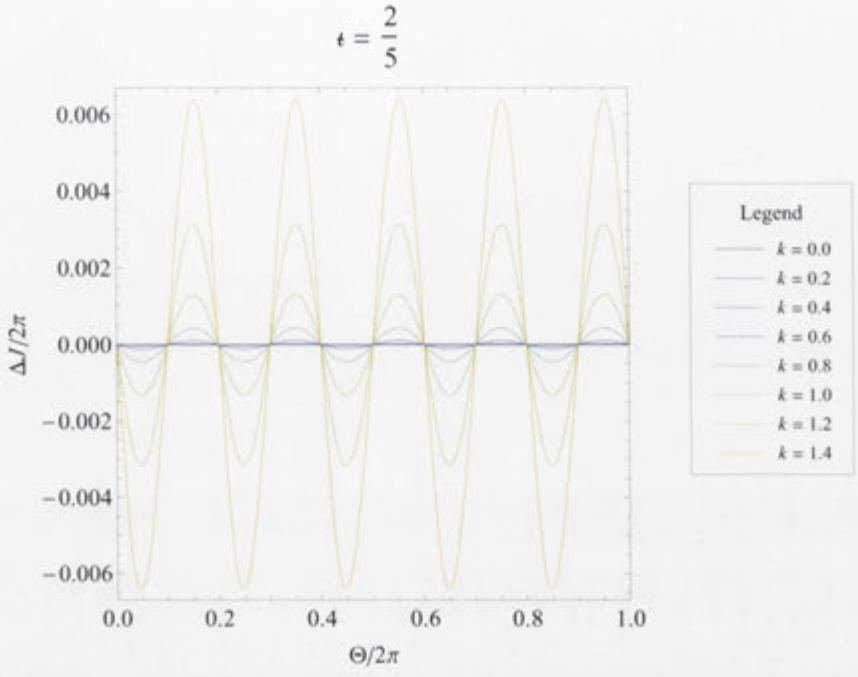

Figure 8.29: Plot of the difference between the reconciled QFMin-ghost curves C^+ and C^- in (Θ, J)-space for $\epsilon = 2/5$ when $j = 50$ and the accuracy goal is 8.

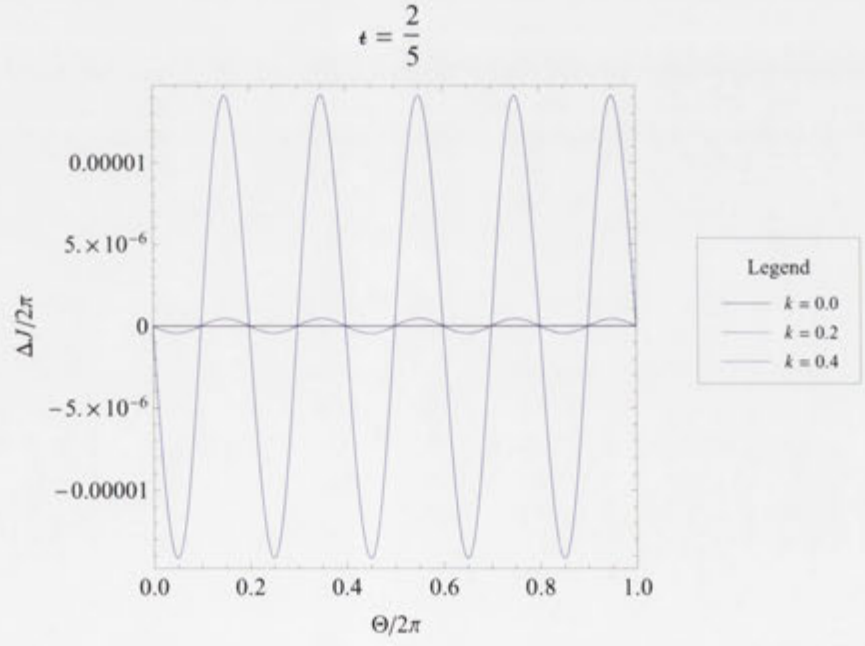

Figure 8.30: Magnified plot of the difference between the reconciled QFMin-ghost curves C^+ and C^- in (Θ, J)-space for $\epsilon = 2/5$ when $j = 50$ and the accuracy goal is 8.

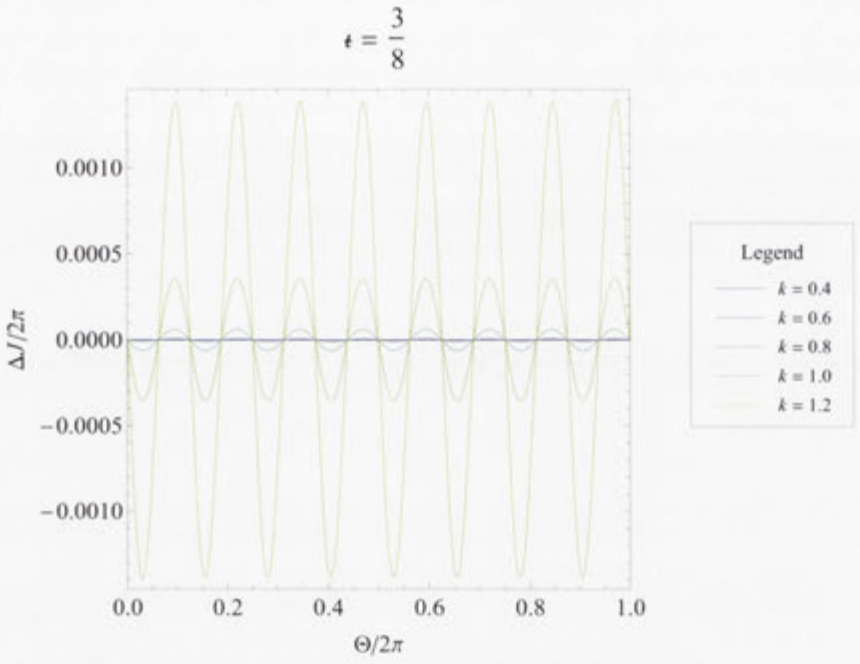

Figure 8.31: Plot of the difference between the reconciled QFMin-ghost curves C^+ and C^- in (Θ, J)-space for $t = 3/8$ when $j = 48$ and the accuracy goal is 8.

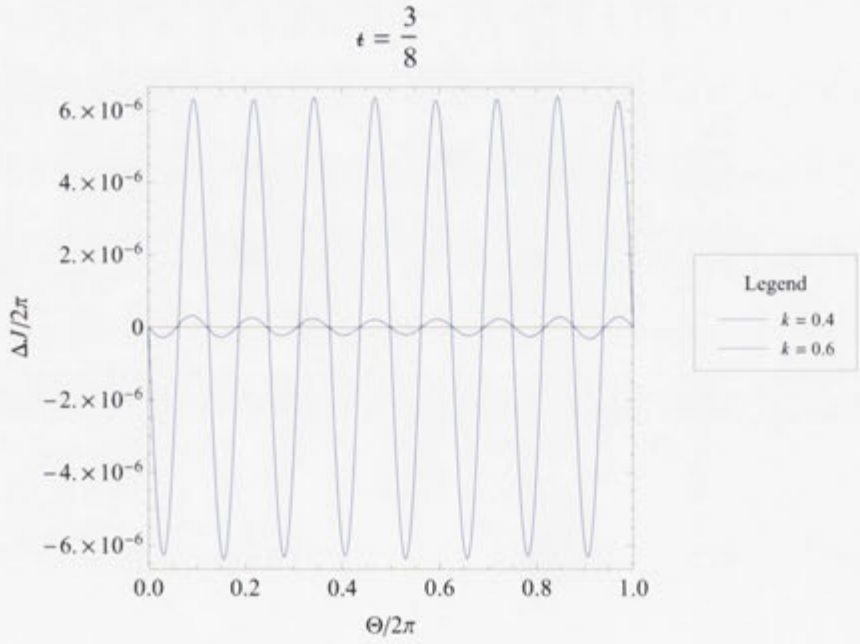

Figure 8.32: Magnified plot of the difference between the reconciled QFMin-ghost curves C^+ and C^- in (Θ, J)-space for $t = 3/8$ when $j = 48$ and the accuracy goal is 8.

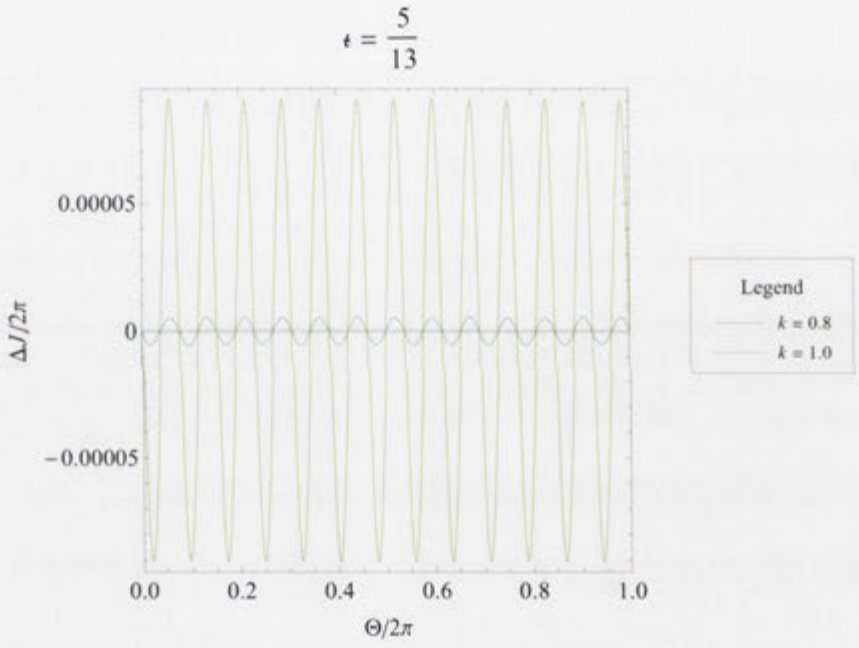

Figure 8.33: Plot of the difference between the reconciled QFMin-ghost curves C^+ and C^- in (Θ, J)-space for $\epsilon = 5/13$ when $j = 52$ and the accuracy goal is 8.

8.8 Determination of the Flux-Leakage Exponents

Once the differences between the reconciled QFMin-ghost curves C^+ and C^- had been plotted in phase space, the amplitudes of the difference curves were plotted as a function of $1/q$ (where q is the denominator of the rational rotational transform) for various k values and interpolated with a linear function, which can be seen in Figure 8.34. We expect that for $k < 0.971635\ldots$, the curves of the amplitude of ΔJ versus $1/q$ will pass through the origin (if the scale is linear), and that for $k > 0.971635\ldots$, they will intercept the positive vertical axis, thus demonstrating the existence of an invariant torus for $k < 0.971635\ldots$ and an invariant cantorus for $k > 0.971635\ldots$ whenever $\epsilon = n \pm \varphi$ and $n \in \mathbb{Z}$, in accordance with the KAM theorem and the Aubry-Mather theorem. This would allow us to use the action gradient and the quadratic flux as an alternative to Greene's residue when determining the existence of KAM tori. Figure 8.34 suggests these properties, but is inconclusive because the order of the approximation to $\epsilon = \phi$ is very low.

Because the continued-fraction convergents of $\epsilon = \phi$ were not sufficiently close to ϕ in order for us to accomplish this, we decided to model the amplitude by assuming it has the form

$$\operatorname{amp}\left(\frac{\Delta J}{2\pi}\right)_k = c_k \left(\frac{1}{q}\right)^{\alpha_k}, \tag{8.20}$$

where $\operatorname{amp}(\Delta J/2\pi)_k$ is the mean of the absolute values of the local extrema of $\Delta J/2\pi$, and find the **flux-leakage exponents** α_k. We expect this model to be valid for $k < 0.971635\ldots$ with $\alpha_k > 0$. In this case, the amplitudes of the ΔJ curves approach zero as $1/q$ approaches zero. For $k > 0.971635\ldots$, the amplitudes of the ΔJ curves will not approach zero as $1/q$ approaches zero, so $\alpha_k = 0$. In order to find the flux-leakage exponents, we take the logarithm of both sides of Equation (8.20), which gives

$$\ln\left[\operatorname{amp}\left(\frac{\Delta J}{2\pi}\right)_k\right] = \alpha_k \ln\left(\frac{1}{q}\right) + \ln c_k, \tag{8.21}$$

from which we can see that the flux-leakage exponents are merely the gradients

$$\alpha_{k,i} = \frac{\ln\left[\operatorname{amp}\left(\frac{\Delta J}{2\pi}\right)_{k,i+1}\right] - \ln\left[\operatorname{amp}\left(\frac{\Delta J}{2\pi}\right)_{k,i}\right]}{\ln\left(\frac{1}{q_{i+1}}\right) - \ln\left(\frac{1}{q_i}\right)} \tag{8.22}$$

of the plots of the amplitudes of $\Delta J/2\pi$ against $1/q$ for successive continued-fraction convergents of ϵ, with k held constant. Because we know the amplitudes of some of the ΔJ curves for four different values of ϵ, we potentially have up to three different approximations to each flux-leakage exponent, indexed by $i \in \{1, 2, 3\}$. These i denote the ith term in Sequence (8.10). They also label the gradients shown in Figure 8.34, in which case, $i = 1$ labels the gradient between $1/q = 1/5$ and $1/q = 1/3$, $i = 2$ labels the gradient between $1/q = 1/8$ and $1/q = 1/5$, and $i = 3$ labels the gradient between $1/q = 1/13$ and $1/q = 1/8$. The approximations to α_k were plotted as a function of k in Figure 8.35, and interpolated and extrapolated to the axes. The first two approximations were interpolated with a cubic function, whereas the third approximation was interpolated with a linear function due to a lack of data points. We expect that as more data points are added to Figures 8.34 and 8.35, the extrapolation range of the α curves for $\alpha > 0$

will contract. The extrapolations of Figure 8.35 are qualitatively consistent with the idea that, as the order of the approximation to α_k (as $\epsilon \to \phi$) increases, the k-intercept of the interpolation approaches the critical value $k_c = 0.971635\ldots$, which would confirm that the reconciled QFMin-ghost tori are consistent with Greene's residue criterion. However, many more cases would need to be included in the study before a quantitative statement could be made.

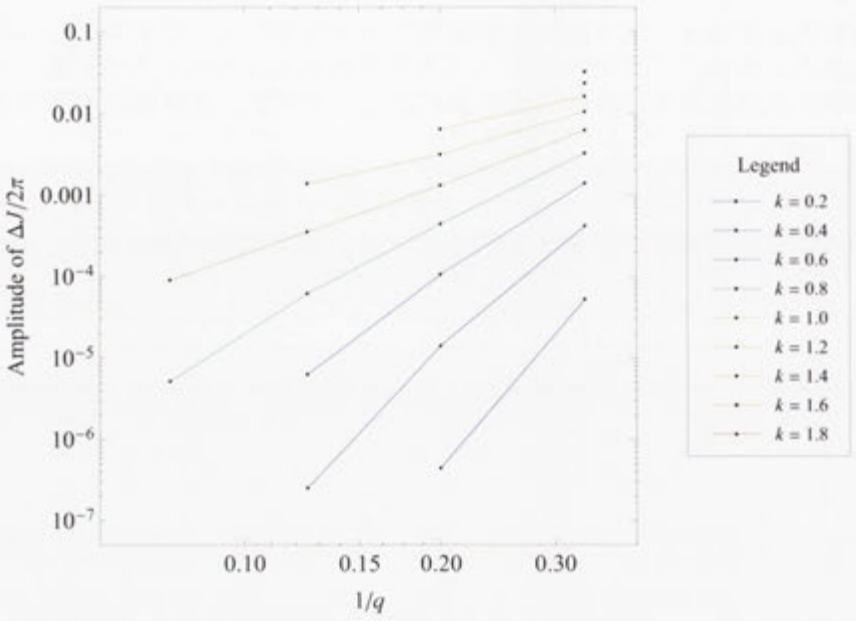

Figure 8.34: Plot of the amplitudes of $\Delta J/2\pi$ for different values of k and $1/q$, interpolated with a linear function.

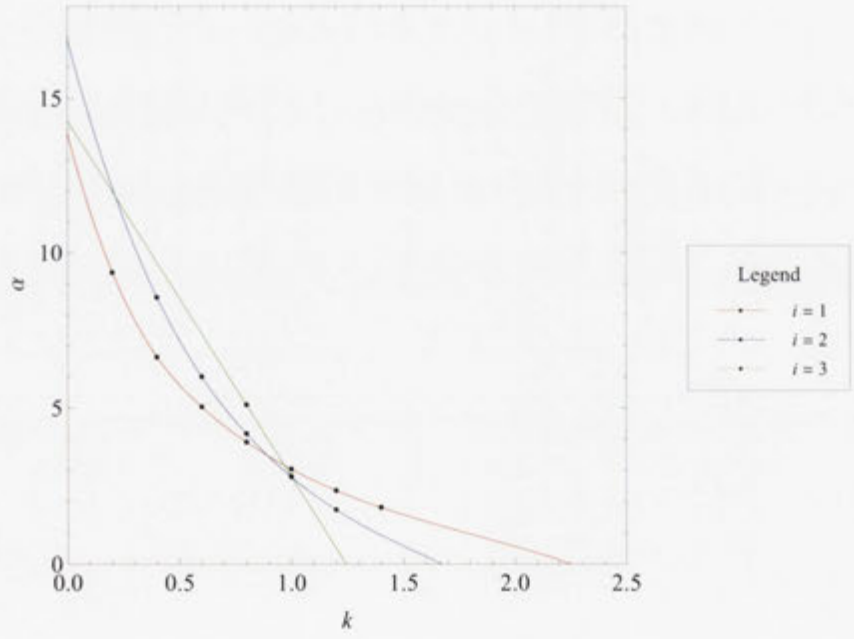

Figure 8.35: Plot of the flux-leakage exponents $\alpha_{k,i}$, corresponding to the gradients of the linear interpolations shown in Figure 8.34. These flux-leakage exponents have been interpolated with a cubic function and extrapolated to the axes, except for those corresponding to $i = 3$, which have been interpolated with a linear function due to a lack of data points.

8.9 Summary of the Results

We have considered three candidates for almost-invariant tori, called QFMin, AGMin and ghost tori, and demonstrated that they can be reconciled with each other in certain cases of the standard map when they are subjected to a suitable change of coordinates. This provides an important first step towards constructing an almost-straight-field-line coordinate system for magnetic islands. Specifically, we have shown that:

- QFMin and ghost tori are equivalent for all rational rotational transforms $\epsilon = p/q$, where p and q are mutually prime integers, up to at least $k = 1.0$ for $q \leq 13$, at least $k = 1.2$ for $q \leq 5$, and at least $k = 1.4$ for $q \leq 3$, where k denotes the nonlinearity parameter of the standard map. This is based on the fact that the Fourier series defined by Equation (7.36) and subject to the minimisation of Equation (7.28) converges to an accuracy of at least 10^{-6} for all $k \leq 1.4$ when $\epsilon = 1/3$, for all $k \leq 1.2$ when $\epsilon = 2/5$, and for all $k \leq 1.0$ when $\epsilon = 3/8$ and $\epsilon = 5/13$, and the fact that these rotational transforms are the continued-fraction convergents of a golden number, so they converge more slowly than all other rational rotational transforms with a lower absolute value of q.

- The reconciliation appears to break down at around $k = 2.1$ when $\epsilon = 1/3$, at around $k = 1.5$ when $\epsilon = 2/5$, at around $k = 1.3$ when $\epsilon = 3/8$, and just under $k = 1.2$ when $\epsilon = 5/13$. However, it's difficult to determine whether the reconciliation has actually broken down or not, because the apparent breakdown in the monotonicity of the transformation could also be caused by the Gibbs phenomenon, the way *Mathematica* handles line searches when the derivative of the transformation is very small, and the particular conjugacy constraint we have used.

- The reconciled QFMin-ghost tori are consistent with Greene's residue criterion and the existence of KAM tori within the standard map with $\epsilon = \phi$, where ϕ denotes two minus the golden mean, for $k < 0.971635\ldots$. This is based on plots of the differences between the reconciled QFMin-ghost curves C^+ and C^-, plots of the amplitudes of those differences, and the determination of a set of flux-leakage exponents from those plots.

- Because QFMin and ghost tori can be reconciled with each other, then the reconciled QFMin-ghost tori must also be reconciled with AGMin tori by means of the rigidity principle defined in Section 4.1. This rigidity principle states that if any two of QFMin, AGMin and ghost pseudo-orbits are reconciled with each other, then they must also be reconciled with the third. Although the rigidity principle was only proven for continuous-time systems, it can also be applied to discrete-time systems via the kicked rotor.

8.10 Implications of the Results

The results of this thesis have numerous implications for toroidal magnetic confinement devices, although none of the results can be applied directly to them. This is because many of the results are highly mathematical, and have yet to be studied in relation to real magnetic confinement systems. However, the results do look promising for toy models such as the kicked rotor and the standard map, and are likely to be extended to real magnetic confinement systems in the future. The most important implications of this research are:

- That under the conditions specified for QFMin and ghost tori to be equivalent in Sections 8.2 and 8.9:
  - Ghost curves can be calculated using the same methods as for QFMin and AGMin curves by transforming them to (Θ, I)-space, thus reducing the amount of time it takes to calculate them.
  - Temperature isotherms can be reconciled with one of QFMin, AGMin and ghost curves if and only if they can be reconciled with all three of them. Thus, if ghost curves are more than just a mathematical construct, but a physical entity, as Hudson and Breslau [29] suggest, then QFMin and AGMin curves must also have the same physical interpretation.
- That we are one step closer to constructing an almost-straight-field-line coordinate system for magnetic islands, which will allow us to find a precise mathematical way to minimise the amount of chaos inside stellarators and to design them such that the number of magnetic surfaces inside them is maximised. Such surfaces would be very similar to the almost-invariant tori discussed in this thesis.

8.11 Further Research

We have already discussed numerous ways in which the results of this thesis could be improved and extended by further research. Some suggestions include:

- Minimising the effect of ringing due to high j truncation by applying a non-boxcar windowing function to ΔJ_n in Equation (7.35).
- Minimising the effect of undershooting in the Fourier representation by applying a high-k roll-off filter to the Fourier coefficients, thereby creating a smoother truncation for them.
- Minimising the effect of overshooting in the numerical minimisation of the variational principle by constraining $\theta'(\Theta)$ to be strictly positive in Equation (7.2), thereby eliminating the risk of obtaining a negative value for $\theta'(\Theta)$.
- Finding a better conjugacy constraint to replace the one used in Section 7.4, that could allow us to demonstrate numerically that QFMin and ghost tori can be reconciled with each other for much larger k values than they are now, and for rotational transforms that are a greater-order approximation to $\iota = \phi$. A prime candidate for this is the removal of the constraint that the resonant terms be zero and the

replacement of the objective function (Equation (7.12)) with

$$\begin{aligned}\mathcal{V}[\theta_{-j},\ldots,\theta_j] &= \frac{1}{2}\left\langle\left[\tilde{\mathbb{P}}(\Delta J_n)\right]^2\right\rangle + \left\langle\left[\bar{\mathbb{P}}(\Delta J_n)\right]^2\right\rangle\langle\sin^2\Theta_0\rangle - \langle\bar{\mathbb{P}}(\Delta J_n)\sin\Theta_0\rangle^2 \\ &= \frac{1}{2}\left\langle(\Delta J_n)^2\right\rangle - \langle\Delta J_n\sin\Theta_0\rangle^2,\end{aligned} \tag{8.23}$$

where

$$\langle f_n\rangle \equiv \frac{1}{4\pi^2}\int_0^{2\pi/q}\sum_{n=0}^{q-1} f_n\,\mathrm{d}\Theta_0, \tag{8.24}$$

which is suggested by the results of Dewar and Khorev [25]. This will hopefully lead to a proof that the action gradient and the quadratic flux can be used as an alternative to Greene's residue when determining the existence of KAM tori.

- Replacing the Fourier representation of $\theta(\Theta)$ with finite elements, thereby localising errors in phase space and potentially improving the convergence, even in cases where k is very low and the order of the approximation to $\iota = \phi$ is large. This is because the function $\theta'(\Theta)$ is jagged, so it requires many terms in our Fourier series treatment, and because each Fourier term is global, so the Fourier approximation is sensitive to the accuracy of large Fourier coefficients in regions where $\theta'(\Theta)$ is small.

- Reducing the probability of the transformation becoming singular by replacing the current discrete-time coordinate transformation with a new canonical transformation of the form $\theta = \theta(\Theta, J)$, for which J is 2π-periodic.

- Showing that QFMin and ghost tori can be reconciled in real magnetic confinement systems by using a real magnetic confinement map instead of the standard map, thereby facilitating the construction of an almost-straight-field-line coordinate system for magnetic islands.

Bibliography

[1] A. H. Boozer, Rev. Mod. Phys. **76**, 1071 (2004).

[2] *Plasma Physics: An Introductory Course*, edited by R. Dendy (Cambridge University Press, Cambridge, 1993).

[3] M. Madau, Lightning over Oradea Romania zoom, photograph, 2005.

[4] A. H. Boozer, Phys. Plasmas **5**, 1647 (1998).

[5] J. Wesson, *Tokamaks*, 3 ed. (Oxford University Press Press, Oxford, 2004).

[6] S. R. Hudson, Phys. Plasmas **11**, 677 (2004).

[7] J. D. Meiss, Rev. Mod. Phys. **64**, 795 (1992).

[8] M. G. Davidson, R. L. Dewar, H. J. Gardner, and J. Howard, Aust. J. Phys. **48**, 871 (1995).

[9] A. J. Lichtenberg and M. A. Lieberman, *Regular and Chaotic Dynamics*, 2 ed. (Springer-Verlag, New York, 1992).

[10] D. K. Arrowsmith and C. M. Place, *An Introduction to Dynamical Systems* (Cambridge University Press, Cambridge, 1991).

[11] J. N. Mather, Topology **21**, 457 (1982).

[12] C. Golé, *Symplectic Twist Maps: Global Variational Techniques* (World Scientific, Singapore, 2001).

[13] J. D. Meiss and R. L. Dewar, in *Proceedings of the Centre for Mathematical Analysis, Australian National University, Miniconference on Chaos & Order, Canberra, Australia, 1-3 February 1990*, edited by N. Joshi and R. L. Dewar (World Scientific, Singapore, 1991), pp. 97–103.

[14] S. R. Hudson and R. L. Dewar, Phys. Lett. A **226**, 85 (1997).

[15] A. H. Boozer, Phys. Fluids **26**, 1288 (1983).

[16] S. R. Hudson and R. L. Dewar, Phys. Lett. A **373**, 4409 (2009).

[17] R. L. Dewar, S. R. Hudson, and A. M. Gibson, J. Plasma Fusion Res. Ser. **9**, 487 (2010).

[18] H. Goldstein, *Classical Mechanics*, 2 ed. (Addison-Wesley Publishing Company, Inc., United States of America, 1980).

[19] R. L. Dewar, S. R. Hudson, and A. M. Gibson, Commun. Nonlinear Sci. Numer. Simulat. **17**, 2062 (2012).

[20] P. Glendinning, *Stability, Instability and Chaos: an introduction to the theory of nonlinear differential equations* (Cambridge University Press Press, Cambridge, 1994).

[21] R. L. Dewar, lecture notes for the PHYS3001 Classical Mechanics course taught at the Australian National University in Canberra, Australia (unpublished).

[22] G. Casati, B. V. Chirikov, F. M. Izraelev, and J. Ford, in *Stochastic Behavior in Classical and Quantum Hamiltonian Systems*, Vol. 93 of *Lecture Notes in Physics*, edited by G. Casati and J. Ford (Springer, Berlin, 1979), pp. 334–352.

[23] P. J. Morrison, Rev. Mod. Phys. **70**, 467 (1998).

[24] B. Chirikov and D. Shepelyansky, Scholarpedia **3**, 3550 (2008).

[25] R. L. Dewar and A. B. Khorev, Physica D **85**, 66 (1995).

[26] S. R. Hudson and R. L. Dewar, J. Plasma Phys. **56**, 361 (1996).

[27] R. L. Dewar, S. R. Hudson, and P. F. Price, Phys. Lett. A **194**, 49 (1994).

[28] R. L. Dewar and S. R. Hudson, in *Proceedings of the International Conference on Plasma Physics (ICPP), Nagoya, Japan, 9–13 September 1996*, Japan Soc. Plasma Sci. and Nucl. Fusion Res., edited by H. Sugai and T. Hayashi (Japan Soc. Plasma Sci. and Nucl. Fusion Res., Nagoya, Japan, 1996), Vol. 2, pp. 1262–1265.

[29] S. R. Hudson and J. Breslau, Phys. Rev. Lett. **100**, 095001 (2008).

[30] R. L. Dewar, research notes made on 25 August 2009 (unpublished).

[31] R. S. MacKay and M. R. Muldoon, Phys. Lett. A **178**, 245 (1993).

[32] R. S. MacKay and J. D. Meiss, Phys. Lett. A **98**, 92 (1983).

[33] R. L. Dewar and J. D. Meiss, Physica D **57**, 476 (1992).

[34] A. Khorev, Ph.D. thesis, The Australian National University, Canberra, Australia, 2002.

[35] Wolfram Research, Inc., *Mathematica*, 7 ed. (Wolfram Research, Inc., Champaign, Illinois, 2008).

[36] Wolfram Research, Inc., *Mathematica*, 8 ed. (Wolfram Research, Inc., Champaign, Illinois, 2010).

[37] E. L. Allgower and K. Georg, *Introduction to Numerical Continuation Methods* (Society for Industrial and Applied Mathematics, Philadelphia, 1979/2003).

[38] R. B. White, *The theory of toroidally confined plasmas*, 2 ed. (Imperial College Press, London, 2006).

[39] R. S. MacKay, J. D. Meiss, and I. C. Percival, Physica D **13**, 55 (1984).

[40] J. Foster and F. B. Richards, Amer. Math. Monthly **98**, 47 (1991).

[41] R. Haberman, *Applied Partial Differential Equations with Fourier Series and Boundary Value Problems*, 4 ed. (Pearson Education, Inc., New Jersey, 2004).

[42] J. M. Greene, J. Math. Phys. **20**, 1183 (1979).

[43] S. Huang, C. Chandre, and T. Uzer, J. Phys. B: At. Mol. Opt. Phys. **41**, 1 (2008).

[44] R. S. MacKay, Nonlinearity **5**, 161 (1992).

[45] P. J. Morrison, Phys. Plasmas **7**, 2279 (2000).